#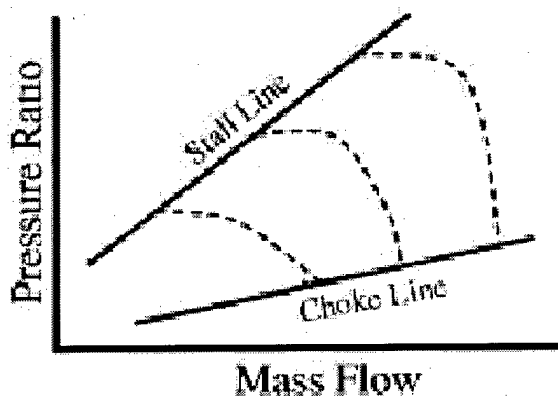 TECHNIQUE TO PREDICT STAGE-BY-STAGE, PRE-STALL COMPRESSOR PERFORMANCE CHARACTERISTICS USING A STREAMLINE CURVATURE CODE WITH LOSS AND DEVIATION CORRELATIONS

JASON KLEPPER

19991130 102

To the Graduate Council:

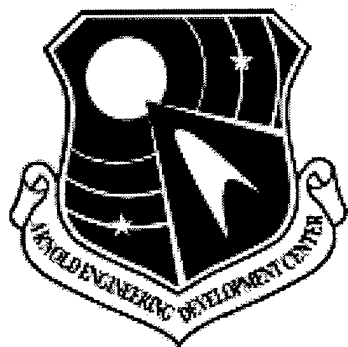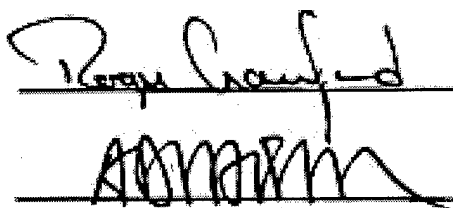I am submitting herewith a thesis written by Jason Brent Klepper entitled "Technique to Predict Stage-by-Stage, Pre-Stall Compressor Performance Characteristics Using a Streamline Curvature Code with Loss and Deviation Correlations." I have examined the final copy of the thesis for form and content and recommend that it be accepted in partial fulfillment of the requirements for the degree of Master of Science, with a major in Mechanical Engineering.

Roy J. Schulz, Major Professor

We have read this thesis
and recommend its acceptance:

Accepted for the Council:

_____

Associate Vice Chancellor and
Dean of the Graduate School

TECHNIQUE TO PREDICT STAGE-BY-STAGE, PRE-STALL COMPRESSOR PERFORMANCE CHARACTERISTICS USING A STREAMLINE CURVATURE CODE WITH LOSS AND DEVIATION CORRELATIONS

A Thesis
Presented for the
Master of Science
Degree
The University of Tennessee, Knoxville

Approved for public release, distribution unlimited.

Jason Brent Klepper
August 1998

DEDICATION

This thesis is dedicated to my Lord and Savior, Jesus Christ and my parents, Eugene and Joyce Klepper. Without their support, patience, encouragement and above all, unconditional love, I could not have completed this thesis.

ACKNOWLEDGEMENTS

I would like to express my sincere appreciation to the many individuals who helped make this work possible. Dr. Alan A. Hale has unselfishly given guidance, support, and assistance at anytime it was needed. Without him, this thesis could not have been completed. I would also like to thank Mrs. Jacqueline Chalk for her help and encouragement with this work, especially the time she spent reviewing this work. Dr. Milt W. Davis, Jr. is also due a special thanks for his support of the work and many suggestions to make it better. Appreciation is also extended to Mr. Peter Montgomery for his encouragement and guidance through the entire process. I would also like to thank Mr. Stephen Savelle for his assistance with my many network and computer problems. Mrs. Sherri Smith is appreciated for her assistance, especially in helping find several technical papers. I would also like to express appreciation to Mr. Matthew Prufert for his willingness to answer my many questions and for his encouragement. Dr. Douglas Garrard is also appreciated for his enthusiasm and assistance with the process of writing a thesis.

I would also like to express a deep appreciation to Dr. Roy J. Schulz for his willingness to serve as my thesis advisor and committee chairman. A special thanks is also extended to Dr. Roger Crawford and Dr. Ahmad Vakili for serving as committee members.

ABSTRACT

Because of the complex flow fields and component interaction in a modern gas turbine engine, these engines require extensive testing to validate performance and stability. The testing process can become expensive and complex. Modeling and simulation of gas turbine engines is one way to reduce testing costs, provide fidelity, and enhance the quality of essential testing. Several numerical simulations for gas turbine engines have been developed at Arnold Engineering Development Center to simulate gas turbine engines and their various components. Compressor performance characteristics are needed in these codes to provide turbomachinery source terms. These terms are currently provided by experimental data. A technique to analytically create these characteristics would greatly enhance the quality and value of the codes in existence.

Therefore, a technique to create 1-D and 2-D compressor performance characteristics with specifications of only annulus geometry, blade geometry, and loss and deviation correlations has been developed. This method uses a previously developed streamline curvature code (SLCC) with open literature loss and deviation correlations to provide on- and off-design stage performance. Data reduction techniques are then used to convert the predicted flow field behavior in the bladed regions into stage-by-stage performance characteristics of the compressor.

In the present investigation, it was discovered that the SLCC could provide an accurate flow field prediction with the calibration of relative total pressure loss coefficients and flow angle deviations to experimental data and the inclusion of inlet and exit radial blockages to correct static pressures and static temperatures. The results of the 1-D representations of compressor characteristics for a calibrated flow field were typically within one-percent of the experimental data. The 2-D representation gave a maximum error of about five-percent.

It was also discovered that machines with significantly different geometry will have different trends in calibration. A second machine was analyzed with unfavorable results when calibrated with the trends discovered from the first machine. This second machine was then analyzed without calibrations and produced a maximum error of less than seven-percent for the 1-D characteristics and less than 24-percent for a 2-D representation.

TABLE OF CONTENTS

LIST OF TABLES

TABLE

LIST OF FIGURES

FIGURE

LIST OF SYMBOLS

Symbol	Definition
a/c	point of maximum camber as a fraction of chord
A	area
c	chord
c_p	specific heat at constant pressure
D	diffusion factor
H_{loss}	hub loss constant
h	enthalpy
i	incidence
I	rothalpy
k	correction factor
l	computing station direction
m	slope factor, meridional direction, mass flow
M	Mach number
n	reference minimum-loss-incidence-angle slope factor, index
N	revolutions per second
NR_{cor}	percent design corrected speed
P	pressure
PR	pressure ratio
r	radius

Symbol	Definition
r_c	radius of curvature
R	gas constant for air
t/c	point of maximum thickness as a fraction of chord
T	temperature
T_{loss}	tip loss constant
TR	temperature ratio
u	axial velocity
U	wheel speed
V	absolute velocity
w	work
W	relative velocity, width
W_{cor}	corrected weight flow
z	axial direction

Greek

α	absolute fluid angle
β	relative fluid angle, blade metal angle
δ	deviation
ϕ	streamline slope, stage flow coefficient

Symbol	Definition
γ	specific heat ratio
λ	blockage
ρ	density
σ	solidity
θ	camber angle
$\bar{\omega}$	total pressure loss coefficient
Ψ	performance characteristic

Subscript	
0	zero-camber
1	inlet
2	exit
3D	three-dimensional
10	10-percent thick NACA 65-(A_{10})-series blade
a	axial component
c	critical
choke	choking condition
des	design
hub	hub location
i	incidence

Symbol	Definition
id	ideal
M	Mach number related
m	meridional component, metal angle
max	maximum
min	minimum
r	radial direction component
ref	reference condition
s	speed
shape	shape factor
stall	stalling condition
t	total
th	thickness factor
tip	tip location
va	axial velocity
vamn	mean axial velocity
vloss	viscous loss
z	axial direction component
θ	circumferential (tangential) direction component

Superscript	Definition
'	relative to the blade row
b	solidity exponent
P	pressure
T	temperature

STATEMENT OF PERMISSION TO USE

In presenting this thesis in partial fulfillment of the requirements for a Master's degree at The University of Tennessee, Knoxville, I agree that the Library shall make it available to borrowers under the rules of the Library. Brief quotations from this thesis are allowable without special permission, provided that accurate acknowledgment of the source is made. Permission for extensive quotation from or reproduction of this thesis may be granted by my major professor, or in his absence, by the Head of Interlibrary Services when, in the opinion of either, the proposed use of the material is for scholarly purposes. Any copying or use of the material in this thesis for financial gain shall not be allowed without my written permission.

Signature_____

Date_____

1.0 INTRODUCTION

Modern aircraft gas turbine engines are extremely complex machines, comprised of several major components. One of the major components of the turbine engine is the compressor. The compressor is designed to increase the pressure of the incoming air and deliver the correct amount of airflow to the rest of the engine. A common type of compressor for large gas turbine engines is the axial flow compressor. An axial flow compressor consists of one or more rotating blade rows which are aerodynamically coupled and rotate around a common axis of rotation. A typical gas turbine compression system is shown in Figure 1.1[1]. A compressor stage consists of a rotating blade row, the rotor, and a stationary blade row, the stator. Rotor blades are a circumferential array of airfoils that increase the kinetic energy of the flow. A pressure rise across the blades is achieved by flow diffusion in the rotor blade passage. Stator blades diffuse the flow more and redirect it to the next stage. The compressor is powered by a combustor and turbine at the back of the engine. The combustor adds energy to the flow and the turbine extracts energy from the flow as shaft work and transfers it to the compressor by a shaft.

Because of the adverse pressure gradient across the compressor, its performance and stability, on- and off-design, are critical. The performance of the compression system is normally shown on compressor performance maps. These

---

[1] All figures and tables may be found in the appendices.

1

maps can be shown in the form of pressure ratio and efficiency or pressure ratio and temperature ratio versus corrected mass flow. Corrected mass flow is mass flow which has been adjusted to reference total pressure and total temperature conditions. Correcting to reference conditions collapses the performance maps for different inlet total pressure and inlet total temperature conditions into one map. The performance data presented in Figure 1.2 is pressure ratio and temperature ratio versus corrected mass flow. The maps show the relationship between compressor total pressure ratio, compressor total temperature ratio, corrected mass flow, and corrected engine speed. The dashed line in the upper part of the total pressure ratio map is the surge line, or stall line. This line represents the limit of the pressure ratio as a function of corrected rotor speed and corrected mass flow rate. To the right of the line, the compressor operates in a stable manner. To the left of the stall line, the compressor may not operate, or will operate unstably. This is caused by high enough loading on the blades such that boundary-layer separation occurs over a large part of the blade. Operation beyond the stall region is structurally dangerous to the gas turbine engine (Mattingly, 1996).

Because of the complex flow fields and component interaction in gas turbine engines, these engines require extensive testing to validate performance and stability. This testing process is very expensive. Furthermore, it is economically and technically infeasible or impractical to measure every through-flow quantity at every location throughout the engine. Thus, complete component analysis cannot be performed during testing. Modeling and simulation of the gas

turbine engine is the way to analyze engine performance and ensure adequate test fidelity in the test program.

At Arnold Engineering Development Center (AEDC), modeling and simulation tools are looked at as necessary analytical methods to reduce testing cost and to enhance the quality of essential testing. To simulate the turbine engine and its components, several gas turbine modeling tools have been developed at AEDC. These codes are:

- **DYN**amic Turbine Engine Compressor Code – DYNTECC

- Aerodynamic Turbine Engine Code – ATEC

- Turbine Engine Analysis Compressor Code – TEACC.

DYNTECC (Hale and Davis, 1992) and ATEC (Garrard, 1995) are one-dimensional (1-D), stage-by-stage simulations. DYNTECC models only the compression system and combustor, while ATEC simulates the entire gas generator (compressor, combustor and turbine). The governing equations in both simulation models are the mass, momentum, and energy conservation equations applied to elemental control volumes with turbomachinery source terms (mass bleed, blade forces, heat transfer, and shaft work) included in the blade row elemental control volumes. The source terms simulate the effect the blades have on a control volume and are determined from a complete set of stage pressure and temperature characteristics.

TEACC (Hale and O'Brien, 1997) is a three-dimensional (3-D) compressor code. This code solves the compressible, 3-D Euler equations modified to include turbomachinery source terms. Again, compressor characteristics can be used to calculate these source terms.

Currently, the performance characteristics must be provided by experimental data for a given stage or compressor. To be able to model a machine without experimental data, a general method is needed to generate the performance maps for a given compressor. The work included in this thesis will provide the necessary steps of using compressor geometry parameters, a streamline curvature code (SLCC), and data reduction to develop both 1-D and radial distributions of performance characteristics to calculate the turbomachinery source terms required by each of the three codes mentioned above.

This thesis is organized to first give a brief review of other techniques used to develop compressor performance characteristics. The methodology and solution technique of the SLCC are then explained. This section includes an in-depth investigation of the transonic loss and deviation correlations used in the SLCC. Next, the calibration of the SLCC to a machine with experimental data is presented. With the results of the calibration for the first machine, the 1-D and two-dimensional (2-D) performance characteristics of another machine are predicted. Then, the results are summarized and conclusions are discussed. Finally, suggestions for future work are presented.

2.0 REVIEW OF THE LITERATURE

Because stage-by-stage analysis of a gas turbine compression system requires compressor stage performance characteristics, many attempts have been made to develop these characteristics. These methods range from a 1-D, 2-D, and 3-D analyses, to altering generic maps to match limited stage-by-stage data. Prior to explaining the current methodology, previous work on generation of performance characteristics is reviewed.

2.1 Experimental Data

Experimental methods are a very common way to develop compressor performance characteristics. Pressure and temperature measurements are obtained at the front and back of a compressor stage (Cyrus, 1996). This data can be taken from either compressor rig tests or actual complete engine tests. The pressure and temperature data is then reduced to stage-by-stage characteristics. These methods require the actual testing of hardware. Also, in the development phase, to test a new blade shape or stage setup, new blades have to be cut and tested. Davis and O'Brien (1991) took experimental data from a three-stage compressor rig and converted it to 1-D, steady-state characteristics. These steady-state characteristics were then used to model an unsteady, post-stall compression system. Similar studies were presented by Davis, Hale, Sharohroki, and Garrard (1996) for a 10-stage machine and a T-55 helicopter engine. Because these methods require the

building and testing of hardware, they can become expensive. Therefore accurate computational methods are desirable.

2.2 One-Dimensional Techniques

One-dimensional (1-D) techniques are simple and fast methods for obtaining compressor performance predictions. A drawback to the 1-D analysis is that the true 3-D physics of the flow in the compressor are replaced by a 1-D model which must inherently predict the average of what occurs across a blade row. A 1-D method to generate stage characteristics was presented by Attia and Schobeiri (1995). This method required that blade row exit flow angles be given and used a loss correlation model developed by one of the authors to predict loss across a blade row. The only other required inputs were geometry, rotational speed, and mass flow rate. The technique assumed that deviation angles were negligible. The deviation angle is the angular difference between the blade metal angle and the actual exit flow angle. The results were presented in the form of pressure ratio and efficiency versus mass flow. It was concluded that the model was satisfactory for blades of small height. This result were satisfactory only for blades of small height because of the assumption that the deviation angle was negligible everywhere, which cancelled hub and tip effects.

Johnson (1991) presented a method for calculating 1-D, stage-by-stage characteristics using a blade element technique. This technique requires the actual inlet and exit flow conditions and solves the continuity, energy, and momentum

equations at every stage. He used a deviation correlation presented by Horlock (1958). Horlock (1958) also provided a relationship between coefficient of drag and total pressure loss coefficient that was used in this correlation. The data used for both the loss and deviation correlations were developed from NACA data collected by Emery (1958). For the compressor studied by Johnson, this technique yielded predictions for performance characteristics that were higher than experimental data. This inaccuracy was blamed on the total pressure loss coefficient correlation.

The final 1-D method cited here was by Tsalavoutas et. al. (1994). This method was essentially a stage stacking technique. It required no knowledge of internal geometry but required some experimental performance data for the compressor. This method also involved no flow physics and relied entirely on experimental data. The method started with an initial set of generic stage characteristics and used optimization routines until selected points on the overall map were obtained within a desired accuracy level. The individual stage characteristics may not have been accurate, but the overall map was. The results of the characteristics were in the form of pressure ratio and efficiency versus corrected mass flow.

2.3 Two-Dimensional Techniques

Two-dimensional techniques, or throughflow techniques, are another common way to develop characteristics. Sayari and Böics (1995) developed a

technique based on the streamline curvature method. Most streamline curvature codes (SLCC) use a circumferential averaging technique to develop the 2-D flow field. Sayari and Böics offered a method that averaged normal to the central streamline. They argued that this method more accurately predicts the Mach number just before and around the shock. This model was considered an improvement on the commonly used Miller shock model discussed in detail in Section 3.2.1. This method concentrated on loss and deviation due to shocks and gave no consideration to other loss and deviation possibilities. The machines predicted were only simulated in the region where shocks were present. They presented graphical comparisons to data but never mentioned percent differences.

Korakianitis and Zou (1993) presented a streamline curvature method that, instead of iteratively solving the radial momentum equation, used a predictor-corrector technique to solve it in one pass. This reduced computational time. No correlations for deviation were presented; they must be provided by the user as known inputs. Loss across a blade row could have either been a user input or calculated by using open-literature loss correlations.

The final 2-D method (Yazigi, N. et. al., 1990) reviewed used a streamline curvature method for performance prediction. This method incorporated an inverse boundary-layer model to calculate the boundary-layer thickness at the trailing edge. Scholz's model, as described by Klein (1977), was used for estimation of the mixing losses. Deviation was determined by potential flow theory, taking into account the influence of the boundary layers, separation, and

8

stream tube height. The performance was presented in the form of pressure distribution. The computational time required for this method was still quite high, at nearly 0.75-hours on an IBM-PC for one run.

2.4 Three-Dimensional Techniques

Another computational method of developing performance characteristics is the use of 3-D computational fluid dynamics (CFD) codes. A method presented by Hah and Wennerstrom (1990) used a Reynolds-averaged Navier-Stokes equation solution to develop the flow field in blade rows. The results of the 3-D flow field for a transonic compressor with swept blades were presented as total pressure and total temperature characteristics. The resulting characteristics were within 2-percent of experimental data. This code required one hour of computational time on a Cray XMP supercomputer to converge to a solution for one flow point.

Another three dimensional technique was presented by Swan (1961). This technique used non-isentropic complete radial equilibrium-momentum equations combined with continuity, energy, and flow-process relations to derive a group of equations that could be solved on a computer. The results of a single stage machine were presented in the form of total pressure ratio and adiabatic efficiency versus corrected mass flow. The results given were accurate to within 10-percent of experimental data. This method used only a single variable to statistically

9

deduce the real fluid effects such as viscous losses and shock losses. The method was computer time intensive.

2.5 Present Investigation

As a consequence of the brief review of these previous compressor modeling approaches, it was concluded that the previous works lacked important desirable features need for this study. Specifically, all models exhibited one or more of the following deficiencies:

- Experimental data for the particular machine under study is required

- Only one or two sources of loss and deviation are utilized in the model

- Model does not account for spanwise variation in the flow

- Computational times are too long

The purpose of this thesis is to develop a compressor performance prediction technique that overcomes the deficiencies of the previous models and can give sufficiently accurate compressor performance predictions for compressors operating in pre-stall conditions. The technique will be based on input of geometric data for the annulus and blade shape; no experimental data for the particular machine under study is needed, except for calibration and validation. It is based on an existing streamline curvature code with several general loss and deviation correlation models. The model gives a radial distribution of the entire flow field and requires only seconds to run a flow point on a desktop computer.

3.0 APPROACH

The approach used in the present investigation is based on the use of a streamline curvature code (SLCC). The SLCC is essentially a duct flow solver with an imbedded set of loss and deviation correlations which provide the means to step across a bladed region. Because the SLCC is an integral part of this approach to calculating compressor stage characteristics, and the correlations are the heart of the SLCC, each needs to be investigated. A data reduction technique was developed that converts a radial distribution of performance quantities to their equivalent 1-D representations, and generates performance characteristics from the SLCC output. Details of the data reduction technique are also presented in this thesis.

3.1 Streamline Curvature Code Methodology

In the early 1950's, Wu (1952) developed the governing equations and general theory for a three-dimensional analysis of turbomachines. With improvements in computer sizes and speeds in the mid-1960's, numerical solution methods based on Wu's general theory were developed to solve flows through turbomachines. Marsh (1966) developed the matrix through-flow method, and Smith (1966) developed the streamline curvature method. Streamlines are defined as lines which are tangent to the velocity vectors throughout the flow field. The method used in the current approach to determine the flow field is a streamline curvature method developed by Hearsey (1994) and is similar to the one developed

by Smith (1966). The SLCC is a computer program that solves an axisymmetric, annular flow field. The flow is assumed to be an inviscid, perfect gas with no transfer of mass, momentum, or energy between adjacent streamlines.

The inputs required by the SLCC are the overall annulus geometry, blade geometry, and a radial distribution of inlet total temperature, total pressure, swirl angle, and loss and deviation correlations which are sensitive to the local flow field. The annulus geometry is divided into a series of axial stations that need not necessarily be radial but may be leaned, or inclined, at an angle with respect to the radial direction to facilitate placement at locations of interest, such as the leading- and trailing-edge blade angles. Initial estimated streamlines are then set up radially to create a computational grid. The slope of the streamlines are assumed to be zero far from the bladed regions at the inlet and exit. A schematic of the SLCC inputs and how the annulus is divided into a computational grid is illustrated in Figure 3.1.

A computing station is defined by the computational grid. A sketch of the computing station is shown in Figure 3.2. In this figure, r is the radial direction, z is the axial direction, l is the computing station direction, m is the meridional direction, r_c is the radius of curvature of the streamline, γ is the station lean angle, and ϕ is the streamline slope angle.

The velocity triangle nomenclature used in the SLCC is presented in Figure 3.3. The meridional velocity (V_m) is the base velocity, defined as the vector sum

of the axial and radial velocity components. One limitation of the streamline curvature method (Smith 1966) is that the velocities in the absolute reference plane must be subsonic. The relative Mach numbers have no restrictions. Alpha (α) is the absolute flow angle and is defined as the angle between $\mathbf{V}_m$ and the absolute velocity, $\mathbf{V}$. Beta (β) is the relative flow angle and is defined as the angle between $\mathbf{V}_m$ and the relative velocity ($\mathbf{W}$). $\mathbf{U}$ represents the wheel rotational velocity.

The following paragraphs briefly describe the solution technique of the SLCC. A complete derivation of the governing equations can be found in Appendix C. The SLCC assumes an inviscid, axisymmetric, adiabatic, steady-state flow with no body forces. The governing equations are continuity, circumferential momentum, axial momentum, radial momentum, energy, entropy and the ideal gas equation of state. Mapping the circumferential momentum equation to the non-orthogonal, m and l coordinate system reveals that angular momentum is constant along a streamline. As shown in Appendix C, mapping of the radial and axial momentum equations to the m and l coordinate system, in combination with the inclusion of the T-dS, energy, and entropy equations, reveals that the radial and axial momentum equations are equivalent. For this reason, the axial momentum equation is discarded.

Duct flow regions and bladed regions are solved by different equations. Both methods use the radial momentum equation, continuity equation, ideal gas equation of state, definition of static temperature, and the isentropic relationship

for static pressure. The other equations involved are used to calculate three closure parameters. These parameters are exit swirl velocity, exit total temperature, and exit total pressure.

The closure relations for duct flow regions are presented first. From integration of the circumferential momentum equation, energy equation, and entropy equation along a streamline, it is revealed that angular momentum, enthalpy, and entropy are constant along a streamline. This fact gives the three closure relations as

$$V_{\theta 2} = \left(\frac{r_1}{r_2} \right) V_{\theta 1}, \qquad [3.1]$$

$$T_{t2} = T_{t1}, \qquad [3.2]$$

$$P_{t2} = P_{t1}, \qquad [3.3]$$

where the subscripts 1 and 2 represent the inlet and exit to a computational station.

For a bladed region, the process is more complex. Angular momentum, enthalpy, and entropy are not constant along a streamline. Because of the complexity of the flows involved in the bladed region, the SLCC does not directly model the bladed region. Empirically derived loss and deviation correlations provide the relative total pressure loss coefficient and flow deviation across a bladed region. The relative total pressure loss coefficient is defined as the mass-averaged defect in relative total pressure divided by the pressure equivalent of the inlet velocity head,

$$\overline{\omega}' = \frac{\left(P'_{t2}\right)_{id} - P'_{t2}}{P'_{t1} - P_1}.$$ [3.4]

where $\left(P'_{t2}\right)_{id}$ is the ideal exit relative total pressure with no losses, P'_{t2} is the exit relative total pressure with losses, and the denominator is the relative inlet dynamic pressure head.

The deviation correlations provide the deviation of the exit flow angle, β_2, from the blade metal angle, β_{2m},

$$\delta = \beta_2 - \beta_{2m}.$$ [3.5]

The correlations for both loss and deviation are experimentally derived and described in detail in Section 3.2.

With loss and deviation provided by the correlations at each streamline, the closure relations that specify the change in enthalpy, entropy, and angular momentum across a blade row are developed. The relations are derived in Appendix C. The final relations are

$$V_{\theta 2} = V_{m2} \tan \beta_2 \cos \phi_2 + U_2,$$ [3.6]

$$T_{t2} = T_{t1} + U_2 \left[V_{\theta 2} - \frac{r_1}{r_2} V_{\theta 1} \right] \frac{1}{c_p},$$ [3.7]

$$P_{t2} = P_{t1} \left(\frac{T_{t2}}{T_{t1}} \right)^{\frac{\gamma}{\gamma-1}} \left[1 - \left(\frac{P'_{t1}}{P'_{t2}} \right)_{id} \overline{\omega}' \left(1 - \left[\frac{1}{1 + \frac{\gamma-1}{2} \left(M'_1\right)^2} \right]^{\frac{\gamma}{\gamma-1}} \right) \right].$$ [3.8]

With the exit swirl velocity, exit total temperature, and exit total pressure determined, the conservation equations described in Appendix C for each case are solved to develop the entire flow field.

3.2 Correlations Used in the Streamline Curvature Code

Because of the complex physical flow occurring in a compressor stage, it is very difficult to model the flow phenomena exactly. For this reason, empirical correlations are typically used to approximate the actual physics involved. Most of the correlations used in the SLCC were originally derived from 2-D linear cascade flow results and are found in NASA SP-36 (1965). These correlations were developed from databases acquired from machines of 1950's and 1960's design. Because they were developed on earlier designs, the correlations may have trouble when modeling machines with more modern blade profiles. However, some correlations have been modified to better approximate modern high speed turbomachines.

Before the loss and deviation correlations can be used, several geometric quantities must be known. These are the blade inlet and exit metal angles, solidity, camber, blade maximum thickness to chord ratio, and location of maximum camber point as a fraction of chord. With these quantities defined, two reference values are calculated using the equations found NASA SP-36 (Lieblein, 1965). The first parameter is the low-speed reference minimum-loss incidence angle given by

$$i_{ref} = (k_i)_{shape} (k_i)_{th} (i_0)_{10} - n\theta ,$$
[3.9]

where $(k_i)_{shape}$ and $(k_i)_{th}$ are correction factors for blades with shapes other than

NACA 65-(A_{10})-series blades and $(i_0)_{10}$ is the variation of zero-camber incidence

angle for the 10-percent-thick 65-series thickness distribution. $(i_0)_{10}$ is a function

of inlet air angle, β_1. This value is unknown at the time of calculation of i_{ref}, so it

is found iteratively. The term n is the minimum-loss-incidence slope factor. i_{ref} is

used in Equations [3.10] and [3.34] - [3.37].

The last reference value that must be found is the reference minimum-loss

air inlet angle. Assuming the minimum-loss incidence angle is zero, the reference

minimum-loss air inlet angle would be equal to the inlet blade metal angle.

However, Equation [3.9] calculates a reference minimum-loss incidence angle, so

a better initial estimate of the reference minimum-loss air inlet angle is

$$\beta_{1ref} = \beta_{1m} + i_{ref} .$$
[3.10]

β_{1ref} is used in Equations [3.13], [3.15], and [3.23].

3.2.1 Loss Correlations

The loss correlations calculate the relative total pressure loss coefficient,

$\overline{\omega}'$, defined by Equation [3.4]. The SLCC calculates loss at a given compressor

operating point by developing a "loss bucket". A loss bucket is the graphical

representation of loss as a function of incidence for constant Mach number. The

curve normally has a U-shape or bucket shape with the middle of the bottom of the

bucket being the minimum-loss incidence point. The equation that develops the loss bucket for the SLCC is

$$\overline{\varpi}' = \left[\left(\varpi_{min} + \varpi_M + \varpi_{hub} + \varpi_{tip} \right) \left[1 + \left(\frac{i - i_M}{W} \right)^2 \right] \right].$$ [3.11]

The first four terms are magnitudes of different loss values, i is the actual incidence, i_M is the minimum loss incidence, and W is an arbitrarily defined width of the loss bucket. i_M is a function of inlet relative Mach number and i_{ref} (defined by Equation [3.9]). An example of the loss bucket and how each term effects the bucket shape is shown in Figure 3.4. The solid line represents a baseline bucket. The baseline bucket is an arbitrary bucket that will be used as a baseline to depict how the other variables affect the bucket. With increasing minimum incidence (i_M), the bucket shifts to the right. With increasing magnitude of loss terms (ϖ_{min}, ϖ_M, ϖ_{hub}, ϖ_{tip}), the bucket shifts up. As the width term (W) decreases, the bucket width decreases.

The minimum loss term, ϖ_{min}, is essentially the profile loss, or friction loss, caused by viscous forces on the blade. The one used for this investigation is proposed by Robbins et. al. (1965) in NASA SP-36. The correlation for minimum profile loss is given as

$$\varpi_{min} = \varpi_{vloss} \left(\frac{2P\sigma}{\cos \beta_{2ref}} \right)$$ [3.12]

where ϖ_{vloss} is an input loss modification term. The P term in Equation [3.12] is interpolated from a data set developed from Figure 3.5. The abscissa for Figure 3.5 is the design diffusion factor, D_{des}. The diffusion factor used in the SLCC is based on flow-weighted mean inlet and exit axial velocities and the outlet flow angle plus the deviation due to mean axial velocity changes. Equation [3.13] shows this relationship

$$D_{des} = 1 - \frac{V_{a2}}{V_{a1}} \frac{\cos \beta_{1ref}}{\cos(\beta_{2ref} + \delta_{vamn})} +$$

$$\left[\frac{2(r_1 V_{a1} \tan \beta_{1ref} - r_2 V_{a2} \tan(\beta_{2ref} + \delta_{vamn}))}{r_1 + r_2} + \frac{2\pi N_s}{30}(r_2 - r_1) \right] \times$$

$$\left[\frac{\cos \beta_{1ref}}{2 V_{a1} \sigma} 2(0.45 + 0.5(t/c)_{max}) \right] + 5.0(t/c)_{max}^2 . \qquad [3.13]$$

where V_a is the axial velocity, δ_{vamn} is the deviation due to mean axial velocity defined similar to Equation [3.21] except using V_a instead of V_m, and N_s is the rotational wheel speed in terms of revolutions per minute (rpm).

The next loss correlation to be examined is the loss due to a strong shock in the passage. The model for shock loss is the one presented by Miller, Lewis, and Hartman (1960). The inlet critical Mach number is defined as the value of the inlet Mach number that will give supersonic flow somewhere in the blade passage. This value is found by assuming that the pressure coefficient corresponding to the minimum pressure point on the blade suction surface remains practically

unchanged up to the critical Mach number (Grewe, 1957). From this assumption, the following equation for critical inlet Mach number was derived (Al-Daini, 1986)

$$M_{1c}^{'2} = \left\{ \left[\frac{\left(V_{max}^{'}/V_1^{'} \right)^2}{\left(V_{max}^{'}/V_1^{'} \right)^2 + \left(\frac{2}{\gamma+1} \right)^{\frac{\gamma}{\gamma+1}} - 1} \right]^{\frac{\gamma-1}{\gamma}} - 1 \right\} \left(\frac{2}{\gamma-1} \right).$$ [3.14]

Because Equation [3.14] requires the ratio of maximum relative velocity to inlet relative velocity, the following correlation (Jansen and Moffat, 1967) was developed

$$\frac{V_{max}^{'}}{V_1^{'}} = 1 + 5 \left(t/c \right)^2 + \frac{\left[0.45 + 0.5 \left(t/c \right) \right] \left[\cos \beta_{1ref} \left(\tan \beta_{1ref} - \tan \beta_{2ref} \right) \right]}{\sigma}.$$ [3.15]

A schematic of the shock loss model is shown in Figure 3.6. If the inlet relative Mach number is larger than its critical value, a shock will exist somewhere in the blade passage. The shock will be a detached bow shock but, to simplify the problem, it is assumed to be a normal shock. The normal shock extends from the tip of the blade, normal to the mid-channel streamline, and intersects the following blade on the suction side, shown in schematically in Figure 3.6. The Mach number at point A in Figure 3.6 is assumed to be the inlet relative Mach number. The Mach number at B is found by using a Prandtl-Meyer expansion from the blade tip to the point of shock impingement. The expansion angle is approximated by

assuming the blade is a double-circular-arc (DCA) section. The shock Mach number, M_s, is an average of the inlet relative Mach number and the Mach number at point B. Solidity is important in this correlation because blade spacing will directly affect the point of shock impingement, hence affect the Prandtl-Meyer expansion angle. With the shock Mach number known, the loss coefficient associated with the shock given by Lewis, Miller, and Hartman is developed from normal shock and isentropic relations and is given as

$$\varpi_M = \frac{\left(\dfrac{(\gamma+1)M_s^2}{(\gamma-1)M_s^2+2}\right)^{\frac{\gamma}{\gamma-1}}\left(\dfrac{\gamma+1}{2\gamma M_s^2-(\gamma-1)}\right)^{\frac{1}{\gamma-1}}-1}{\left(1+\dfrac{(\gamma-1)}{2}M_1'^2\right)^{\frac{\gamma}{\gamma-1}}-1}.$$ [3.16]

The last two loss terms in Equation [3.11] are the losses due to hub and tip effects, such as intense and concentrated vorticity in the flow. Because the rotors centrifuge some boundary-layer/wake flow radially outwards, increased losses appear at the tip (Hearsey, 1994). Hearsey also states that some experimental data shows an increase in the loss coefficient near the hub that is not accounted for by the other correlations. Therefore, he includes the ϖ_{hub} term. Both ϖ_{tip} and ϖ_{hub} are simply cubic functions of radius that add loss at both the hub and tip in proportion to user inputs, H_{loss} and T_{loss}. The equations for hub and tip loss are given as

$$\varpi_{hub} = \varpi_{min} H_{loss}\left(1-2\frac{r-r_{hub}}{r_{tip}-r_{hub}}\right)^3,$$ [3.17]

$$\varpi_{tip} = \varpi_{min} T_{loss} \left(2 \frac{r - r_{hub}}{r_{tip} - r_{hub}} - 1 \right)^3 . \qquad [3.18]$$

Hearsey suggests both H_{loss} and T_{loss} to be zero for stationary blade rows. For a rotor, he suggests H_{loss} be set to match experimental data and T_{loss} be set to one for the first rotating blade row and decreased by 0.2 for each rotating blade row afterwards until it also is zero.

3.2.2 Deviation Correlations

The deviation correlations represent the deviation in flow angle from the actual blade trailing edge or exit metal angle (Figure 3.7). Such deviations are caused by thick or separating boundary-layers, usually on the suction side of the blade. Like loss, there are several different reasons for deviation to occur. Five specific reasons will be investigated in this section. The total deviation is assumed to be representable as a linear combination of the five reasons. The total deviation is given as

$$\delta = \delta_{ref} + \delta_{va} + \delta_{3D} + \delta_m + \delta_i . \qquad [3.19]$$

The first deviation correlation investigated (Lieblein, 1965) is the low-speed reference minimum loss deviation angle

$$\delta_{ref} = \left(k_\delta \right)_{shape} \left(k_\delta \right)_{th} \left(\delta_0 \right)_{10} + \theta \frac{m + \frac{1}{2} \left(a/c - \frac{1}{2} \right)}{\sigma^b} \qquad [3.20]$$

where $(k_\delta)_{shape}$ and $(k_\delta)_{th}$ are correction factors for blades with shapes other than NACA 65-(A_{10})-series blades and $(\delta_0)_{10}$ is the variation of zero-camber deviation

22

angle for the 10-percent-thick 65-series thickness distribution. $(\delta_0)_{10}$ is a function of inlet air angle, β_1. The term m is the deviation slope factor and b is the solidity exponent. The equation for δ_{ref} varies from the original one presented by Lieblein. A modification to it based on previous empirical data (Carter, 1946) made δ_{ref} a function of (a/c), the point of maximum camber as a fraction of chord.

The next deviation correlation is based on axial velocity ratio (Horlock, 1967-68). Horlock states that because of the growth of end wall boundary layers, the pressure increase (by diffusion) in the blade row is decreased, resulting in an axial velocity ratio that is different from the design. Thus, the axial velocity ratio will, in general, not be unity. Figure 3.8 shows how the streamline contraction across a blade row causes the streamtube area to change. With mass not allowed to cross a streamline, the streamtube area contraction requires that the axial velocity must increase (i.e. diffusion is reduced). With the axial velocity ratio larger than one, he noted the deviation actually decreases. Therefore, he presented this correlation

$$\delta_{va} = 10\left(1 - \frac{V_{m2}}{V_{m1}}\right).$$
[3.21]

The third deviation correlation is the deviation due to streamline radial location. Because of complex, three-dimensional flows at the blade hub and tip, the deviation at these locations can be different from the deviation at the mid-span. This correlation (Robins, Jackson, and Lieblein, 1965), δ_{3D}, accounts for some of

these effects. For high-speed sections, or blades with a DCA profile, δ_{3D} is interpolated from Figure 3.9. In this figure, δ_{3D} is a function of the inlet relative Mach number and percent of blade height from compressor tip. For low-speed sections, or blades with NACA 65-(A$_{10}$)-series sections, δ_{3D} is equal to –0.5 degrees for blade height greater than 50-percent of blade height from compressor hub. For all other radial locations of NACA 65-(A$_{10}$)-series sections,

$$\delta_{3D} = -\frac{1}{2} + 9\frac{3}{8}\left(\frac{1}{2} - \frac{r - r_{hub}}{r_{tip} - r_{hub}}\right)^2 . \qquad [3.22]$$

The existence of a shock in the blade passage is another source of deviation. This correlation is only used if the inlet relative Mach number is larger than one. The development of this correlation involves knowledge of the inlet and exit critical Mach numbers and the inlet and exit axial velocities. The inlet critical Mach number is presented in Equation [3.14]. In the same paper (Jansen and Moffat, 1967), the exit critical Mach number, the inlet and exit critical velocities, and the inlet and exit axial velocities are derived. The exit critical Mach number,

$$M'_{2c} = M'_{1c}\frac{A_1}{A_2}\frac{\cos\beta_{1ref}}{\cos\beta_{2ref}}\left[\frac{1 + \frac{\gamma - 1}{2}M'^2_{2c}}{1 + \frac{\gamma - 1}{2}M'^2_{1c}}\right]^{\frac{\gamma+1}{2(\gamma-1)}} , \qquad [3.23]$$

is solved iteratively across the blade and used to calculate the exit critical velocity. The exit critical Mach number is also used to calculate the exit axial velocity. The inlet and exit critical velocities given by Jansen and Moffat are

24

$$V'_{1c} = \frac{\sqrt{\gamma R T'_t}}{\sqrt{\dfrac{1}{M'^2_{1c}} + \dfrac{\gamma - 1}{2}}}$$ [3.24]

and

$$V'_{2c} = \frac{\sqrt{\gamma R T'_t}}{\sqrt{\dfrac{1}{M'^2_{2c}} + \dfrac{\gamma - 1}{2}}},$$ [3.25]

where T_t is the local relative total temperature.

The inlet axial velocity is found from

$$V_{1a} = \frac{\sqrt{\gamma R T'_t}}{\sqrt{\dfrac{1}{M'^2_1} + \dfrac{\gamma - 1}{2}}}.$$ [3.26]

Jansen and Moffat (1967) state that the relative velocity ratio is assumed unchanged for Mach numbers above the critical value, hence the exit axial velocity ratio can be found from

$$V_{2a} = V_{1a} \frac{V'_{2c}}{V'_{1c}}.$$ [3.27]

Finally, the exit relative Mach number can be calculated from

$$M'^2_2 = \frac{1}{\dfrac{1}{\left(\dfrac{V_{2a}}{\sqrt{\gamma R T'_t}}\right)^2} - \dfrac{\gamma - 1}{2}}.$$ [3.28]

The actual outlet flow angle caused by the inlet Mach number above the critical value is given by

$$\cos\beta_{2M} = \cos\beta_{1ref} \frac{A_1}{A_2} \frac{V_{1a}}{V_{2a}} \left[\frac{1 + \frac{\gamma-1}{2}M_2'^2}{1 + \frac{\gamma-1}{2}M_1'^2} \right]^{\frac{1}{\gamma-1}} .$$ [3.29]

The deviation due to the Mach number greater than one in the blade passage is then simply

$$\delta_M = \beta_{2M} - \beta_{2ref} .$$ [3.30]

The final deviation component is the deviation due to off-design incidence. To determine this value, the stalling and choking incidences must be known. The stalling incidence is the incidence at which a boundary-layer separation occurs over a large part of the blade, causing the blade to stall. The choking incidence is the flow incidence at which the flow in the blade passage becomes choked. The equations for stalling and choking incidence (Emery, Herrig, Erwin, and Felix, 1958) are

$$i_{stall} = i_{ref} + 1.5\left[10 + \frac{\theta(55 - \beta_{1m})}{150} \right]\left(0.5 + 5.0(t/c)_{max}\right)$$ [3.31]

and

$$i_{choke} = i_{ref} - \left[10 - \frac{\theta(\beta_{1m} - 40)}{450} \right]\left(0.5 + 5.0(t/c)_{max}\right) .$$ [3.32]

The equations for deviation due to incidence were constructed by Hearsey using existing cascade data (Horlock, 1958). These equations are divided into four parts, depending on the actual incidence angle. They are

$$\delta_i = \tfrac{1}{2}\frac{\partial\delta}{\partial i}\left(i_{choke} - i_{ref}\right), \qquad\qquad i \le i_{choke} \qquad\qquad [3.33]$$

$$\delta_i = \frac{\partial\delta}{\partial i}\frac{\left(i - i_{ref}\right)\left(i + i_{ref} - 2i_{choke}\right)}{2\left(i_{ref} - i_{choke}\right)}, \qquad i_{choke} < i \le i_{ref} \qquad [3.34]$$

$$\delta_i = \left(i - i_{ref}\right)\left[1 + \frac{\left(1 - \dfrac{\partial\delta}{\partial i}\right)\left(i + i_{ref} - 2i_{stall}\right)}{2\left(i_{stall} - i_{ref}\right)}\right], \qquad i_{ref} < i < i_{stall} \qquad [3.35]$$

$$\delta_i = i - i_{stall} + \tfrac{1}{2}\left(\frac{\partial\delta}{\partial i} + 1\right)\left(i_{stall} - i_{ref}\right), \qquad i \ge i_{stall} \qquad [3.36]$$

where $\dfrac{\partial\delta}{\partial i}$ is interpolated as a function of σ and β_{1ref} from a data set developed from Figure 3.10.

3.3 Data Reduction Techniques

Compressor performance characteristics enable a stage-by-stage analysis technique to describe the changes in the flow field across a stage. Performance characteristics are normally specified in the form of pressure ratio and temperature ratio, or pressure ratio and compressor or stage efficiency, as a function of a mass flow coefficient. The method used in this study is the total pressure ratio (Ψ^P) and total temperature ratio (Ψ^T) as a function of corrected mass flow (ϕ). Several other

methods for calculating total pressure and total temperature characteristics are given in Appendix D.

Because the data provided by the SLCC is a radial distribution of quantities defined on streamlines, a data reduction technique is required to generate 1-D performance characteristics. To satisfy the first law of thermodynamics, a mass-average technique must be used for total temperature reduction. However, several methods are available for total pressure ratio averaging. Oates (1988) offers three different averaging techniques for total pressure ratio. These three techniques are mass-average, stream thrust-average, and continuity-average. The mass-average technique was chosen for this study because of its simplicity. The mass-averaging technique is explained next.

The mass flow between two streamlines is calculated in the SLCC. A linear interpolation between the characteristics on the streamline that defines the top of the streamtube and the streamline that defines the bottom of a streamtube is performed to find the characteristic ($PR_{t,n}$, $TR_{t,n}$) in the center of the streamtube. Equations [3.37] and [3.38] show the reduction used to get a 1-D representation for pressure and temperature characteristics,

$$\Psi^P = \frac{1}{2}\sum_{i=1}^{n}\frac{m_i}{m_t}\left(PR_{t,i} + PR_{t,i+1}\right) \tag{3.37}$$

$$\Psi^T = \frac{1}{2}\sum_{i=1}^{n}\frac{m_i}{m_t}\left(TR_{t,i} + TR_{t,i+1}\right). \tag{3.38}$$

In Equations [3.37] and [3.38], the n index is the number of streamtubes and m_t is

the total mass flow through the machine. Figure 3.11 illustrates how this reduction

is done.

4.0 CALIBRATION AND RESULTS FOR NASA ROTOR 1B

To develop the method for generating compressor performance characteristics, a calibration of the SLCC for one machine was required to determine the predictive behavior of the loss and deviation correlations. The machine chosen to do the initial calibration was the NASA Rotor 1B compressor that operated in the General Electric House Compressor Test Facility, Lynn, Massachusetts, as described in Section 4.1. The following sections will discuss the characteristics of NASA Rotor 1B and its test setup, the calibration technique of the SLCC, and the results of the calibration for Rotor 1B.

4.1 Experimental Data for NASA Rotor 1B

NASA Rotor 1B (Seyler and Gostolow, 1967) was chosen as the initial calibration machine for this approach for several reasons. Rotor 1B is a single blade row machine with no inlet or exit guide vanes to alter the flow. The data provided in the report consists of extensive radial distributions of several flow quantities to compare with the SLCC predicted results. With only one blade row to calibrate, the effects of the calibration quantities would be easier to discern. NASA Rotor 1B is a transonic machine that has a combination of double-circular-arc (DCA) and multiple-circular-arc (MCA) blade shapes. These qualities are similar to those of modern military fans.

4.1.1 Characteristics of NASA Rotor 1B

NASA Rotor 1B was designed in the mid-1960's to advance the level of knowledge of high speed, high stage loading turbomachines. With the development of a workable titanium alloy, blades were strong enough to have tip speeds beyond 1400 feet per second, where shock losses, due to high relative Mach numbers, are important.

The blades of Rotor 1B were designed with a DCA profile from the hub to approximately 60-percent span. The DCA profile is composed of circular-arc upper and lower surfaces. The arc for each surface is drawn between the point of maximum thickness at mid-chord and the tangent to the circles of the leading- and trailing-edge radii (Lieblein, 1965). A MCA camber line was used from 60-percent span to the tip. The MCA profile is similar to a DCA profile except that the two circular arcs are mutually tangent at the point directly across the flow passage from the leading edge of the adjacent blade that forms the other side of the flow passage, instead of at the mid-chord (Seyler and Gostolow, 1967). The rotor tip diameter was 36.5 inches with a hub-tip ratio of 0.50, a tip solidity of 1.30, and a hub solidity of about 2.45. A mid-span damper was employed to maintain the structural integrity of each blade. The rotor had a medium aspect-ratio, a tip speed of 1400 feet per second, and a diffusion factor of 0.35 at the tip. The machine had a total of 44 blades in the single blade row.

The design point for Rotor 1B was a flow of 215.49 pounds per second at a total pressure ratio of 1.60 and adiabatic efficiency of 0.858. The machine actually achieved a total pressure ratio of 1.638 and adiabatic efficiency of 0.895 at a flow of 219.2 pounds per second.

4.1.2 Test Facility

Rotor 1B was tested at General Electric's House Compressor Test Facility in Lynn, Massachusetts. The test rotor drew air from the atmosphere through two banks of filters. The first filter bank was designed to remove 22 percent of the particles in the air larger than abut three microns. The second filter was designed to remove 90- to 95- percent of the remaining particles of the same size. The air then went through a coarse wire foreign object damage (FOD) screen, a bell-mouth, and a flow straightener. An area contraction of 2.24 occurred between the flow straightener exit and the inlet face of the test rotor. Outlet guide vanes (OGV) far downstream of the rotor were used to de-swirl the flow leaving the test facility. The exit flow was then split into two flows, each of which was passed through a venturi for flow measurement, and then exhausted to atmosphere. The test rotor was powered by a high-pressure, non-condensing steam turbine rated at 15,000 horsepower.

4.1.3 Instrumentation

Inlet conditions to Rotor 1B were measured using 24 thermocouples distributed on the inlet screen and 6 pitot-static rakes of seven elements each

placed at centers of equal annulus areas located 14 inches downstream of the flow straightener. Blade element data was recorded at five radial positions using transverse probes. These measurements were taken at 10-, 30-, 50-, 70-, and 90-percent of the annulus height. Immersion of the transverse probes at other instrumentation points were established to correspond to the radial location at which the design streamlines would pass the instrumentation planes. Several static pressure taps were located on the casing and hub throughout the flow path. Static pressure was measured at only one circumferential location, except at the axial stations where the traverse probes or rakes were located. There, the static pressure was measured at more than one circumferential location. The thermocouple rakes and static pressure wedges were calibrated for Mach number effects and were sufficiently insensitive to small pitch and yaw effects. The test configuration and instrument location can be seen in Figure 4.1.

4.2 Calibration Technique for NASA Rotor 1B

Four calibration quantities were chosen by the author as the means to calibrate the SLCC to Rotor 1B performance. These were radial variations of additional loss, additional deviation, inlet blade blockage, and exit blade blockage. Additional loss and deviation parameters correct the predicted loss and deviation to experimental data. The T_{loss} term was used as suggested in Section 3.2.1. The H_{loss} term mentioned in Section 3.2.1 wasn't used because it could not be adjusted to correctly match experimental data at the hub. With the predicted loss and

33

deviation matching experimental data, the other predicted flow field quantities were much closer to experimental data. The radial distributions of inlet and exit blade blockages were used to achieve the best match between predicted blade row effects on the flow and the experimental data.

Because no experimental error was available in the experimental data for Rotor 1B, it was speculated that if the SLCC results were within one-percent of experimental data, it would be within the experimental data error band. Therefore, the goal in the calibration effort was to determine the exit total pressure and exit total temperature to within one-percent of the data.

The results of each calibration step are presented in this section to show how each step in the calibration effort was an improvement over the previous step. The quantities discussed are loss, deviation, exit absolute Mach number, exit relative Mach number, exit absolute swirl velocity, exit relative swirl velocity, exit total pressure, exit static pressure, exit total temperature, and exit static temperature. These parameters were chosen because they give a complete description of the change in the flow field through a bladed region in terms of changes occurring in the absolute, relative, total, and static reference frames. Therefore, they give a good overall picture of machine performance.

The three levels of calibration in the calibration effort are denoted uncalibrated, partially calibrated, and calibrated. The results of the SLCC with no calibration are presented as a baseline (uncalibrated) to see how well the uncorrected correlations and the SLCC performed to predict blade row

performance. Figure 4.2(a) illustrates how this method of calibration was conducted. The only input was geometry. The SLCC was then allowed to run with only the correlations used to predict the results.

Next, because experimental loss and deviation were available from the Rotor 1B data, the SLCC was altered to accept loss and deviation as user inputs. The correlations were still allowed to calculate a loss and deviation at each streamline. The difference between the loss and deviation predicted by the correlations and experimental loss and deviation was included as add-loss and add-deviation. Performance results with only the loss and deviation corrections utilized are referred to as the partially calibrated results. Figure 4.2(b) illustrates how this calibration was conducted. Geometry, experimental loss, and experimental deviation were input to the SLCC. The results of this run yielded add-loss and add-deviation as described above. The geometry, add-loss, and add-deviation were then input into the SLCC to yield the final results.

The last calibration step was the fully calibrated step. For this step, geometry, add-loss, add-deviation, inlet blade blockage and exit blade blockage were input to the SLCC. The SLCC results were then compared to experimental results. If the results were within the predetermined one-percent tolerance, the results were denoted as final results. If the results were outside of the one-percent tolerance, the blockage terms were adjusted and the SLCC was initiated again. This was an iterative process to adjust the blockage terms. The process for the

fully calibrated step is illustrated in Figure 4.2(c). The performance results with all four calibration parameters included are referred to as the calibrated results.

4.2.1 Description of Calibration Points and Figures

The results of the calibration are shown in Figures 4.3 through 4.12. Each of the three calibration steps is shown in comparison to experimental data. The experimental data is displayed with black diamonds, the uncalibrated results are represented with a green dot-dashed line, the partially calibrated results are shown with a dashed red line, and the fully calibrated results are shown with a solid blue line. Table 4.1 summarizes the percent difference between experimental data and the results from each of the three calibration steps. The loss results in Table 4.1 are given in absolute error instead of percent error because the values are so close to zero that percent differences would give an unclear representation of the results.

Although the results were predicted for 50-, 70-, 90-, and 100-percent design speeds and numerous mass flows along each speed line, only one speed and flow point is shown for comparison. The point chosen is on the 100-percent speed line with a corrected mass flow of 216. 31 lb_m/s. This point was chosen because the 100-percent speed line represented the most difficult speed to calibrate (apparently due to the transonic flows relative to the blade causing increase shock losses). The chosen point is also in the middle of the speed line, and considered to be typical of most points along the 100-percent speed line. Predictions at other speeds were typically better than the ones presented in this section.

4.2.2 Discussion of Calibration Results

The uncalibrated results for the relative total pressure loss coefficient, shown in Figure 4.3, show that the correlations significantly over-predict the loss around the hub. Rotor 1B has a hub solidity approaching 2.5. The correlations are only reliable up to a solidity of about 2.0. Beyond 2.0, the correlations become unstable. This is why the loss was over-predicted at the hub. However, the uncalibrated predictions are closer toward the tip. For both the partial calibration and full calibration steps, the loss is specified. The loss is still in error by a small amount (0.013 and 0.014, respectively) as opposed to −0.15 for the uncalibrated prediction. This error in the partially and full calibration prediction is partly due to interpolation and extrapolation of experimental data. Interpolation and extrapolation are required since experimental loss data is given at only five radial locations across the flow. Losses at locations of the streamlines predicted by the SLCC were interpolated or extrapolated from the five experimental points. The partially calibrated and calibrated results in Figure 4.3 lie nearly on top of each other.

Figure 4.4 shows that the correlations under-predict the deviation at the hub, and again, do better near the tip for the uncalibrated step. These results are somewhat expected because the correlations, for the most part, were developed from linear cascade theory and experience and the flow phenomena occurring at hub and tip regions are highly three-dimensional. For the partially calibrated and

fully calibrated results, where the deviation is specified, the predictions shows a 30-percent improvement over the uncalibrated results. The predicted results differ, in part, from the experimental data also because of required interpolation or extrapolation of theoretical results from experimental data.

Exit absolute Mach number, shown in Figure 4.5, is fairly constant across the radius of the machine. The uncalibrated values differ from experiment by a maximum of -3.87-percent in the hub region. With the partial calibration, an improvement of 1.73-percent is gained in the prediction over the uncalibrated run. The complete calibration prediction gives a slightly better improvement to a -1.93-percent difference from experimental data.

The exit relative Mach numbers, shown in Figure 4.6, differ from experiment by 9.88-percent at the compressor hub for the uncalibrated case. In the tip region, the values more closely follow the actual data. The partially calibrated prediction improves by more than 50-percent over the uncalibrated error. The fully calibrated predictions exhibit an error of 3.79-percent for the exit relative Mach number.

The exit absolute swirl velocity is one of the quantities needed by the SLCC to step across the bladed region. The radial distribution for it is shown in Figure 4.7. The prediction of the exit absolute swirl velocity for the uncalibrated case differs a substantial –11.05-percent from experiment in the hub region. This quantity is directly dependant on predicted deviation, which differs significantly from experiment at the hub. With loss and deviation specified, the error for the

partially calibrated case decreases to 8.06-percent at the tip. With the radial inlet and exit blockage included in the full calibration, the error comes down to a more reasonable −5.32-percent.

The exit relative swirl velocity is shown in Figure 4.8. For the uncalibrated case, the predicted values differ from experiment by a large amount, 22.70-percent at the hub. The partial and calibrated results are fairly close, with the calibrated results reducing the percent error by almost a factor of seven to 3.25-percent.

The exit absolute total pressure is shown in Figure 4.9. These values are one of the key factors in determining performance characteristics and are another of the closure quantities. Because loss is used directly in calculating this parameter, the exit total pressure is expected to differ from experimental data. The error in the uncalibrated run is 2.81-percent. However, with loss and deviation corrected, the error in the predicted exit total pressure is worse, with an error of −3.08-percent when compared to experiment. The results match much better at the hub, but miss more at the tip. The author interprets these results to mean that the inlet and exit radial blockages are additional important factors in determining exit total pressure. With a complete calibration, the percent error for exit total pressure compared to experimental data is −0.89-percent. This is within the 1.0-percent goal set earlier.

Figure 4.10 shows the exit static pressure. The uncalibrated run differs a maximum of 3.35-percent at the hub. The partial and calibrated runs lie nearly on top of each other until the radius approaches 16-inches. The partial results then

over-predict the data by over 2.0-percent. The complete calibration brings the maximum error to -0.56-percent at the radial location of about 16-inches.

The last of the closure quantities is the exit absolute total temperature, shown in Figure 4.11. The uncalibrated SLCC predictions differ by a maximum of −1.36-percent. The predicted temperature is high at the hub, low in the middle, and high at the tip. The partial calibration reduces the error to less than 1.0-percent. The final calibrated results for the exit total temperature differ from the experimental data by a maximum of 0.18-percent.

Exit static temperature is plotted in Figure 4.12. The uncalibrated results followed the same trends as the uncalibrated total temperature results. The maximum error for the exit static temperature for the uncalibrated case were within the one-percent goal. The partial and calibrated results showed slight improvements with a final percent error of only 0.10-percent.

In summary, only the value of the exit static temperature came in within the desired one-percent accuracy for the uncalibrated parameters. The results of the partial calibration typically showed significant improvements over the baseline correlation predictions alone. The final calibration showed small improvements over the partial calibration. Not all values tracked were less than the one-percent goal. However, the exit total pressure and exit total temperature are the main parameters used in compressor performance characteristic prediction and they were both within the one-percent goal. Again, the calibration point discussed in this section was for a high speed point where the correlations are expected to have

the most problems (because of transonic flow conditions). These results are typical for the 100-percent speed line. At lower speeds, the error between experimental and calibrated data points were typically lower than the point presented here.

4.3 Calibration Trends

The above calibration process was described for one speed and flow point only. However, this calibration method was also carried out for 50-, 70-, 90-, and 100-percent speeds at several mass flows from the stall line to the choking region for each speed. Several trends became apparent throughout this process. These trends are discussed in this section.

4.3.1 Trends Along the 100-percent Speed Line

A radial distribution of additional loss (add-loss) was included to calibrate the loss correlations to match experimental data. Add-loss is loss added (or subtracted) to the loss calculated by the correlations. The calculation of the add-loss term is described in Section 4.2. Add-loss was included at every experimental point on the map. The radial distribution of add-loss for the point at 100-percent speed is shown in Figure 4.13. There are seven different mass flows on this figure ranging from 204.79 lb_m/s to 221.81 lb_m/s. An eighth curve is also shown on the figure. It is a solid heavy black line that represents a least-squares curve fit to the data. As shown in Figure 4.3, the loss at the hub is over-predicted with the baseline correlations. Figure 4.13 clearly shows how the loss is subtracted at the

hub to account for this effect. From the mid-span to the tip, the additional loss term remains fairly constant. The higher mass flows do cause the additional loss to decrease toward the tip. The overall fit curve has a parabolic shape with negative values at the hub, increasing to positive values past the mid-span, and then decrease into the negative region again at the tip.

Additional Deviation (add-deviation) was the second quantity to be calibrated. Add-deviation is deviation added (or subtracted) to the deviation calculated by the correlations. The calculation of the add-deviation term is described in Section 4.2. Figure 4.14 shows the add-deviation data for 100-percent speed. The curves show lines of add-deviation for the same range of the mass flows investigated for the add-loss factor. Like the loss correlations, the deviation correlations apparently have the most trouble at the hub. The add-deviation curves also have a parabolic shape, with the largest values positive at the hub, decreasing to almost zero at the mid-span, and increasing again slightly at the tip. The lower the mass flow the less additional deviation needs to be added.

Figures 4.15 and 4.16 are plots of the radial inlet and exit blade blockage terms. These terms were added to adjust the physical area blockage of the blades in the flow field. For calibration purposes, the values were allowed to be either positive or negative. The positive values are easily explained as an actual physical blockage of the flow caused by a blade and its boundary-layers. The negative values, however, are not inherently obvious. The correlations used in the SLCC use the solidity of the bladed regions. This solidity increases toward the hub of the

compressor. The correlations used were only reliable to a solidity of about two. Near the hub, the value of solidity for Rotor 1B exceeds the value of 2.0 to a value of nearly 2.5. This causes the correlations predict unreasonable amount of loss at the hub. The negative values of blockage help to adjust for the effects of the high values of solidity and other 3-D flow effects that cause problems in the correlations. Static pressure and numerous velocity values were identified as the quantities most affected by blockage. An increase in blockage caused an increase in the local velocity and a decrease in the local static pressure. The inlet blockage of the blade row had little effect on the overall flow field. However, the entire flow field was very dependant on the exit blockage.

Figure 4.15 shows the inlet blockage used to completely calibrate the SLCC for Rotor 1B. Inlet blockage affected the inlet static pressure and temperature and velocity quantities but had little effect on the exit conditions. The inlet blockage at the hub is negative and increases to positive just before the mid-span. From the mid-span to the tip, the value of inlet blockage remains fairly constant at about 4.0-percent.

The exit blockage (Figure 4.16) was used to adjust the exit static pressure and the velocities. This calibration quantity seemed to be more important to overall calibration than the inlet blockage. The variation of exit blockage affected both inlet and exit conditions significantly. The shape of this curve is very similar to the inlet blockage except it increases more significantly at the tip. It is negative at the hub and increases to about zero, and remains around zero from about

20-percent to 80-percent span. Beyond 80-percent span, the blockage increases again. This increase in blockage decreases the predicted static pressure to match the experimentally determined static pressure. The fit line is again a least-square curve fit to all of the different mass flows along the given speed line.

4.3.2 Trends Over the Entire Machine

The calibration trends presented in the preceding section were duplicated for the entire machine. The trends presented in the previous section were fairly typical of the results seen at other speeds. The calibration results presented in Figures 4.17 through 4.20 are the fit lines for each speed and calibration quantity. To make the results easily applicable to another machine, the results are presented as a function of percent span instead of radius.

Figure 4.17 shows the radial distribution of the averaged add-loss for different speeds. Each curve has a similar parabolic shape, with the values largely negative around the hub, increasing to the mid-span, and then decreasing to the tip. The magnitude of add-loss decreases with decreasing machine speed. This is expected because most of the correlations used were originally developed for low speed machines. Around the mid-span, the curves for all the speeds converge around the same values.

The additional deviation is presented in Figure 4.18. It too has a parabolic shape, decreasing toward the mid-span and then increasing to the tip. The curves

again converge to similar values at the mid-span. The additional deviation needed typically decreases with decreasing speed.

Radial inlet blockage as a function of percent span is shown in Figure 4.19. All of the curves have similar shapes and similar magnitudes. They are largely negative at the hub, increasing toward the mid-span (where they are fairly constant), and increasing slightly at the tip.

The final calibration curves, exit blockage, are seen in Figure 4.20. Like the inlet blockage, the exit blockage curves are very similar in shape and magnitude. Each curve tends to have a negative value at the hub and increase to almost zero at the mid- span. From mid-span to tip, they increase at a much more aggressive rate than the inlet blockage. Each of the curves tends to lay almost on top of the others throughout the span except for the 70-percent curve.

4.4 Compressor Maps

With the predicted radial flow field of Rotor 1B calibrated, the computed flow fields were processed through a mass-averaged data reduction routine to reduce it to a 1-D representation. With the data in a 1-D form, it was possible to generate 1-D compressor characteristics. The characteristics presented are the total pressure ratio (PR) and total temperature ratio (TR) versus corrected mass flow for different speeds. These results are shown in Figures 4.21 and 4.22, respectively.

45

The pressure characteristic shown for 50-, 70-, 90-, and 100-percent design corrected speed are plotted in Figure 4.21. Corrected mass flow (ϕ) is on the abscissa and PR (Ψ^P) on the ordinate. The calibrated data matches the experimental data closely. The maximum percent error for every point on the 50-, 70-, and 90-percent speed lines is below one-percent. On the highest speed line, 100-percent, all points are below one-percent except for the highest mass flow point, which is in the choking region. The maximum percent error at this point is 2.63-percent. This point could not be completely calibrated. Any further adjustment to the calibration quantities would not allow the SLCC to converge to a solution. In general, the highest percent difference on a speed line is the point closest to choking. This is to be expected since the streamline curvature method has difficulty with choking (Cumpsty, 1989). The error also typically increases as the speed increases.

Figure 4.22 shows the temperature characteristics for 50-, 70-, 90-, and 100-percent corrected speed. The abscissa is again ϕ but the ordinate is TR (Ψ^T). These characteristics have the same general shape as the pressure characteristics, however the magnitudes are not quite as large. The errors followed trends similar to those for the pressure characteristic: errors tend to increase toward the choking region and as speed increases. The percent error at each point is under one-percent. The largest error, 0.67-percent is again at the choking point on the 100-percent speed line.

The next two figures show the 2-D characteristics. The characteristics are in the same form as the ones presented in Figures 4.21 and 4.22. However, the results are no longer a 1-D representation, but are broken into hub, mid-line, and tip regions. The percent span from the hub are 10-, 50-, and 90-percent. On the figures, diamonds represent the experimental data, a red dot-dash line represents the hub results, a solid blue line represents the mid-line, and a green dotted line represents the tip results.

Figure 4.23 shows the pressure characteristics. At lower speeds, 50- and 70-percent, the characteristic curves lie close to each other and are relatively flat. As the mass flow increases at the lower speeds, they diverge some but are still relatively close and flat. This means that at the lower speeds, there is little variation in work done across the span of the blade. At the higher speeds, the 90- and 100-percent lines, the character of the curves changes. The tip region begins to do more work at lower mass flows. As the mass flow approaches choked flow conditions, the characteristics converge. The characteristic curves at the hub tend to be flatter, while the tip drops off faster as the flow moves toward choke.

The percent error of pressure characteristics follows the same trends as for the 1-D representation. The maximum percent difference occurs at the points closest to choke for 100-percent speed at the tip. From looking at the 2-D pressure characteristics, the tip area seems to be more into the choking region than the mid-line or hub. Since the streamline curvature method has difficulty with choking, this point can be expected to be less accurate. The percent errors in all of the

pressure characteristics at the hub are less than 0.9-percent. The maximum percent error for the mid-line is 2.35-percent and 5.06-percent for the tip.

The temperature characteristics, shown in Figure 4.24, also follow the same trends as the pressure characteristics. At lower speeds, the curves are flatter and lie closer together. As speed increases, the hub, mid-line, and tip take on a different character. They again converge as the flow tends toward choked conditions. The maximum error for the entire temperature characteristics map is again at the 100-percent speed line at the point closest to choke in the tip region. The error at this point is 1.37-percent. The error for all other points on the map is less than 0.60-percent.

These results show that with the relative total pressure coefficient, deviation angle, and inlet and exit blockage calibrated in the SLCC, the flow field is approximated closely. With a calibrated flow field, the 1-D and 2-D characteristics are shown to be in good agreement with the experimental data. Therefore, a technique to predict stage-by-stage, pre-stall compressor performance characteristics has been developed.

5.0 PREDICTION OF NASA STAGE 35 COMPRESSOR MAPS

With NASA Rotor 1B calibrated, it was desirable to use the knowledge gained from that calibration to predict the performance of some other machine. An investigation was initiated to determine if the calibration trends discovered for NASA Rotor 1B are useful for calibrating a very different machine such as NASA Stage 35. The following section describes NASA Stage 35 and shows the radial and overall predictions and comparisons of the pre-stall compressor performance maps.

5.1 Experimental Data for NASA Stage 35

NASA Stage 35 (Reid and Moore, 1978) was chosen as the machine to predict performance by applying calibration trends gained by analysis of NASA Rotor 1B. Stage 35 is a single stage, two blade row machine designed in the mid-1970's. It was chosen because it has highly loaded, low aspect ratio blades that are typical in modern military high pressure compressor cores. There is also experimental data available to compare with the prediction. Rotor 1B is designed to be one of the rotors of a low speed compressor fan stage, while Stage 35 is designed to be the first stage of a core compressor. The rotor tip speed is similar to that of Rotor 1B. However, Rotor 1B is a moderate-aspect ratio machine whereas Stage 35 is a low aspect-ratio machine. These different characteristics will verify if similar calibration quantities will hold for dissimilar machines.

5.1.1 Characteristics of NASA Stage 35

NASA Stage 35 was designed in the mid-1970's for an investigation into the effects of blade aspect ratio and stage loading. Four machines were designed with identical rotor and stator solidity, rotational speeds, mass flows, and flow path geometry. Only the rotor aspect ratio and stage loading were varied. Stage 35 has a low-aspect ratio rotor and low pressure ratio design.

Both rotor and stator blades were designed with multiple-circular arc (MCA) profiles and low aspect ratios. The rotor tip diameter is 19.9 inches with a hub-tip ratio of 0.7. Because of the higher hub-tip ratio, no mid-span damper was used. The machine has 36 rotor blades and 46 stator blades. The tip solidity of the rotor and stator regions are both 1.3. The hub solidity for the rotor and stator is 1.77 and 1.48, respectively.

The design point for Stage 35 is a mass flow of 44.53 pounds per second at a stage total pressure ratio of 1.82. The peak rotor and stage efficiency are 0.872 and 0.845, respectively. The rotor tip speed is 1493 feet per second and has a maximum rotor diffusion factor of 0.48. The stator diffusion factor is 0.34.

5.1.2 Test Facility

Stage 35 was tested at NASA Lewis Research Center's Single-Stage Compressor Facility in Cleveland, Ohio. A schematic of the facility is show in Figure 5.1. Atmospheric air enters the facility from the roof and passes through a flow measuring orifice and into a plenum chamber upstream of the test section.

Air then passes through the test section and into the collector and exits the facility through a vacuum exhaust system.

5.1.3 Instrumentation

The radial distribution of flow conditions upstream of the rotor were determined using two combination probes and two $18°$ wedge probes. The combination probes measured total temperature, total pressure, and flow angle. The wedge probes measured static pressure and flow angle. The probes were automatically aligned in the flow direction with a null-balancing control system. Inner and outer wall static pressure taps were located at the same axial position as the survey probes. Chromel-constantan thermocouples were used to measure temperature. No data were taken between the rotor and stator because of the close blade spacing. A radial distribution of flow conditions at the stator exit was determined using the two combination and two wedge probes. The probes were also traversed circumferentially. The layout for locations of the combination probe, wedge probe, and wall static taps is shown in Figure 5.2. Station 1 is the station immediately in front of the rotor. Station 3 is the station directly behind the stator. The view of both stations is looking downstream in the flow.

The mass flow was measured by using a calibrated thin-plate orifice. The average of two Chromel-constantan thermocouples was used to obtain the orifice temperature. Orifice pressures were measured by calibrated pressure transducers. An electronic speed counter and magnetic pickup were used to measure rotational

speed. Estimated errors in the data based on inherent inaccuracies of the instrumentation and recording systems are shown in Table 5.1.

5.2 Radial Predictions and Compressor Maps

With the calibration trends discovered during the calibration of Rotor 1B, it was hoped the same trends for add-loss, add-deviation, inlet blockage, and exit blockage would hold true for Stage 35. This was, however, not the case. With the calibration results of Rotor 1B imposed on Stage 35, the results were unsatisfactory. Figure 5.3 shows the 1-D mass-averaged stage pressure characteristic for Stage 35 with Rotor 1B calibration trends imposed. The results are adequate for the 70-percent speed line but unacceptable for the 90- and 100-percent speed line. The maximum error in the pressure characteristic is –11.10-percent on the 100-percent speed line.

Figure 5.4 shows the 1-D mass-averaged stage temperature characteristic for Stage 35 with Rotor 1B calibration trends imposed. Like the pressure characteristic, the temperature characteristic is acceptable for the 70-percent speed line. However, the 90- and 100-percent speed line predictions are in disagreement with experimental data. The maximum error in the temperature characteristic is –3.41-percent on the 100-percent speed line.

It was discovered during the calibration of Rotor 1B that the percent error in the mass-averaged 1-D prediction was smaller than the prediction of a radial distribution. Because of this fact and the fact that the SLCC couldn't converge to

a solution at all flow points with Rotor 1B trends imposed on Stage 35, the conclusion was made that Rotor 1B calibration trends are not acceptable for Stage 35. Therefore, an investigation was conducted to explain why the Rotor 1B calibration trends would not hold true for Stage 35. The investigation revealed that the machines were too dissimilar in design for the same trends to be true for both. The major difference discovered was the solidity of the blade rows. Rotor 1B had a relatively high solidity, especially at the hub where it approached 2.5. The correlations used in the SLCC were only reliable up to a solidity of about 2.0. The calibration efforts for Rotor 1B were primarily to overcome the effects of the high solidity at the hub. Negative blockage values at the hub were required because of this high solidity. The hub solidity for Stage 35 peaked at about 1.8 for the rotor.

Another problem encountered in applying the correlations to Rotor 1B was the relatively high 3-D effects at the hub. The slope of the hub wall was significant. The slope of the wall was larger at the hub for Rotor 1B than for Stage 35. SLCCs are also known to have problems with lower hub-casing ratio fans (Cumpsty, 1989) because of the strong curvature in the meridional plane and the larger slope of the wall at the hub. Stage 35 has a 40.0-percent higher hub-casing ratio and a 30.6-percent smaller slope at the hub wall than Rotor 1B.

A final major difference between the two machines is the blade profiles. The majority of the Rotor 1B blade profile is the DCA design. Stage 35 blades were designed with the MCA design across the entire span of the blades. These

53

profile, solidity, and annulus wall shape differences were enough to disallow the same calibration trends to be used on the different machines. The Rotor 1B correlation corrections moved loss and deviation in the wrong direction for Stage 35. Therefore, it was decided to predict Stage 35 with the original, uncalibrated correlations. The correlations and the SLCC were intended for use on machines with an annulus geometry like Stage 35 more so than Rotor 1B. The results introduced in this section are for an uncalibrated prediction of Stage 35.

The results of the uncalibrated SLCC for a single run are presented next. The results displayed are for a case at 100-percent design speed and a mass flow of 44.69 lb$_m$/s. The results are broken into those at the exit of the rotor and those at the exit of the stator. The maximum difference presented in the figures is the percent difference between the experimental data and the SLCC results. Figures 5.5 through 5.14 are results at the exit of the rotor and Figures 5.15 through 5.22 are results at the exit of the stator.

Figure 5.5 displays the radial distribution of the relative total pressure loss coefficient for Stage 35 rotor. These results follow the trend of and nearly match the experimental data with no calibration. Figure 5.6 shows the comparison for the exit flow angle for Stage 35 instead of the deviation. The exit flow angles differ from the respective deviations by a constant, the blade metal angle at the exit. The exit flow angle results (Figure 5.6) deviate from the experimental data, especially at the hub. The maximum difference between experimental data and SLCC results for the exit flow angle is 26.23-percent at the hub. One explanation offered for

this variance in exit flow angle is the blade shape design. The correlations were developed, for the most part, on machines with DCA profiles, whereas Stage 35 has MCA profiles. Therefore, the result was that the SLCC couldn't match the deviation. Because compressor work is directly related to the exit flow deviation and deviation poorly predicted at the hub, the results at the hub for other rotor variables also differ from experimental data.

The exit Mach number and exit relative Mach number are shown in Figures 5.7 and 5.8, respectively. Both curves follow the trends of the experimental data very closely. The absolute Mach number error at the hub is due to the near-hub deviation being under-predicted. The maximum difference is –13.83-percent. The relative Mach number is closer to the experimental data. The maximum difference is about 4.0-percent and occurs at the blade mid-span.

The absolute and relative exit swirl velocities are discussed next. Figure 5.9 shows the exit swirl velocity. This parameter is also under-predicted at the hub because of the near-hub deviation error. The maximum difference is –14.12-percent. The exit relative swirl velocity, Figure 5.10, varies 20.60-percent at the hub. Because this is one of the closure quantities, the inaccuracy in this variable will cause the entire flow field to differ from the experimental data.

Figures 5.11 and 5.12 show the predicted and experimental exit total and static pressures, respectively. The total pressure is under-predicted at the hub, with a maximum percent difference of –8.84-percent. At the tip, the total pressure is over-predicted. The experimental data is much flatter than the predicted results.

The exit static pressure is in better agreement with experimental data with a maximum difference of -1.40-percent.

The exit total temperature, Figure 5.13, and exit static temperature, Figure 5.14, each follow the same trend as the exit total and static pressures. The total temperature is under-predicted at the hub by 2.72-percent and over-predicted at the tip. This is a result of the deviation being over-predicted at the hub and under-predicted at the tip. The static temperature is predicted to within one-percent and follows the experimental trends very closely.

Figures 5.15 through 5.22 show the results at the exit of the stator, the second blade row in Stage 35. Because the results of the rotor exit are in error, the inlet and exit flows of the stator will also be in error. Figure 5.15 shows the predicted relative total pressure loss coefficient. The SLCC predicts a very uniform loss across the span. The experimental results are a factor of two higher and not nearly as uniform. Unlike the rotor, the stator misses the exit flow angle (Figure 5.16) more at the tip than at the hub. This results from the error in the flow deviation prediction. The maximum error in the exit flow angle is –37.75-percent, or almost five degrees, at the tip.

Because the stator is a stationary blade row, the absolute and relative frames of reference are the same; therefore, no relative quantities are presented for the stator. The predicted exit Mach number in Figure 5.17 tends to increase toward the tip, as opposed to the experimental data which decreases toward the tip. The maximum percent difference in Mach number is almost 31-percent at the tip.

56

The stator is attempting to de-swirl the flow coming out of the rotor. This can be seen by comparing the stator exit swirl velocity (Figure 5.18) with the rotor exit swirl velocity (Figure 5.9). The stator swirl velocity is approximately five times lower than the rotor swirl. The predicted swirl velocity is lower than the experimental data. The lower predicted value occurred because the deviation was too low and as a result the flow was not turned enough.

Figures 5.19 and 5.20 show the stator exit total and static pressure, respectively. The stator total pressure is in better agreement than that of the rotor exit total pressure. The maximum percent difference is only –6.18-percent. The SLCC predicts a larger pressure at the tip than the experimental data. The static pressure (Figure 5.20) is less than the experimental data everywhere except at the hub. The maximum percent error is –3.30-percent.

The stator exit total temperature and static temperature are plotted in Figures 5.21 and 5.22, respectively. The total temperature trend is similar to the total pressure, under-predicted at the hub and mid-span and over-predicted at the tip. The static temperature closely follows the trend of the experimental data, only slightly offset. The maximum difference in the total and static temperatures are –2.71- and –2.34-percent, respectively.

Using the averaging technique to convert radial distributions of flow field variables into a 1-D representation, the total pressure and total temperature characteristics for Stage 35 were computed and are presented in Figures 5.23 and

5.24. The pressure characteristics, Ψ^P, are shown in Figure 5.23 for 70-, 90-, and 100-percent design corrected speeds. Each point of these results is a mass average of a radial distribution of SLCC results at the stage inlet and exit. The results shown in Figure 5.23 indicate that the overall performance characteristics follow the experimental curvature trend fairly well. The 90-percent curve follows the experimental data closely, with a maximum percent difference of only 4.31-percent. The 100-precent speed line had a maximum error of 5.04-percent. The 70-percent speed line has the highest maximum error, 6.42-percent, at the highest mass flow point. The maximum error of 6.42-percent for the uncalibrated correlations is almost twice as accurate as the 11.10-percent difference between experimental data and Stage 35 predictions with Rotor 1B calibration trends included (illustrated in Figure 5.3). Figure 5.23 clearly demonstrates that even though the radial distributions of compressor flow fields might be predicted with significant error, the mass-averaged results of the experimental and predicted results may be quite acceptable.

Figure 5.24 displays the temperature characteristics for Stage 35. These results again show the 90-percent speed prediction is better than at the other two speeds. The 70-percent speed line has a maximum error of 1.91-percent at the highest mass flow point. The 100-percent line has a maximum percent error of −2.26-percent at the stall limit. This error is smaller than the −3.41-percent error shown in Figure 5.4 for the case of Stage 35 with Rotor 1B calibration trends

included. The percent error for the mass-averaged 1-D temperature characteristic representation (Figure 5.24) is again better than the 2-D representation of the same data. Typically, the percent difference of error in the temperature characteristic is smaller than that of the pressure characteristic.

The last set of results presented for Stage 35 are the pressure and temperature characteristics at the hub, mid-line, and tip for the different speeds. The experimental data for the tip is represented by a diamond, the mid-line a circle, and the hub an X. The results for the tip are a dashed green line, midline a solid blue line, and the hub a red dot-dashed line. The pressure characteristic results are presented in Figure 5.25. The predictions for all three speed lines have the tip with the highest total pressure ratio, the mid-line with the next highest pressure ratio, and the hub with the lowest pressure ratio. The experimental results differ, however. At 100-percent speed, the mid-line has the highest pressure ratio. This is because Stage 35 was designed with a MCA blade profile for large stall margin. Because the tip is normally the first section to stall on a compressor stage, the tip was designed to be less highly loaded at the higher speeds. This characteristic is also present at the 90-percent speed. At 70-percent speed, the tip is the most highly loaded section.

The maximum percent error for the hub region is –6.22-percent on the 100-percent speed line. At the midline, the 70-percent speed line has the largest error of 5.59-percent. The largest error at the tip is 23.32-percent on the

90-percent speed line. The tip has the largest error because the correlations used were not able to handle MCA blade profiles very well.

Figure 5.26 shows the total temperature characteristic and has the same legend as Figure 5.25. The total temperature characteristic for Stage 35 exhibits different behavior than Rotor 1B. Stage 35 typically has the highest temperature ratio at the hub and the lowest ratio at the tip, whereas, Rotor 1B typically has the opposite distribution. The results predict the tip to have the highest temperature ratio and the hub the lowest at all speeds for Stage 35. This is again due the correlations which were developed for DCA blade profiles while Stage 35 has MCA profiles.

The maximum percent error for the hub region is –2.82-percent on the 100-percent speed line. In the mid-line region, the maximum error is –3.12-percent on the 100-percent speed line. The 100-percent speed line also has the maximum percent error at the tip. The error there is 6.17-percent. Typically, the temperature ratio percent error is smaller that of the pressure ratio error.

6.0 SUMMARY AND CONCLUSIONS

This chapter summarizes the results and conclusions of the work contained in this investigation. The summary of the results lists the highlights of the results of the calibration of Rotor 1B and the prediction of Stage 35 characteristics. The conclusions discuss the lessons learned and the significance of the results.

6.1 Summary of the Results

The purpose of this thesis was to develop a technique to generate stage-by-stage, pre-stall compressor performance characteristics by coupling an existing SLCC using open literature correlations for flow losses and deviations for bladed regions. The method was developed, one machine was calibrated, and one machine was predicted. The results of applying the method to the two machines are summarized below:

- A method to generate 1-D and 2-D compressor performance characteristics was developed.

- With calibration of relative total pressure loss coefficient, flow deviation, and inlet and exit radial blade blockage, the entire flow field can be predicted.

- A calibrated flow field for Rotor 1B gave a 1-D representation of compressor performance characteristics to within 3-percent.

- A calibrated flow field for Rotor 1B gave a 2-D representation of compressor performance characteristics to within 6-percent.

- The calibration trends of Rotor 1B imposed on Stage 35 gave unsatisfactory results, therefore Stage 35 was predicted using the original, uncalibrated correlations.

- An uncalibrated flow field for Stage 35 gave a 1-D representation of compressor performance characteristics to within 7-percent.

- An uncalibrated flow field for Stage 35 gave a 2-D representation of compressor performance characteristics to within 24-percent.

The following section discusses the conclusions of what was learned from the results.

6.2 Conclusions

Several important pieces of information were learned from the calibration and prediction of characteristics for Rotor 1B and Stage 35. The first conclusion is that, with the four quantities used in the calibration, a machine that does not meet all the constraints of the correlations can be calibrated if several important flow field quantities are known; in particular, radial distributions of loss, deviation, total pressure, and total temperature.

Another piece of knowledge gained is that it is easier to match a 1-D representation of characteristics than a 2-D representation. For Stage 35, the radial distribution of the flow field proved to be somewhat inaccurate for several flow field quantities.   With the radial distribution mass-averaged into a 1-D

representation, the results were in better agreement with the mass-averaged experimental 1-D performance quantities.

Solidity is a very important input quantity for the SLCC and the correlations used in this investigation. A look at the Rotor 1B uncalibrated results shows that the predicted relative total pressure loss coefficient is significantly too high for the high solidity region at the hub. The correlations were good for a solidity of less than two and the hub of Rotor 1B exceeded this value. The corrections applied to Rotor 1B, especially the negative inlet and exit blockage and negative loss at the hub, were able to correct for the inaccuracy of the loss and deviation correlations at the hub.

Annulus wall geometry also plays an important part in predicting characteristics using a SLCC. The hub geometry for Rotor 1B has a large slope associated with it. This large slope requires a large curvature of the streamlines across the blades. This leads to 3-D flow effects. The correlations were not designed to handle these or any other severe 3-D effects which led to a poor prediction of the loss and deviation at the hub.

The blade shape is also identified as an error contributor in the use of the deviation correlations. The correlations used in the SLCC were developed for the double-circular-arc (DCA) blade profile. Stage 35 blades use multiple-circular-arc (MCA) blade profiles. The loss for Stage 35 was predicted fairly accurately. The deviation was not. It is believed that this blade shape difference is the reason the

correlations could not accurately predict deviation for the MCA profiles of Stage 35.

Another key piece of knowledge is that the SLCC has much more difficulty with convergence as the machine approaches the choked condition. The addition of inlet and exit radial blockage also adds to the difficulty of convergence near choke. A point on the 100-percent speed line of Rotor 1B could not be completely calibrated because any additional blockage would cause the SLCC solution to diverge.

7.0 RECOMMENDATIONS

Although the calibration of the SLCC and loss and deviation correlations for Rotor 1B was extremely successful, the prediction of Stage 35 characteristics was less accurate. There were also several areas identified that could be improved or added to in future work on the same subject to make the stage characteristic method a more useful and better predictive tool. A summary of recommendations for future work is included below.

The first recommendation is to use the method to calibrate several more machines that have experimental data documented. It is apparent that the calibration of the method based on a fan blades cannot be imposed on a core compressor blade and get accurate results. Several fan rotors and stators, and several core compressor rotors and stators should be calibrated. The calibration trends should be investigated to see if fan blades of similar families all have similar trends and core blades of similar families have similar trends. A fan blade or core blade family should be defined by blades with similar design variables such as stage loading, relative Mach numbers, diffusion factors, and solidity. It also should be investigated to see if rotor blades and stator blades have similar calibration trends.

The next recommendation is to initiate an open-literature investigation to see if more correlations can be found to model blade rows with higher solidity, since modern machines are tending toward higher solidity.

Another recommendation is to conduct an open-literature investigation to see if there are correlations to handle additional types of blade profiles. The correlations in the SLCC used in this research were available for NACA 65-(A_{10}) series and double-circular-arc blade profiles. Blading on modern machines is becoming more complicated, and correlations should be found with these types of profiles if this is to truly be a predictive tool. If correlations cannot be found, corrections to these correlations could be found through calibration trends of several machines with the same types of blade profiles.

An alternative to the previous recommendation would be to develop correlations for blades with complex shapes by using 3-D CFD models. A database of performance variables for a family of complex blades could be gathered from simulations run at on- and off-design conditions. Correlations could then be developed from this database of information.

REFERENCES

REFERENCES

Al-Daini, A. J. "Loss and Deviation Model for a Compressor Blade Element." Int. J. Heat & Fluid Flow, March 1986.

Attia, M. S. and Schobeiri, M. T. "New Method for the Prediction of Compressor Performance Maps Using One-Dimensional Row-by-Row Analysis." ASME 95-GT-434, ASME International Gas Turbine and Aeroengine Congress and Exhibit, Houston, Texas, June 1995.

Carter, A. D. S. and Hughes, H. P. "A Theoretical Investigation into the Effects of Profile Shape on the Performance of Aerofoils in Cascades." British A.R.C,R&M No. 2384, 1946.

Cumpsty, N. A. *Compressor Aerodynamics*. Longman Scientific and Technical, England, 1989.

Cyrus, V. "Aerodynamic Performance of Rear Axial Compressor Stage with Annular Diffuser and Outlet Chamber." ASME 96-GT-238, ASME International Gas Turbine and Aeroengine Congress and Exhibit Birmingham, UK, June 1996.

Davis, M. W., Jr. and O'Brien, W. F. "Stage-by-Stage Poststall Compression System Modeling Technique." *Transactions of the ASME, Journal of Propulsion and Power,* Volume 7, Number 6, Nov.-Dec. 1991, pp. 997-1005.

Davis, M.W., Jr., Hale, A. A., Shahrokhi, K. A. and Garrard, G. D. "Euler Modeling Techniques for the Investigation of Unsteady Dynamic Compression System Behaivior" AGARD PEP 85th Symposium on Loss Mechanisms and Unsteady Flows in Turbomachines, Derby, UK, May 1995.

Emery J. C., Herrig, L. J., Erwin, J. R., and Felix, A. R. "Systematic Two-Dimensional Cascade Tests of NACA 65-Series Compressor Blades at Low Speeds." NACA Report No. 1368, 1958.

Garrard, G. D. "ATEC: The Aerodynamic Turbine Engine Code for Analysis of Transient and Dynamic Gas Turbine Engine System Operation." Ph.D. Dissertation, The University of Tennessee, Knoxville, TN, 1995.

Grewe, K. H. "Pressure Distribution Measurements on Two-Dimensional Cascades at High Subsonic Mach Numbers," Part 1. DFL report 57/6a, AFOSR TN 57-289, Institut für Strömungs-mechanik, Technische Hochschule, Braunschweig, Germany, March 1957.

Hah, C. and Wennerstrom, A. J. "Three-Dimensional Flow-Fields Inside a Transonic Compressor With Swept Blades." *Transactions of the ASME, Journal of Turbomachinery*, April 1991, pp. 241-251.

Hale, A. A. and Davis, M. W., Jr. "DYNamic Turbine Engine Compressor Code, DYNTECC – Theory and Capabilities." AIAA-92-3190, AIAA/SAE/ASME/ASEE 28th Joint Propulsion Conference, Nashville, TN, July 1992.

Hale, A. A., O'Brien, W. "A Three-Dimensional Turbine Engine Analysis Compressor Code for Steady-State Inlet Distortion." ASME 97-GT-124, ASME International Gas Turbine and Aeroengine Congress and Exhibit, Orlando, Florida, June 1997.

Hearsey, R.M. "Program HT0300 NASA 1994 Volume 2." The Boeing Company, 1994.

Horlock, J. H. *Axial Flow Compressors*. Butterworth Publications Limited, 1958.

Horlock, J. H. "Some Recent Research in Turbo-Machinery." *Proceedings of the Institute of Mechanical Engineers*, Volume 182, Part 1, No. 26, 1967-68, pp. 571-586.

Jansen, W. and Moffat, W.C. "The Off-Design Analysis of Axial-Flow Compressors." Transactions of the ASME, Journal of Engineering for Power, October 1967, pp. 453-462.

Johnson, M. S. "One-Dimensional, Stage-by-Stage, Axial Compressor Performance Model." ASME International Gas Turbine and Aeroengine Congress and Exhibit, Orlando, Florida, June 1991.

Klein, A. "Aerodynamics of Cascades." AGARDograph, 220, 1977, pp. 408-413.

Korakianitis, T. and Zou, D. "Through-Flow Analysis for Axial-Stage Design Including Streamline-Slope Effects." ASME 93-GT-56, ASME International Gas Turbine and Aeroengine Congress and Exhibit, Cincinnati, Ohio, May 1993.

Lieblein, S. "Chapter VI: Experimental Flow in Two-Dimensional Cascades." *Aerodynamic Design of Axial-Flow Compressors*, NASA-SP-36, 1965, pp. 183-226.

Marsh, H. "A Digital Computer Program for the Through-Flow Fluid Mechanics in an Arbitrary Turbomachine Using a Matrix Method." British A.R.C. R.&M. No. 3509, July 1966.

Mattingly, J. D. *Elements of Gas Turbine Propulsion*. McGraw Hill, Inc. 1996.

Miller, G. R., Lewis Jr., G. W. and Hartman, M. J. "Shock Losses in Transonic Compressor Blade Rows." *Transactions of the ASME, Journal of Engineering for Power*, July 1961, pp. 235-242.

Oates, G. C. Aerothermodynamics of Gas Turbine and Rocket Propulsion. AIAA Education Series, J. S. Przemieniecki, Series Editor-in-Chief, American Institute of Aeronautics and Astronautics, Washington, D.C., 1988.

Reid, L. and Moore, R. D. "Design and Overall Performance of Four Highly Loaded, High-Speed Inlet Stages for an Advanced High-Pressure-Ratio Core Compressor." NASA-TP-1337, 1978.

Robins, W. H., Jackson, R. J. and Lieblein, S. "Chapter VII: Blade-Element Flow in Annular Cascades." *Aerodynamic Design of Axial-Flow Compressors*, NASA-SP-36, 1965, pp. 227-254.

Sayari, N. and Bölcs, A. "A New Throughflow Approach for Transonic Axial Compressor Stage Analysis." ASME 95-GT-195, ASME International Gas Turbine and Aeroengine Congress and Exhibit, Houston, Texas, June 1995.

Seyler, D. R. and Gostelow, J. P. "Single Stage Experimental Evaluation of High Mach Number Compressor Rotor Blading Part 2 – Performance of Rotor 1B." NASA-CR-54582, September 1967.

Smith, L. H., Jr. "The Radial-Equilibrium Equation of Turbomachinery." *Transactions of the ASME, Journal of Engineering for Power*, January 1966.

Swan, W. C. "A Practical Method of Predicting Transonic-Compressor Performance." *Transactions of the ASME, Journal of Engineering for Power*, July 1961, pp. 322-330.

Tsalavoutas, A., Stamatis, A. and Mathioudakis, K. "Derivation of Compressor Stage Characteristics for Accurate Overall Performance Map Prediction." ASME 94-GT-372, ASME International Gas Turbine and Aeroengine Congress and Exhibit, Hague, Netherlands, June 1994.

Wu, Chung-Hau. "A General Theory of Three-Dimensional Flow in Subsonic and Supersonic Turbomachines of Axial-, Radial-, and Mixed-Flow Types." NACA TN 2604, January 1952.

Yazigi, N., Charlier, M. H., Gerolymos, G. A. and Chauvin, J. "Performance Prediction of Subsonic Separated Cascades." ASME 90-GT-65, ASME International Gas Turbine and Aeroengine Congress and Exhibit, Brussels, Belgium, June 1990.

APPENDICES

APPENDIX A

TABLES

Table 4.1. Error for Uncalibrated, Partially Calibrated, and Completely Calibrated SLCC Data. (All Given in Percent Except for Loss-Actual Error)

Quantity	Uncalibrated Error	Partially Calibrated Error	Calibrated Error
Loss	-0.15	0.013	0.014
Deviation	35.56	-6.48	-6.58
Exit Total Pressure	2.81	-3.08	-0.89
Exit Static Pressure	3.35	-2.04	0.56
Exit Total Temperature	-1.36	-0.68	0.18
Exit Static Temperature	0.70	-0.43	0.10
Exit Mach Number	-3.87	-2.14	-1.93
Exit Relative Mach Number	9.88	4.20	3.79
Exit Swirl Velocity	-11.05	-8.06	-5.32
Exit Relative Swirl Velocity	22.70	4.78	3.25

Table 5.1. Estimated Errors in Stage 35 Experimental Data.

Measurement Quantity	Estimated Error
Mass Flow	± 0.66 lbm/s
Rotational Speed	± 30 rpm
Flow Angle	± 1.0 deg
Temperature	± 1.1 °R
Rotor Inlet Total Pressure	± 0.01 psi
Rotor Inlet Static Pressure	± 0.04 psi
Stator Inlet Total Pressure	± 0.25 psi
Stator Inlet Static Pressure	± 0.15 psi

APPENDIX B

FIGURES
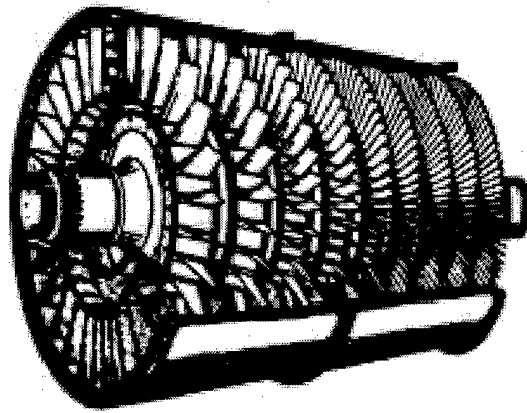
Figure 1.1. Typical Gas Turbine Compression System. (Mattingly, 1996)

Lines of Constant Corrected Speed

Stall Limit

Corrected Mass Flow Rate
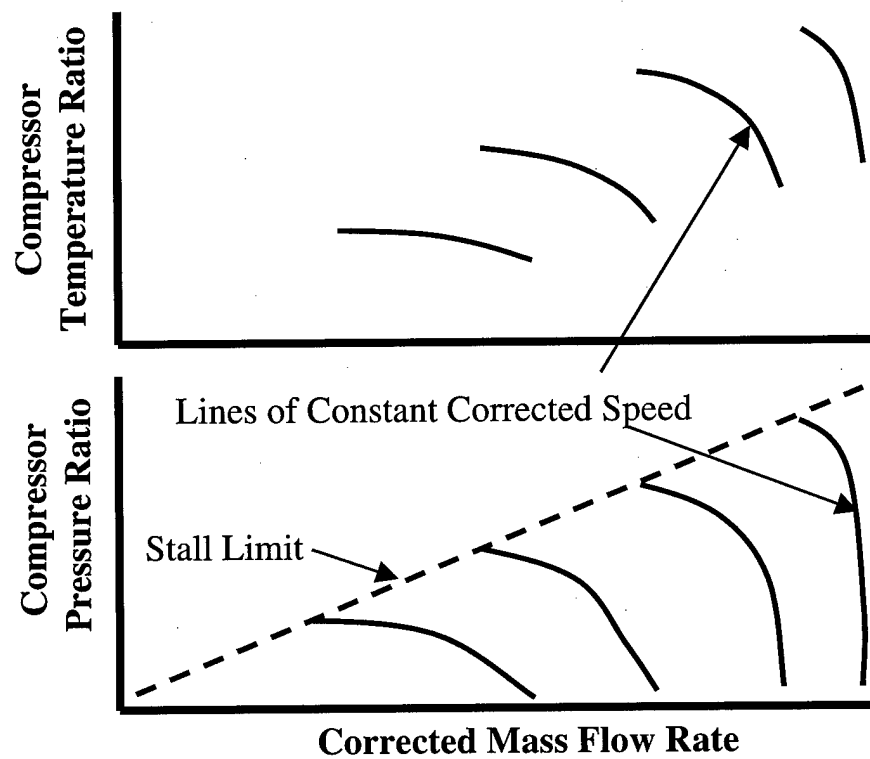
Figure 1.2. Representative Compressor Performance Map.
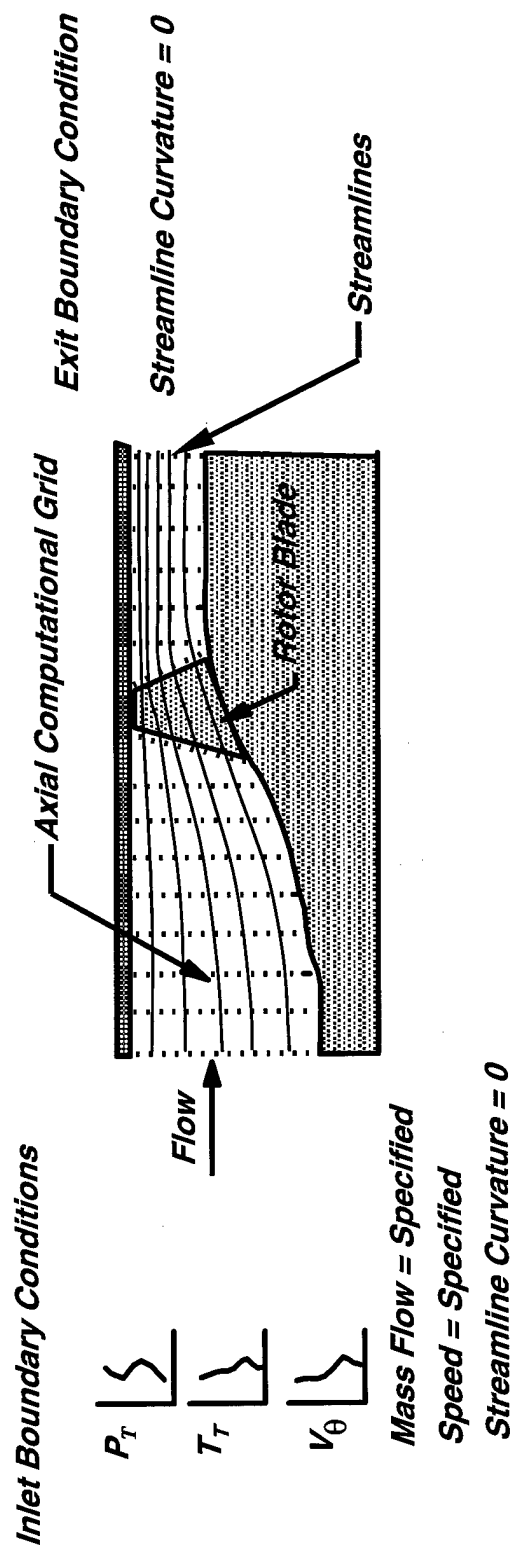
Figure 3.1. Schematic of SLCC Inputs.
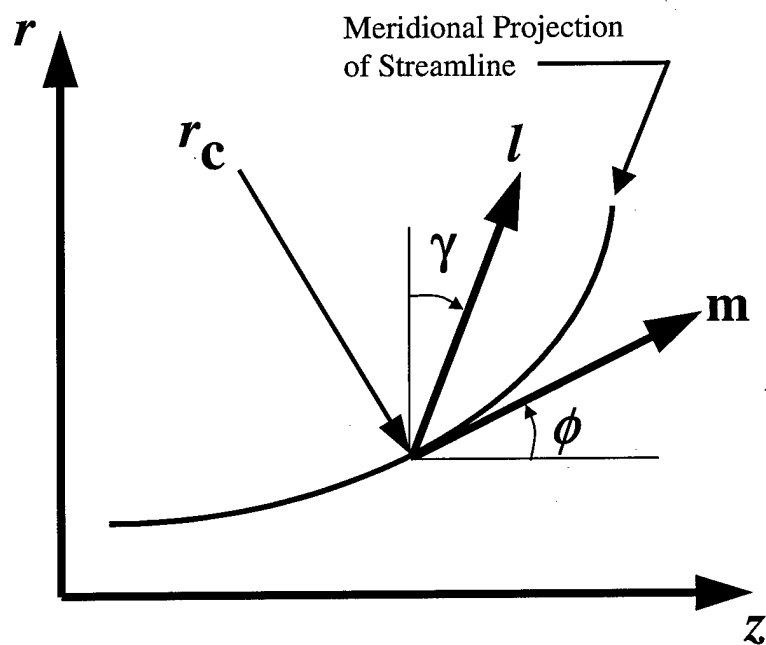
Figure 3.2. Geometry of Computing Station. (Hearsey, 1994)
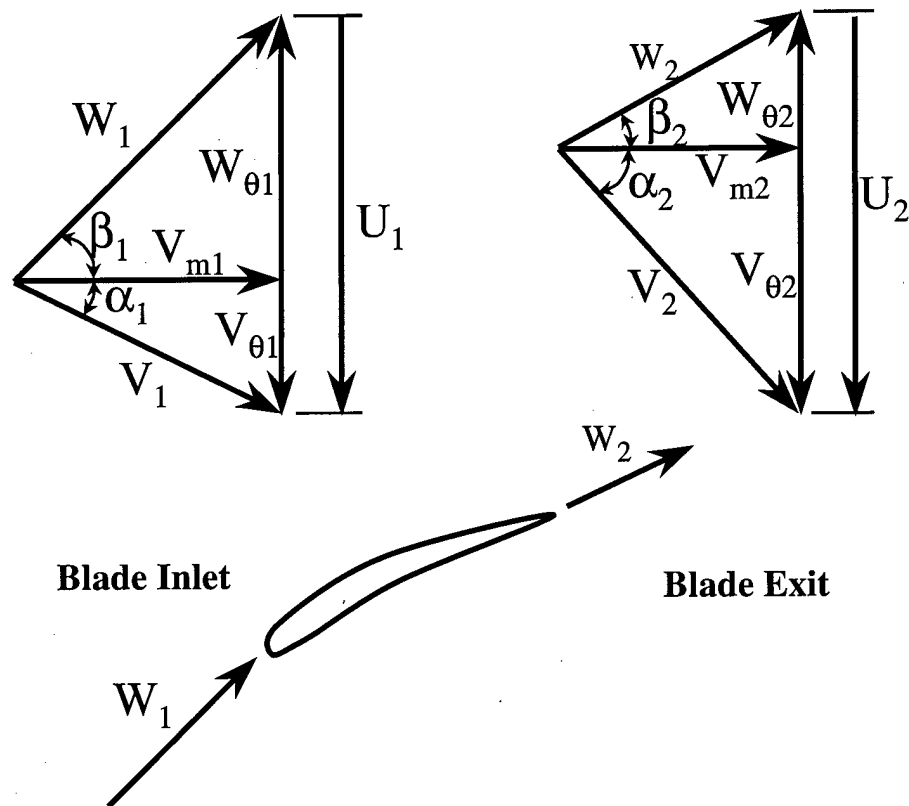
Figure 3.3. Velocity Triangle Nomenclature Used in SLCC.
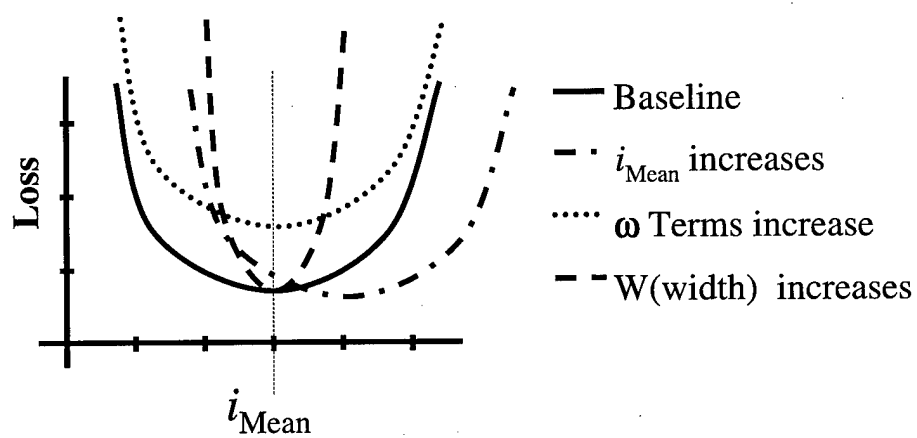
Figure 3.4. Representative Loss Bucket.
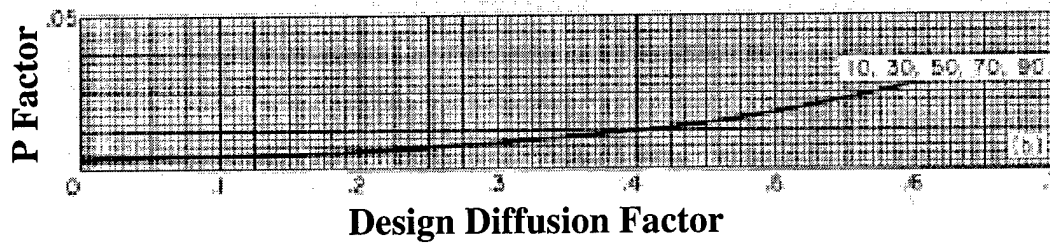
Figure 3.5. P Factor for Minimum Loss Calculation
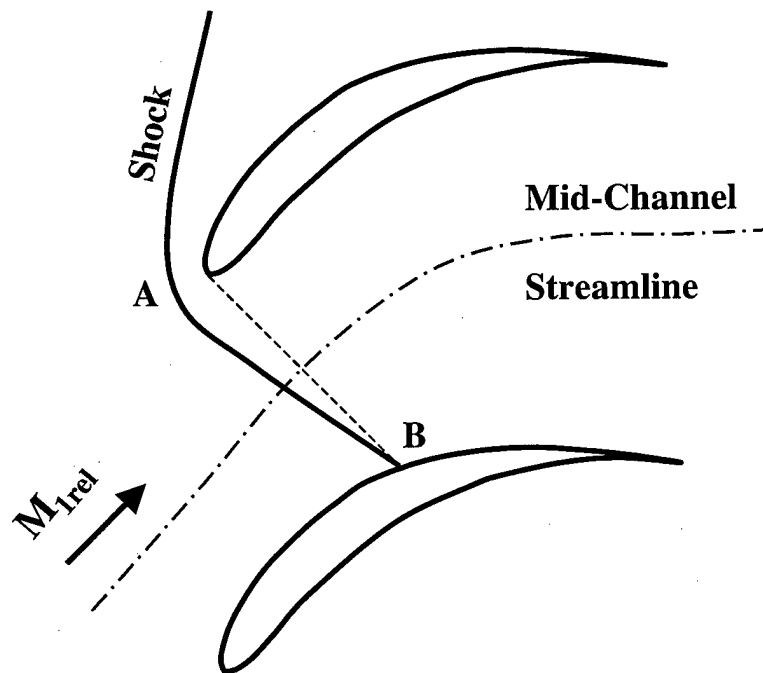
Figure 3.6 Schematic of Lewis, Hartman, Miller Shock Model.
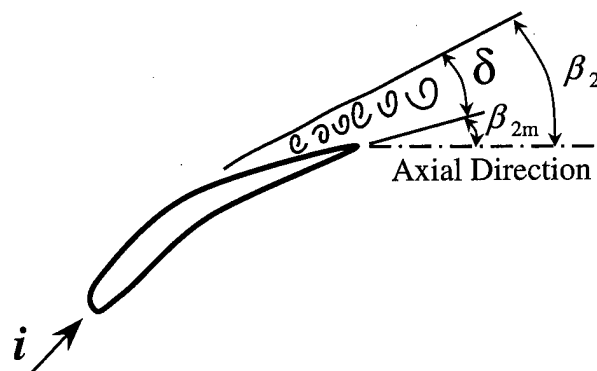
Figure 3.7. Schematic of Deviation.
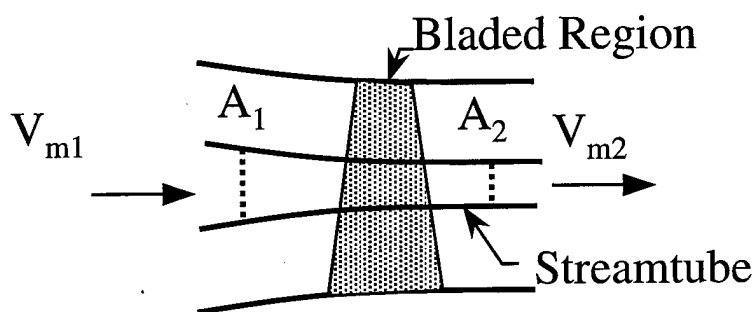
Figure 3.8. Schematic of Streamtube Geometry Change Due
to Axial Velocity Variation.
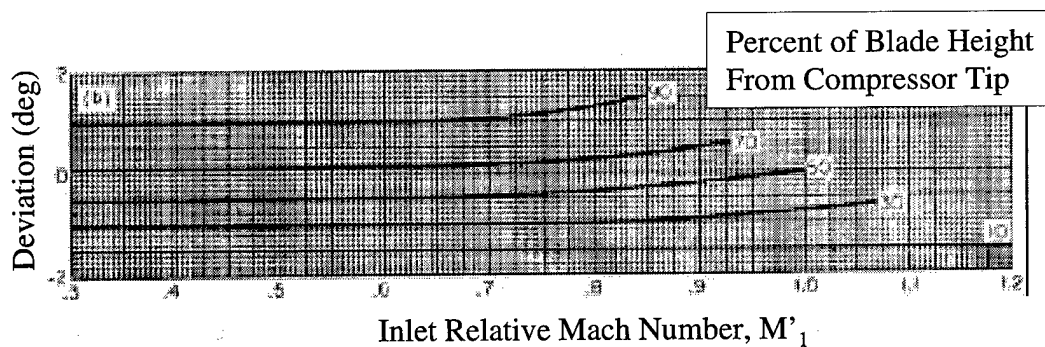
Figure 3.9. Variation of Deviation with Inlet Relative Mach Number for
Different Radial Locations on Double Circular Arc Sections.
(Robbins, Jackson, and Lieblein, 1965)
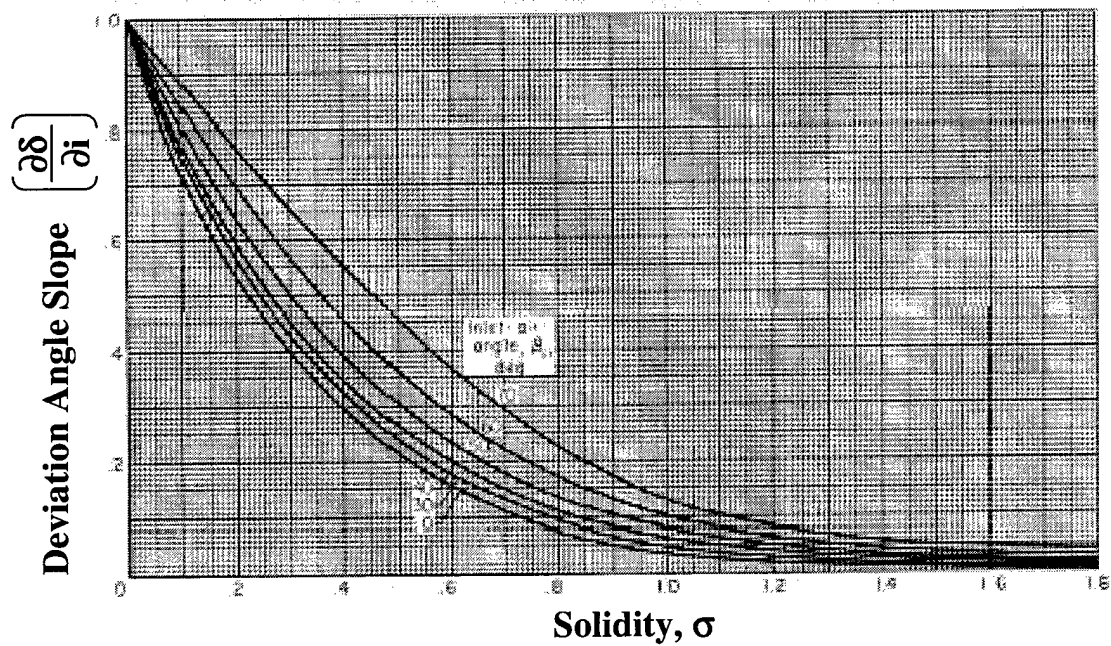
Figure 3.10. Deviation Angle Slope Versus Solidity.
(Robbins, Jackson, and Lieblein, 1965)
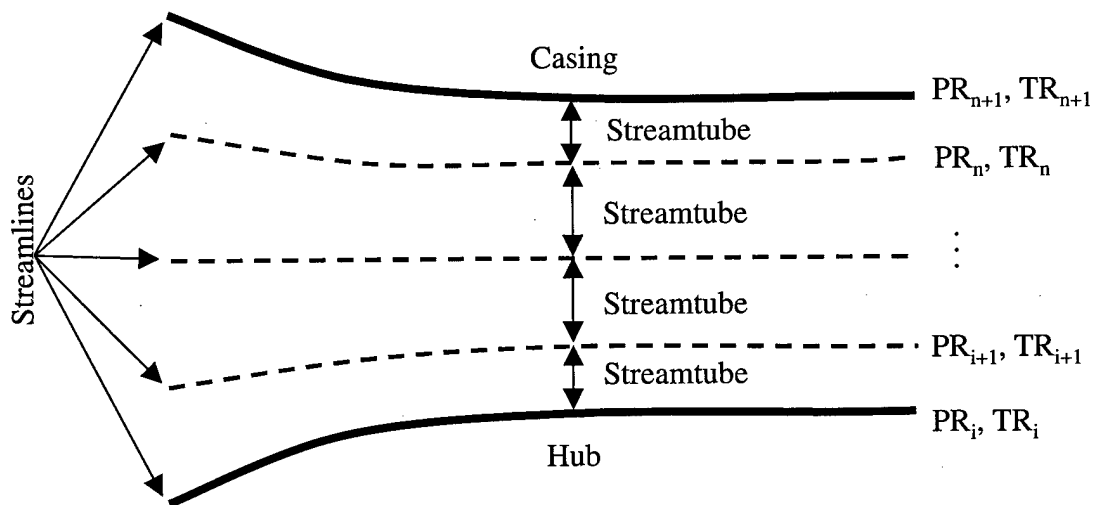
Figure 3.11. Schematic of 1-D Data Reduction Technique
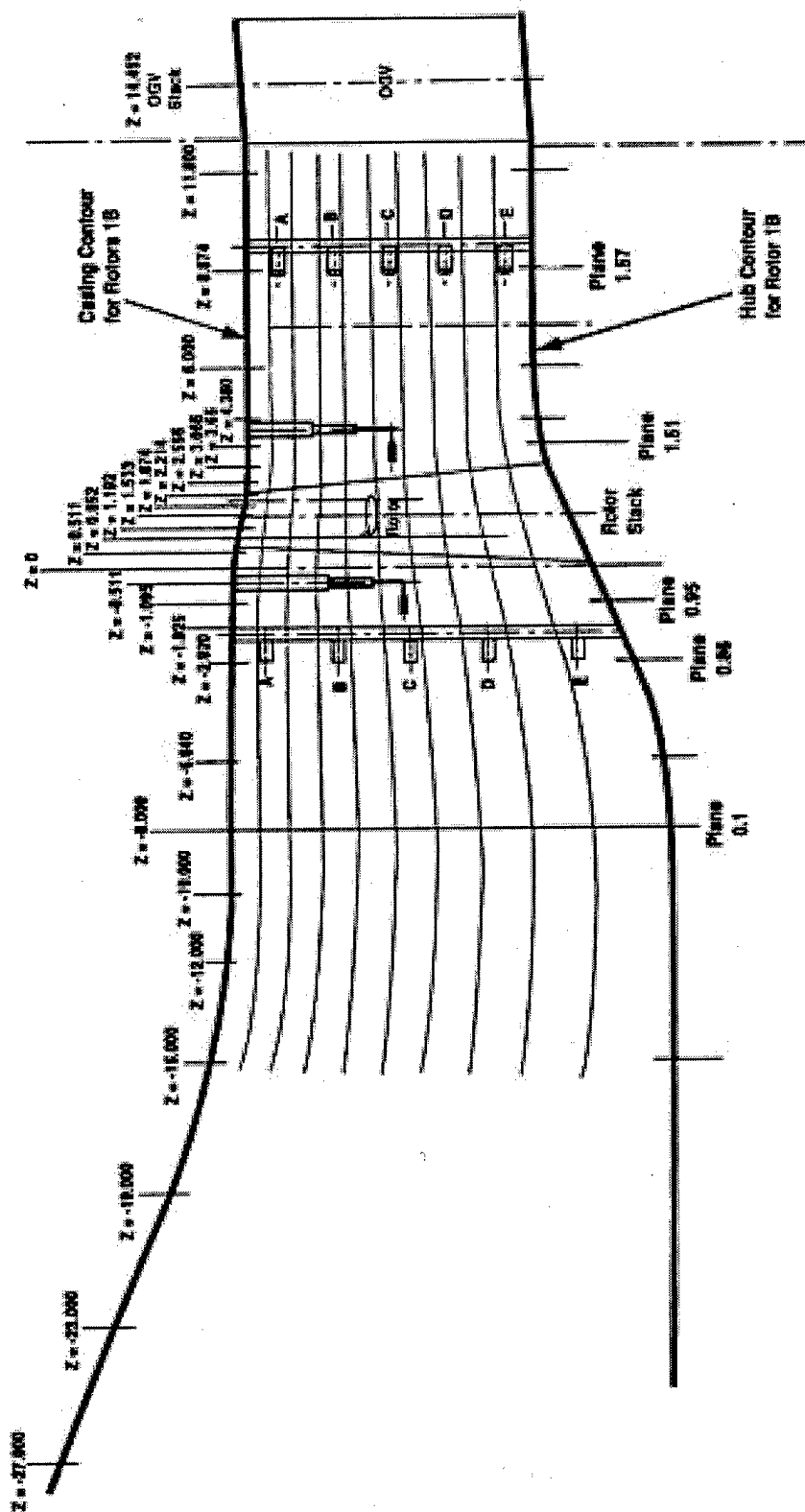
Figure 4.1. Schematic of NASA Rotor 1B Test Setup. (Seyler and Goselow, 1967)
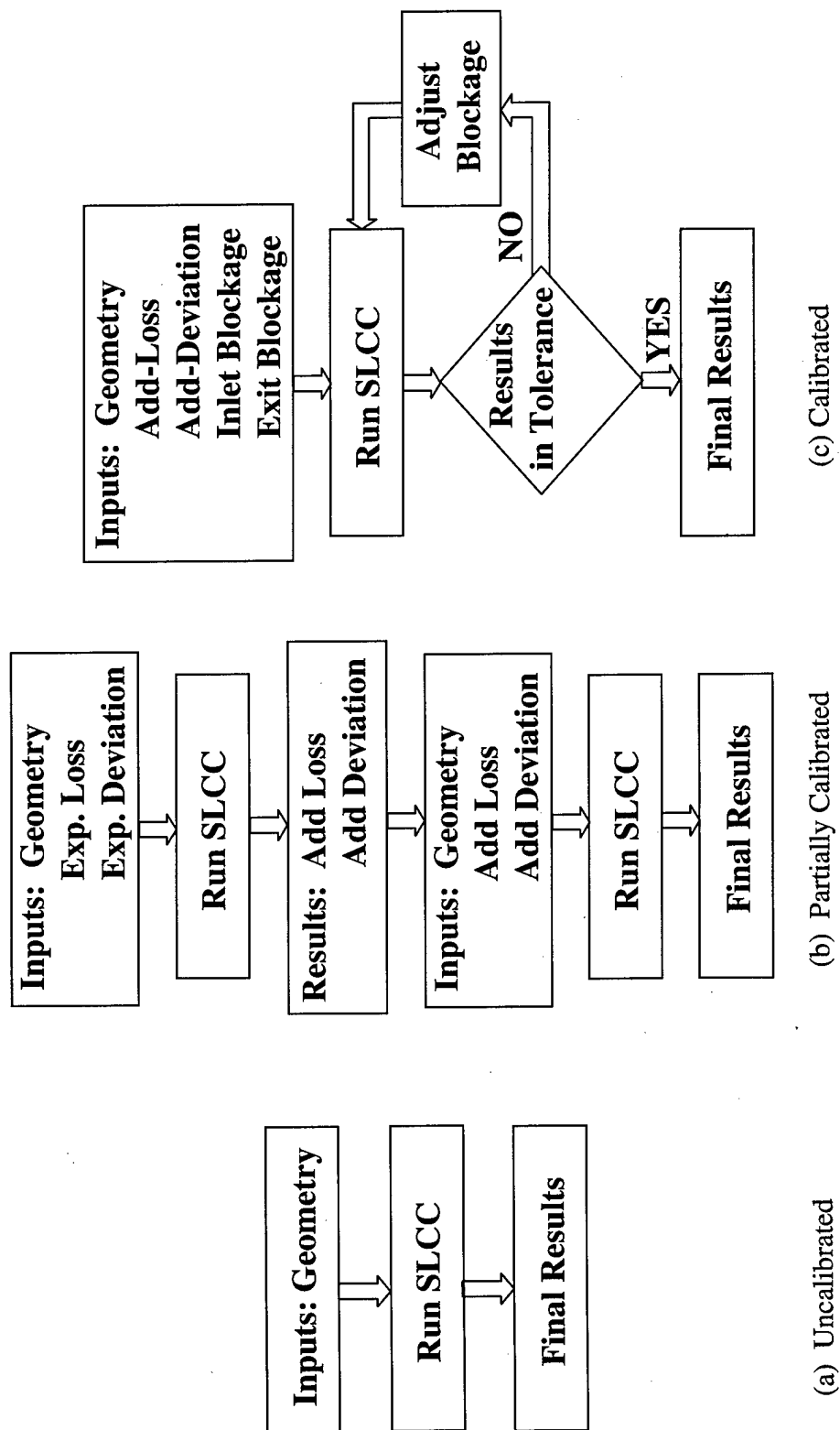
Figure 4.2. Flow Chart for SLCC Calibration Techniques

Inputs: Geometry
Add-Loss
Add-Deviation
Inlet Blockage
Exit Blockage

Run SLCC

Results in Tolerance

Adjust Blockage

NO

YES

Final Results

(c) Calibrated

Inputs: Geometry
Exp. Loss
Exp. Deviation

Run SLCC

Results: Add Loss
Add Deviation

Inputs: Geometry
Add Loss
Add Deviation

Run SLCC

Final Results

(b) Partially Calibrated

Inputs: Geometry

Run SLCC

Final Results

(a) Uncalibrated

84

Figure 4.3. Radial Distribution of Relative Total Pressure Loss
Coefficient including Experimental Data, Uncalibrated Data, Partially
Calibrated Data and Calibrated Data for Rotor 1B.
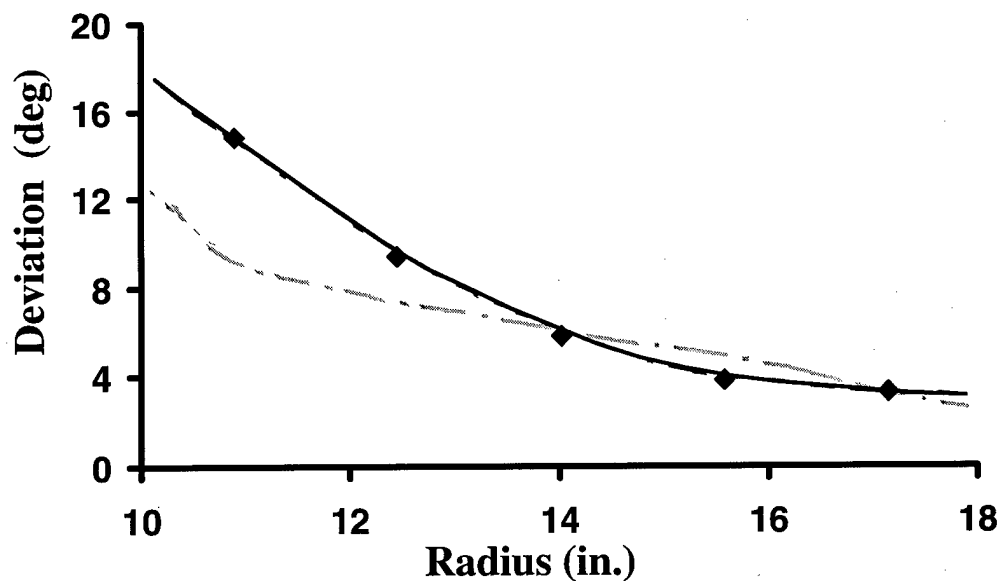
Figure 4.4. Radial Distribution of Deviation including Experimental
Data, Uncalibrated Data, Partially Calibrated Data and Calibrated Data
for Rotor 1B.
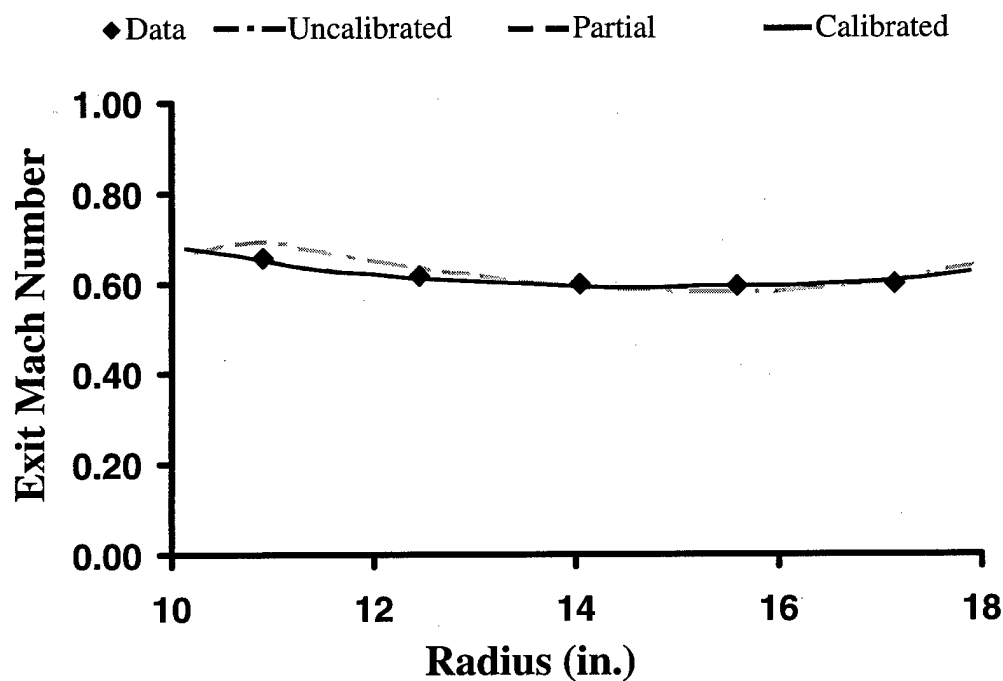
Figure 4.5. Radial Distribution of Exit Mach Number including Experimental Data, Uncalibrated Data, Partially Calibrated Data and Calibrated Data for Rotor 1B.
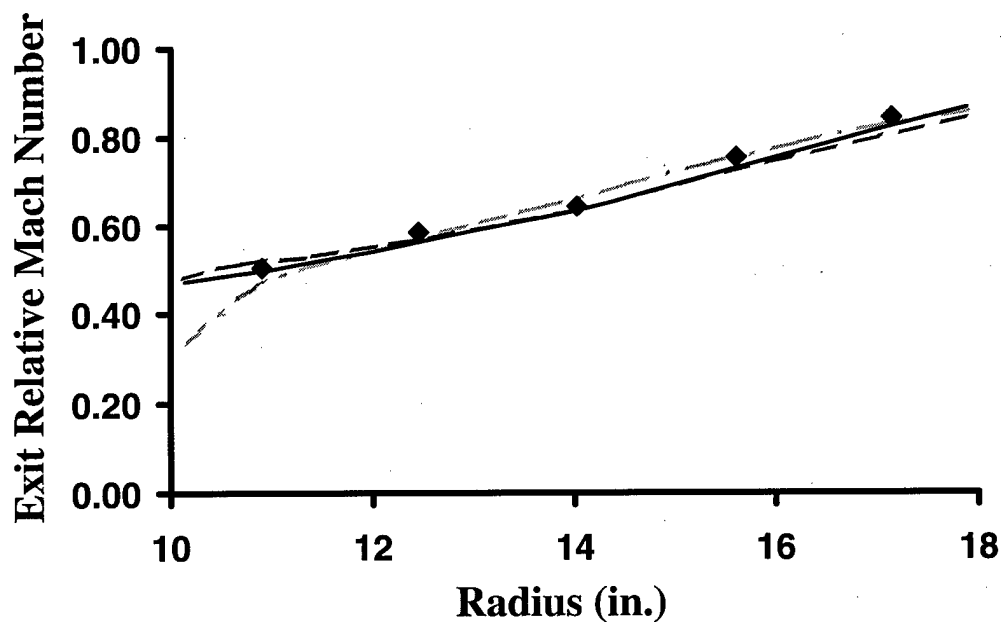
Figure 4.6. Radial Distribution of Exit Relative Mach Number including Experimental Data, Uncalibrated Data, Partially Calibrated Data and Calibrated Data for Rotor 1B.
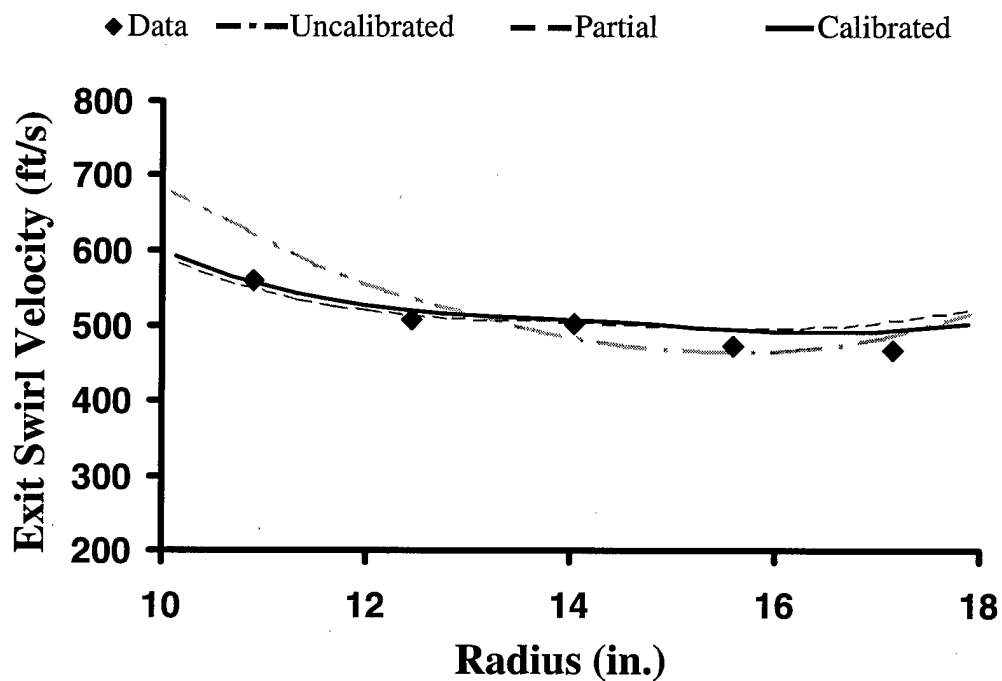
Figure 4.7. Radial Distribution of Exit Swirl Velocity including Experimental Data, Uncalibrated Data, Partially Calibrated Data and Calibrated Data for Rotor 1B.
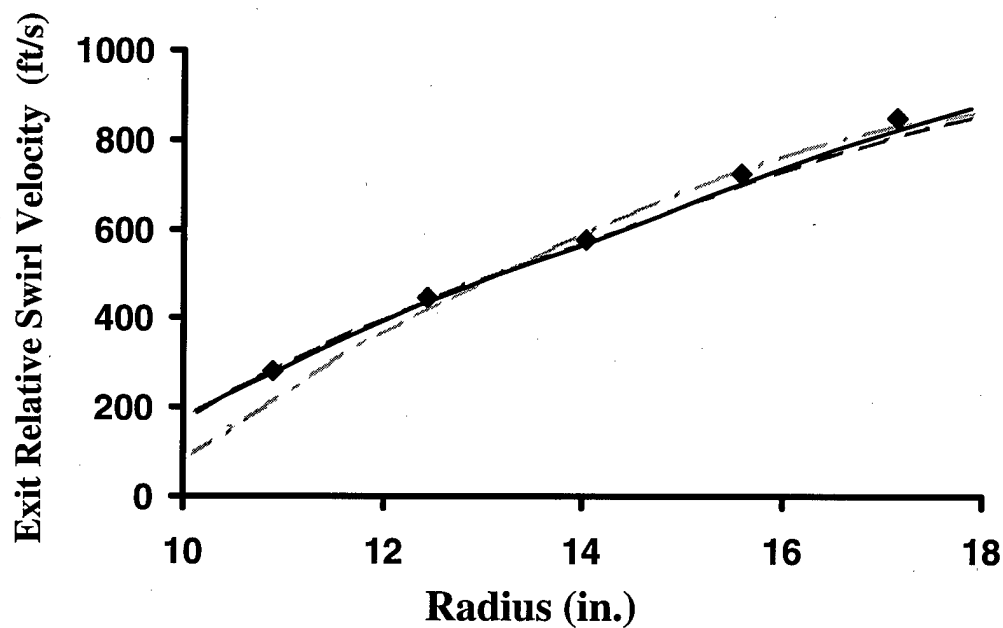
Figure 4.8. Radial Distribution of Exit Relative Swirl Velocity including Experimental Data, Uncalibrated Data, Partially Calibrated Data and Calibrated Data for Rotor 1B.
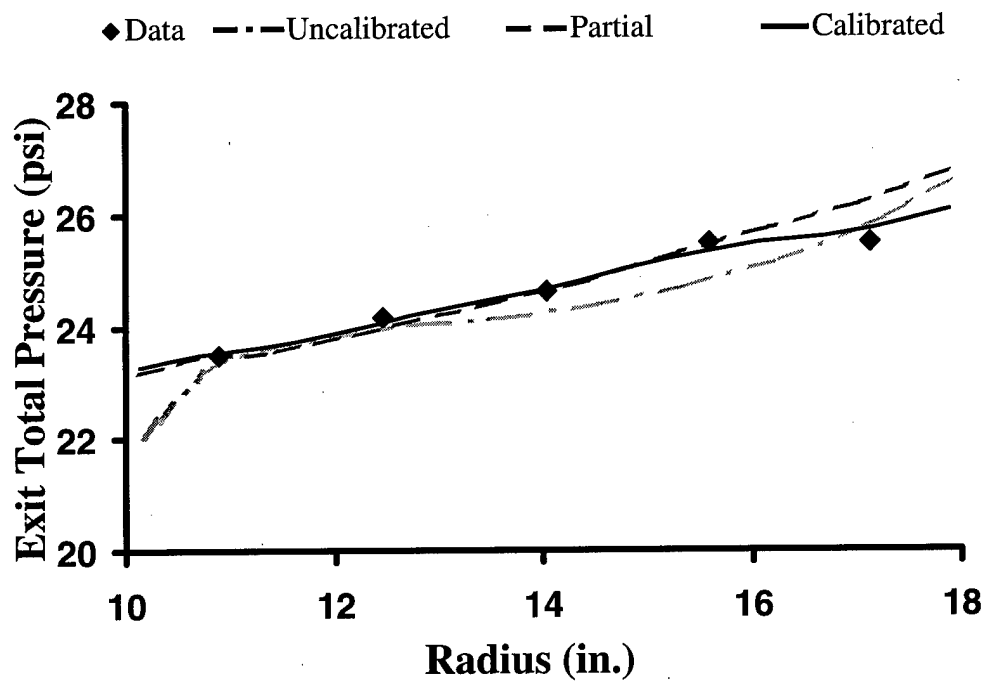
Figure 4.9. Radial Distribution of Exit Total Pressure including Experimental Data, Uncalibrated Data, Partially Calibrated Data and Calibrated Data for Rotor 1B.
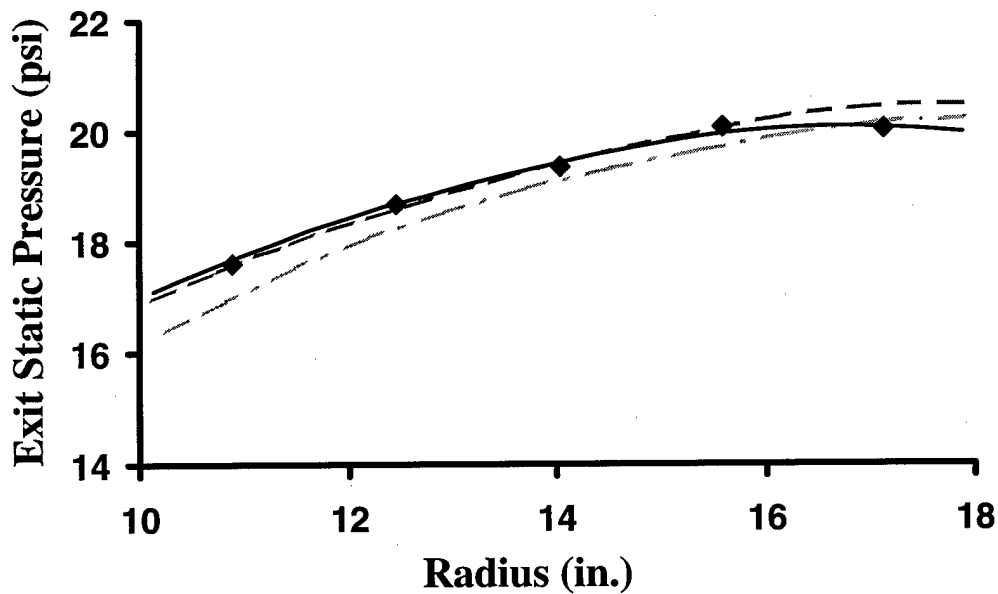
Figure 4.10. Radial Distribution of Exit Static Pressure including Experimental Data, Uncalibrated Data, Partially Calibrated Data and Calibrated Data for Rotor 1B.
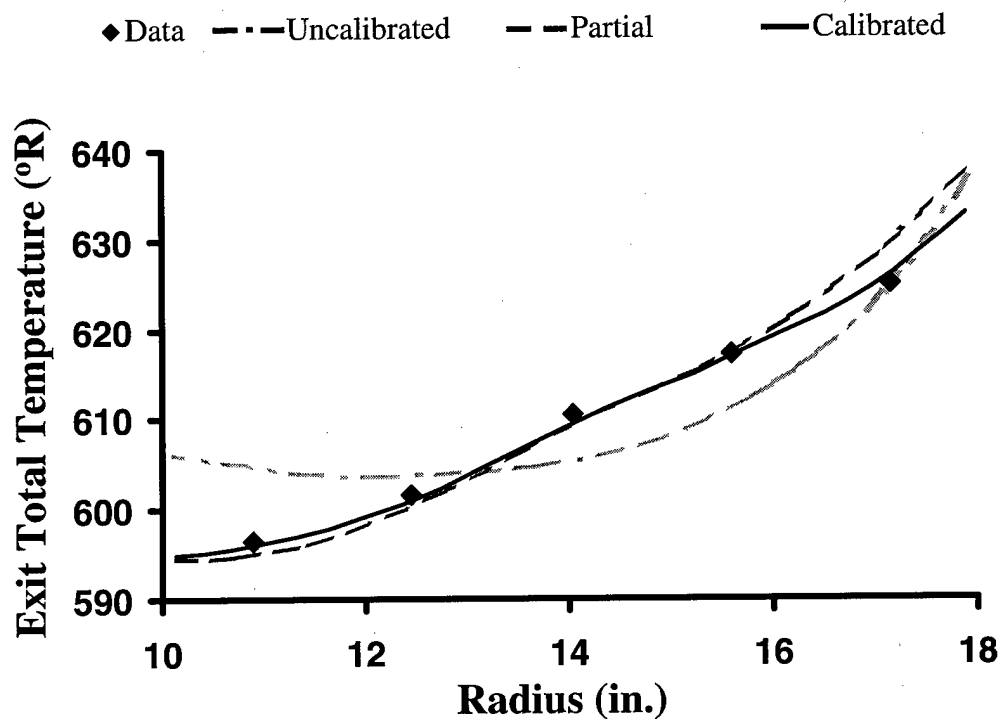
Figure 4.11. Radial Distribution of Exit Total Temperature including
Experimental Data, Uncalibrated Data, Partially Calibrated Data and
Calibrated Data for Rotor 1B.
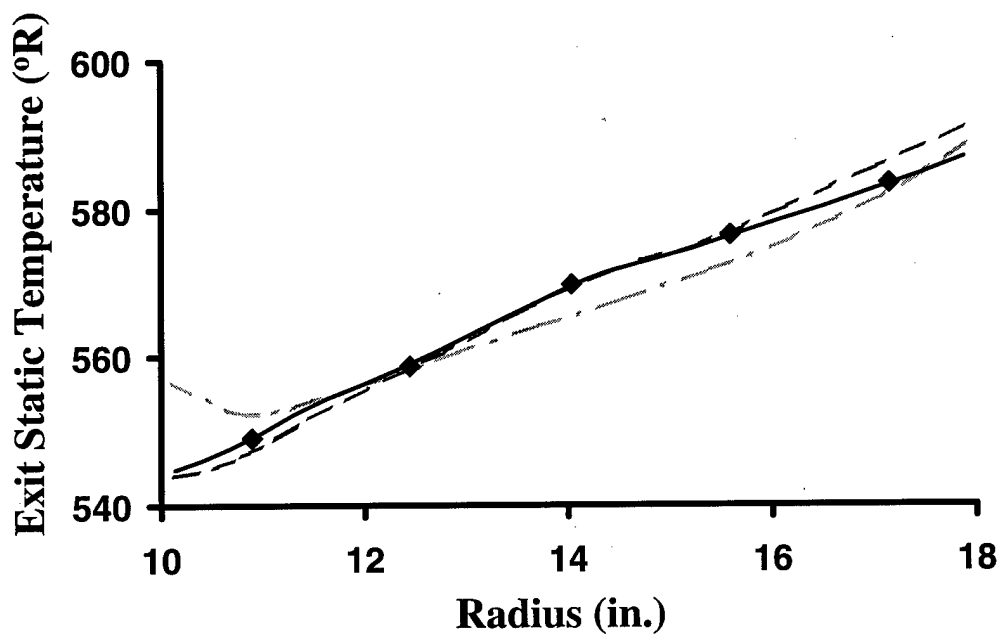
Figure 4.12. Radial Distribution of Exit Static Temperature including
Experimental Data, Uncalibrated Data, Partially Calibrated Data and
Calibrated Data for Rotor 1B.
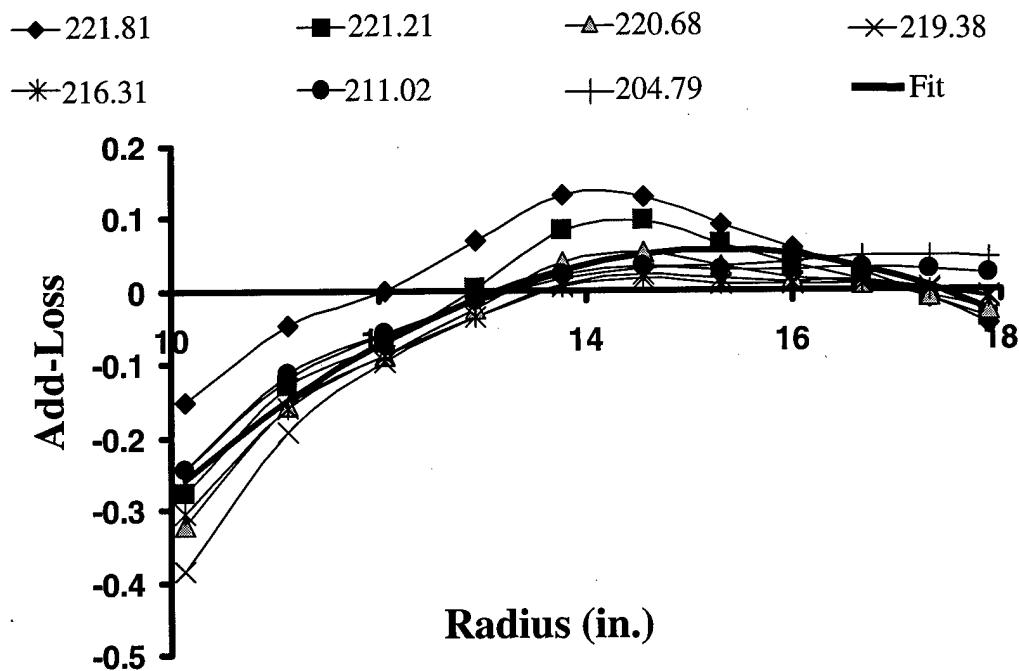
Figure 4.13. Radial Distribution of Add-Loss at 100-Percent Speed
for Various Mass Flows for Rotor1B.
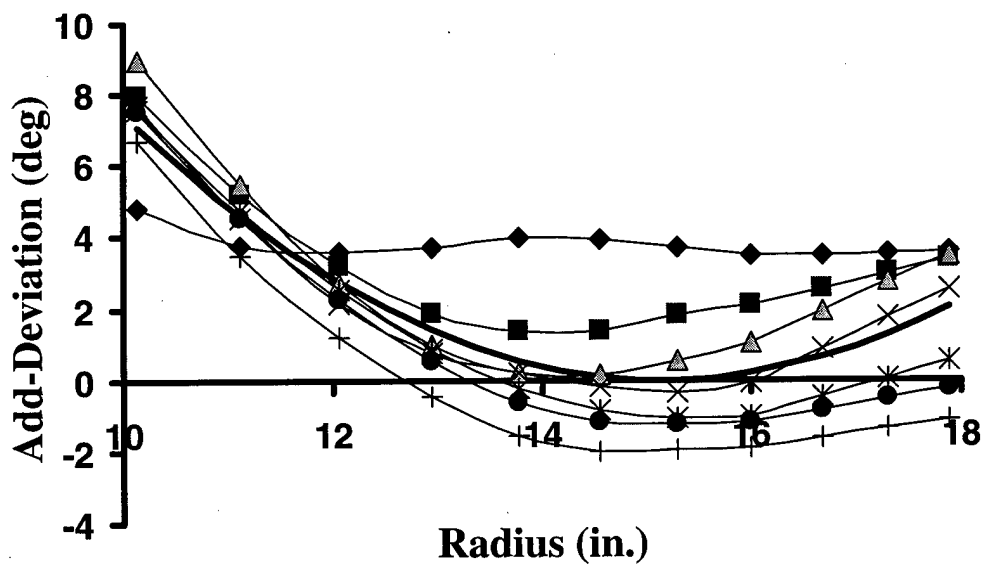
Figure 4.14. Radial Distribution of Add-Deviation at 100-Percent Speed
for Various Mass Flows for Rotor1B.
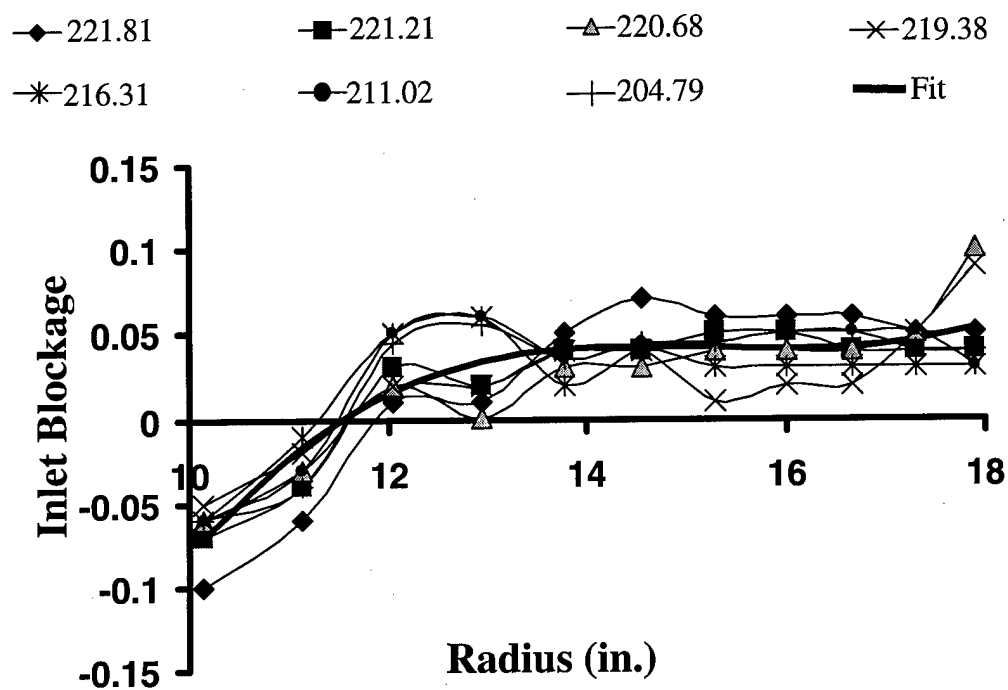
Figure 4.15. Radial Distribution of Inlet Blockage at 100-Percent Speed for Various Mass Flows for Rotor1B.
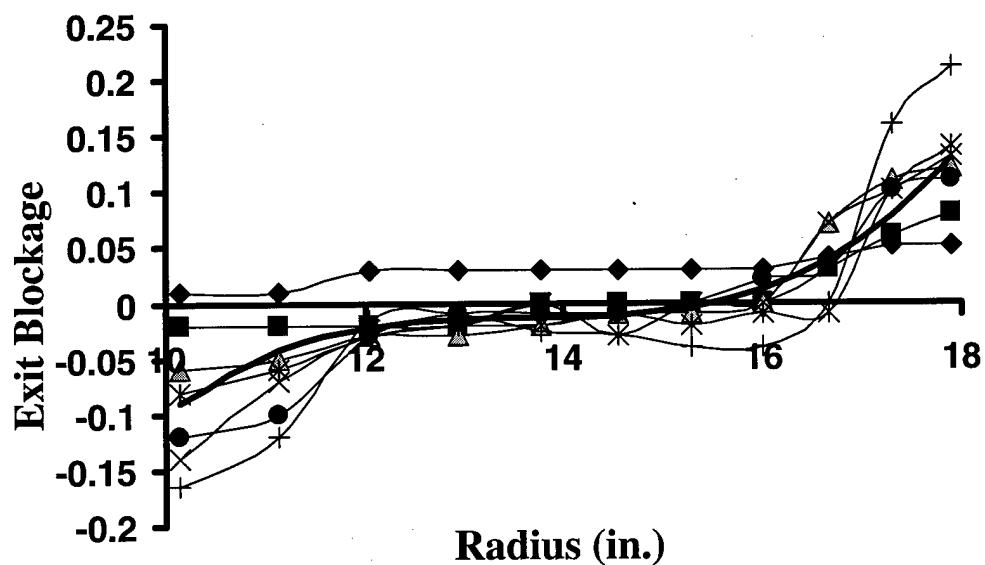
Figure 4.16. Radial Distribution of Exit Blockage at 100-Percent Speed for Various Mass Flows for Rotor1B.
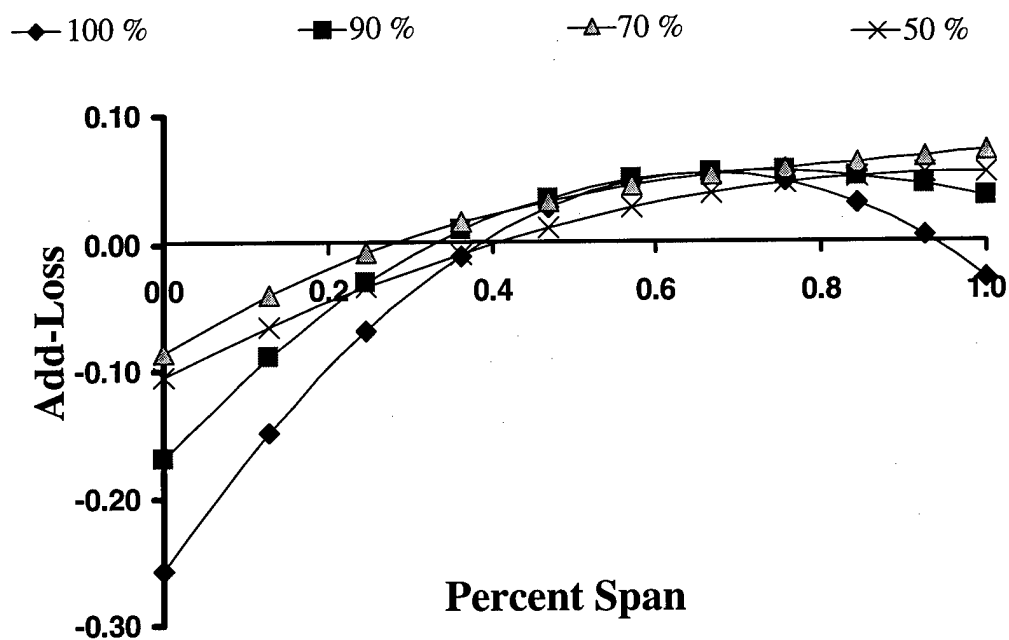
Figure 4.17. Distribution of Add-Loss Averaged Over Mass for Rotor 1B
as a Function of Percent Span for 100-, 90-, 70-, and 50-Percent Speed.
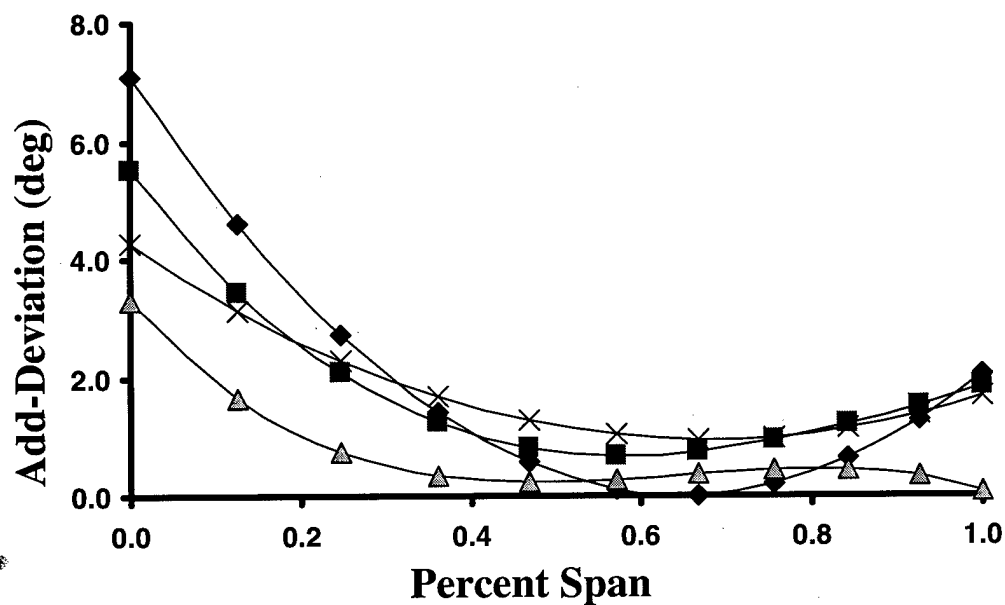
Figure 4.18. Distribution of Add-Deviation Averaged Over Mass for Rotor 1B
as a Function of Percent Span for 100-, 90-, 70-, and 50-Percent Speed.
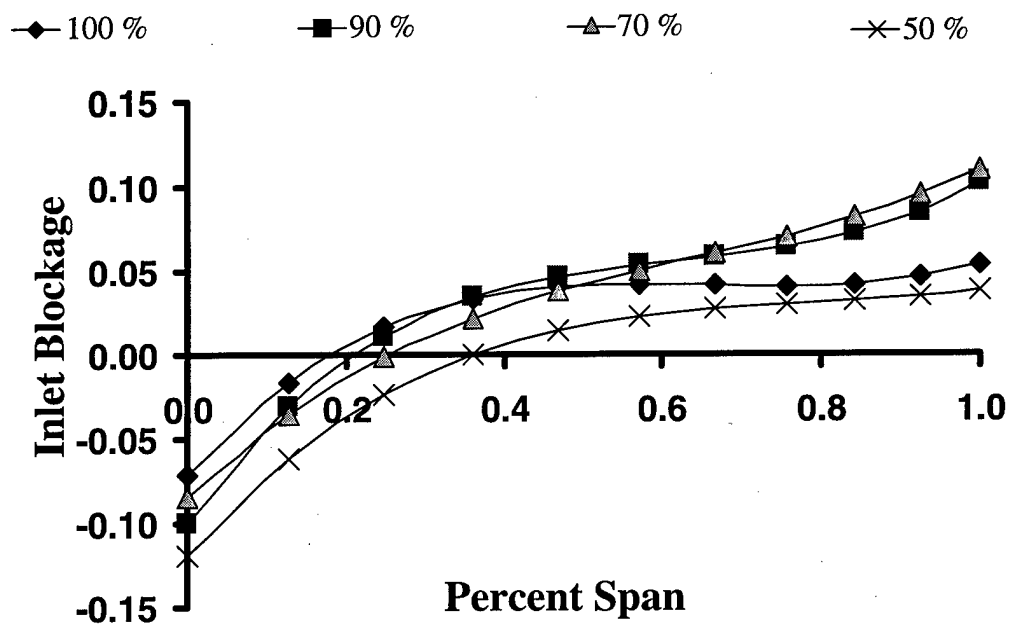
Figure 4.19. Distribution of Inlet Blockage Averaged Over Mass for Rotor 1B
as a Function of Percent Span for 100-, 90-, 70-, and 50-Percent Speed.
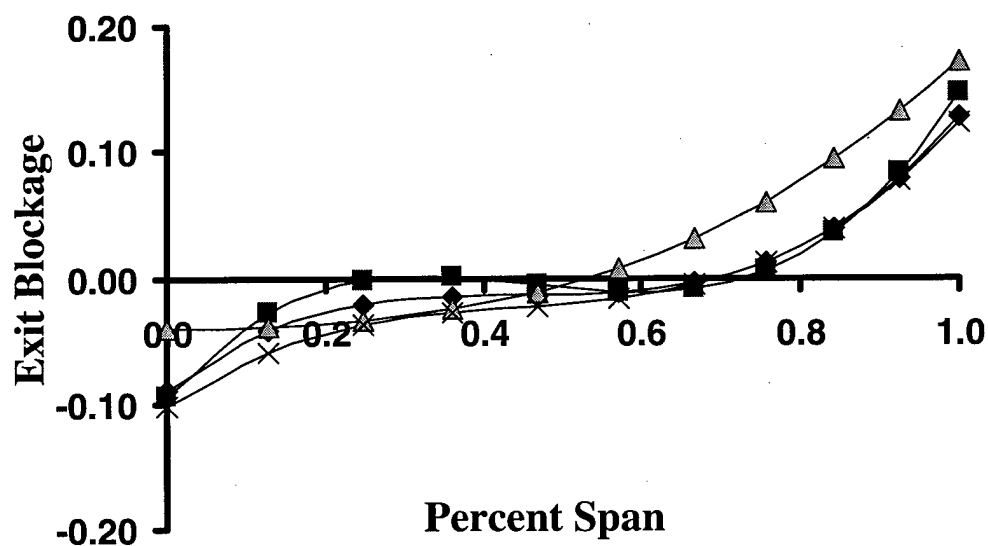
Figure 4.20. Distribution of Exit Blockage Averaged Over Mass for Rotor 1B
as a Function of Percent Span for 100-, 90-, 70-, and 50-Percent Speed.

93
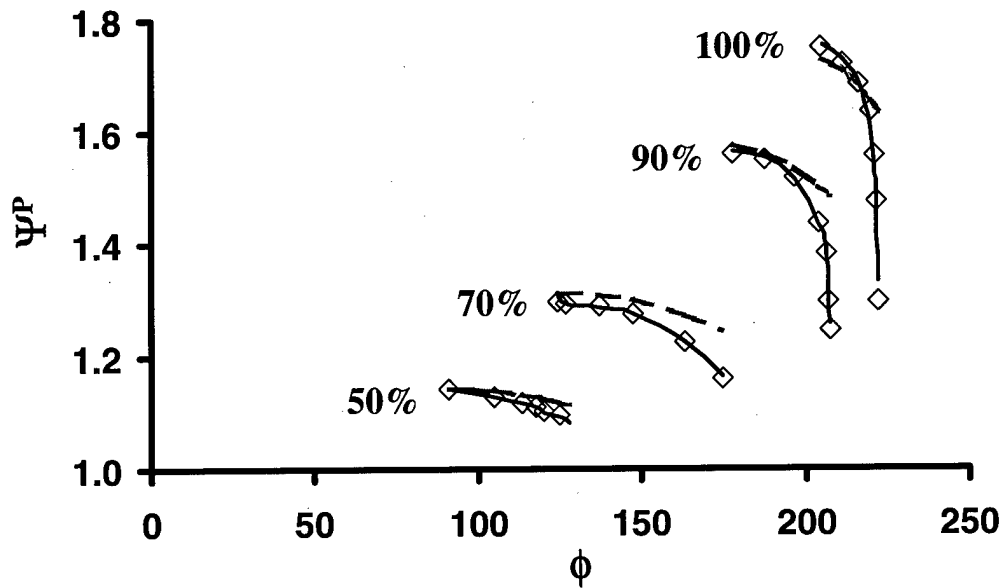
Figure 4.21. 1-D Pressure Characteristic Map for Rotor 1B.

◇ Experimental Data   − − Uncalibrated Results

— Calibrated Results
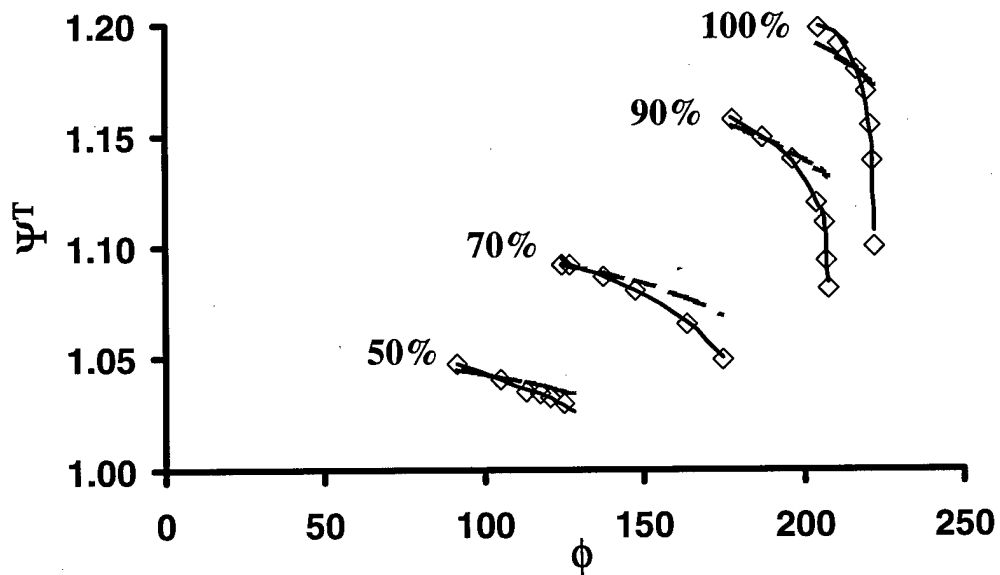
Figure 4.22. 1-D Temperature Characteristic Map for Rotor 1B.
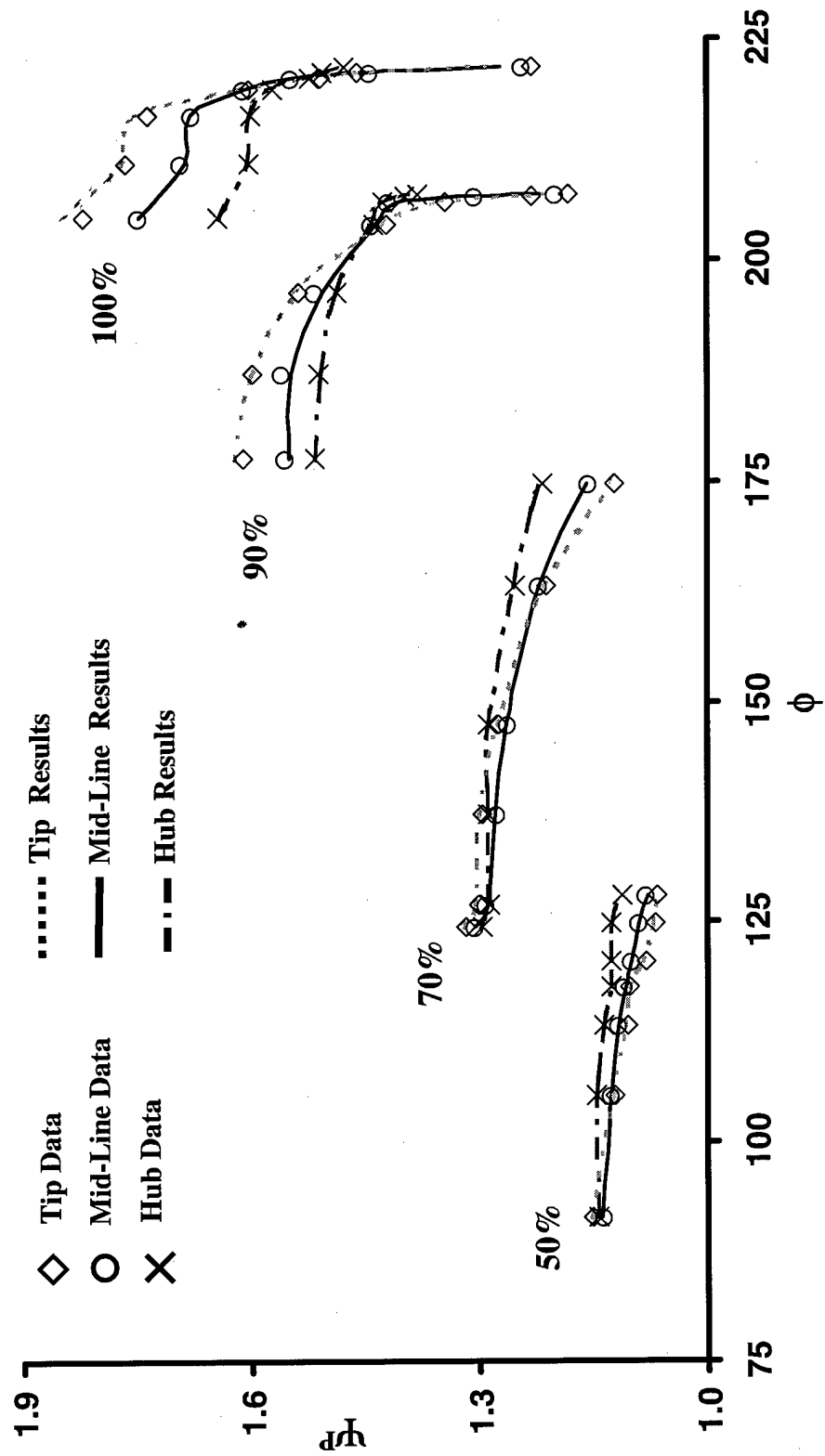
Figure 4.23. Predicted and Experimental 2-D Pressure Characteristic Map for Rotor 1B
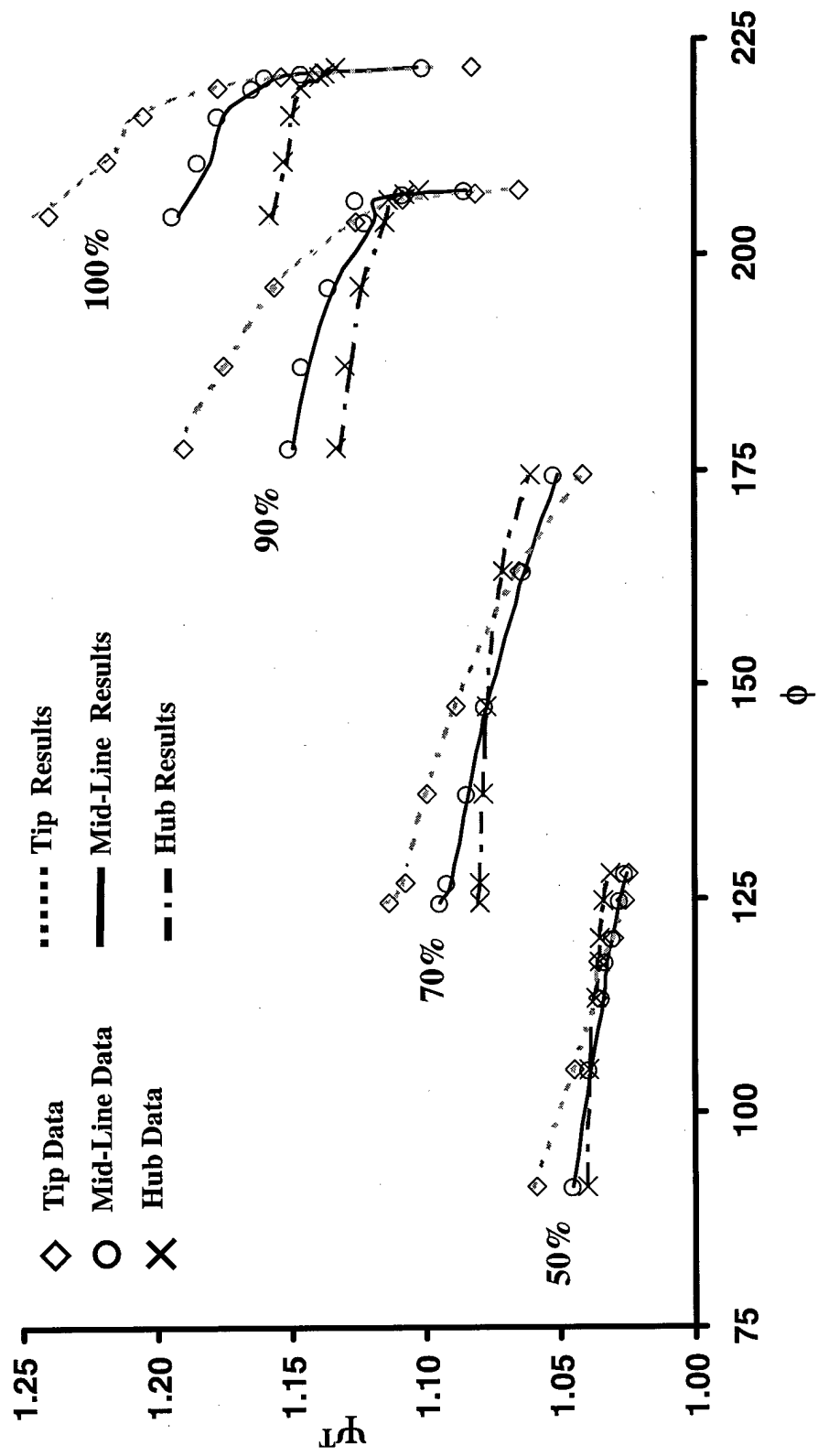
Figure 4.24. Predicted and Experimental 2-D Temperature Characteristic Map for Rotor 1B
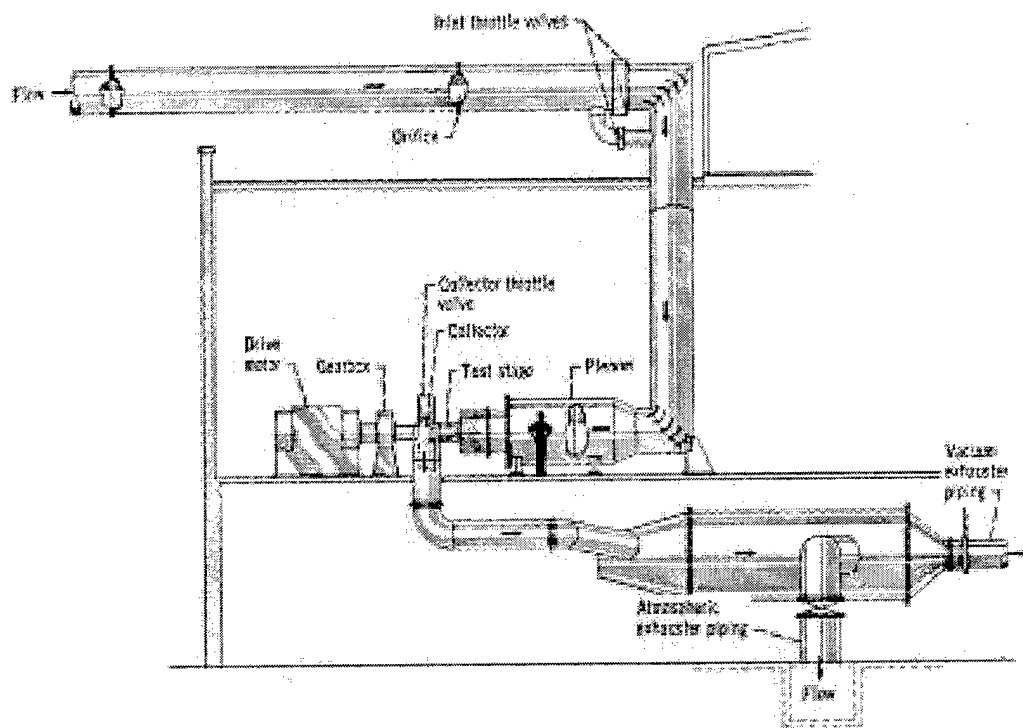
Figure 5.1. Schematic of NASA Stage 35 Test Facility.
(Reid and Moore, 1978)
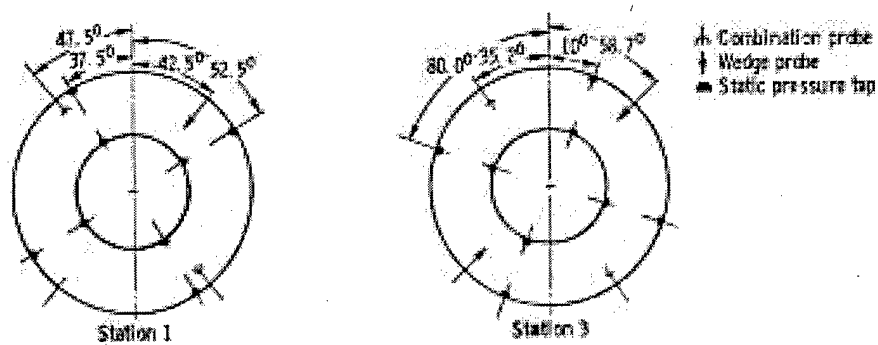
Figure 5.2. Schematic of NASA Stage 35 Instrumentation Layout.
(Reid and Moore, 1978)
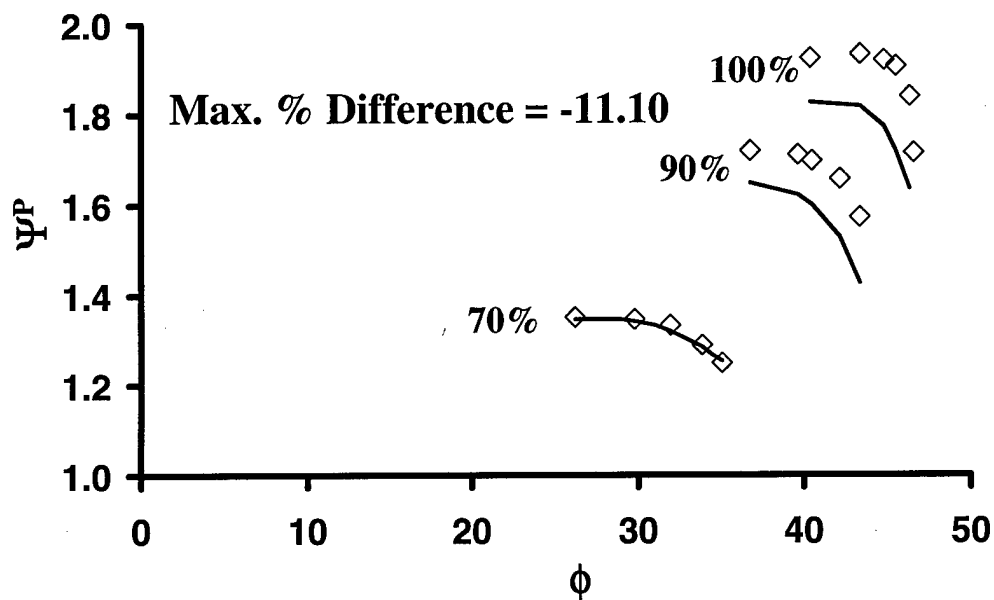
Figure 5.3. 1-D Pressure Characteristic Map for Stage 35
with Rotor 1B Calibration Trends Included.

◇ Data   — Results of Stage 35 with Rotor 1B Calibration Trends
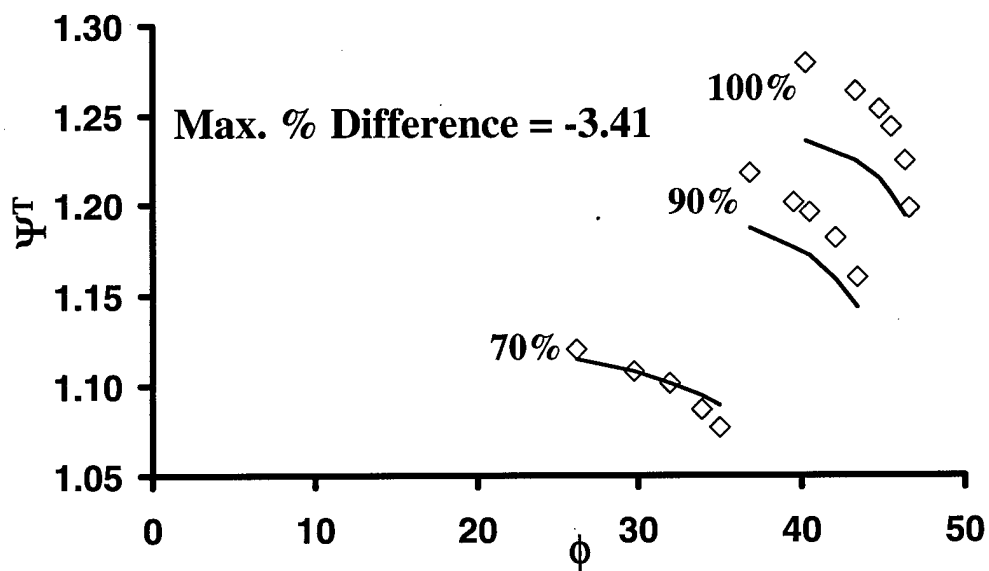
Figure 5. 4. 1-D Temperature Characteristic Map for Stage 35
with Rotor 1B Calibration Trends Included.
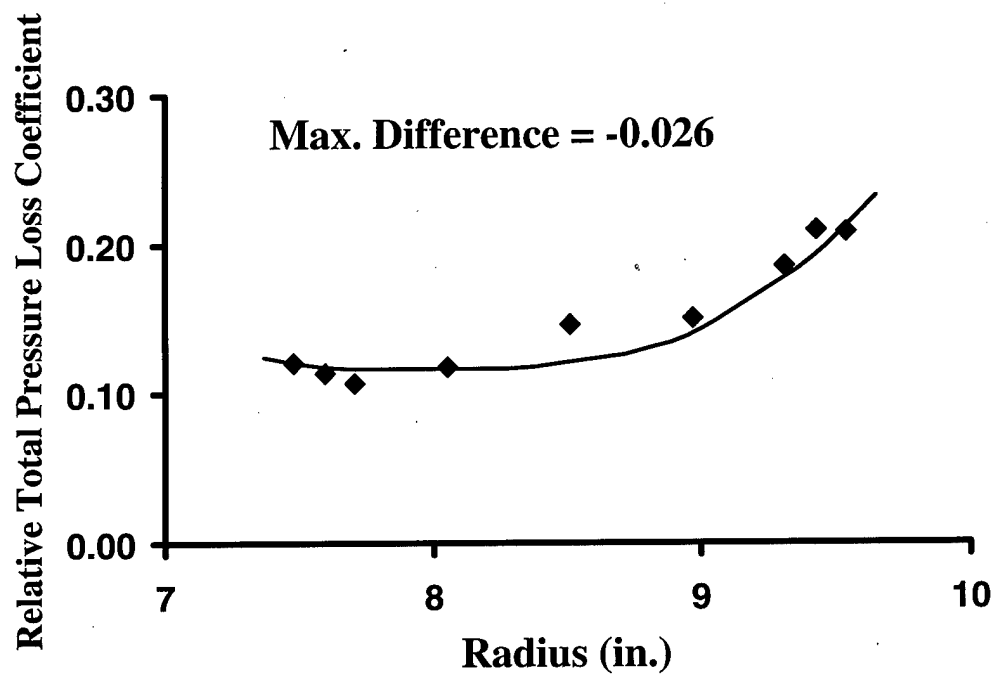
Figure 5.5. Radial Distribution of Relative Total Pressure Loss
Coefficient for Stage 35 Rotor.

◆ Experimental Data   — Uncalibrated SLCC Results
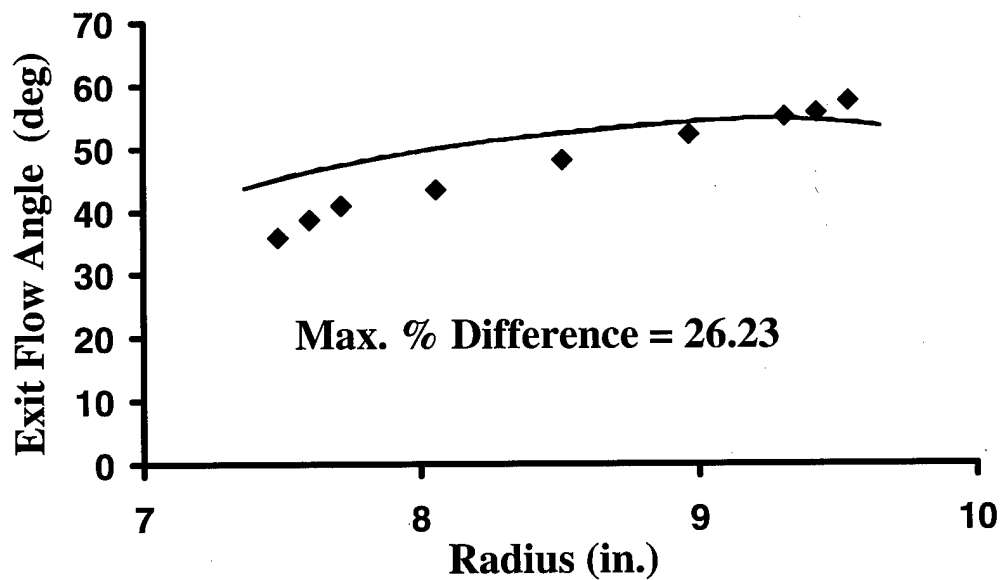
Figure 5.6. Radial Distribution of Exit Flow Angle for Stage 35 Rotor.
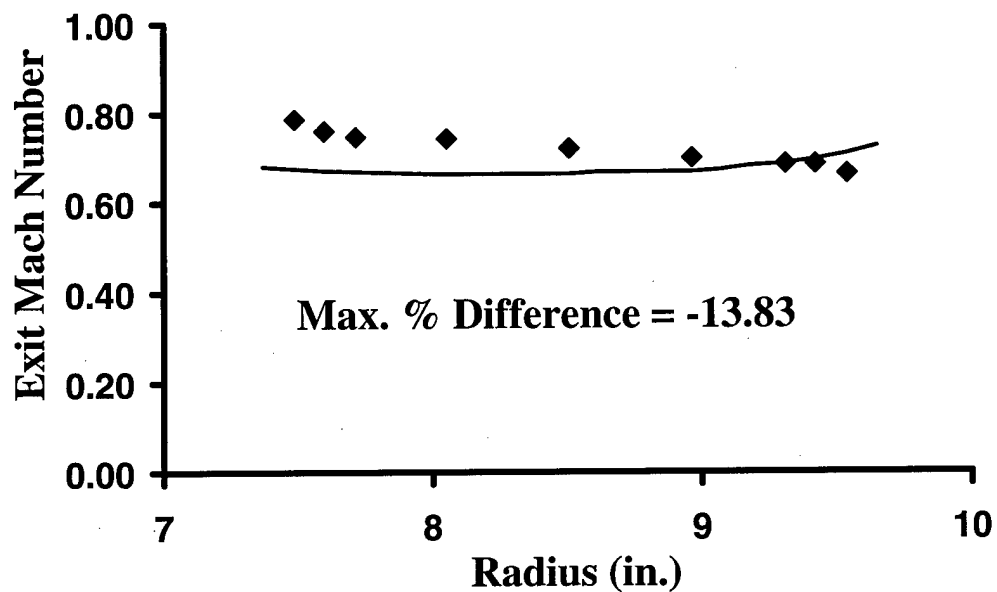
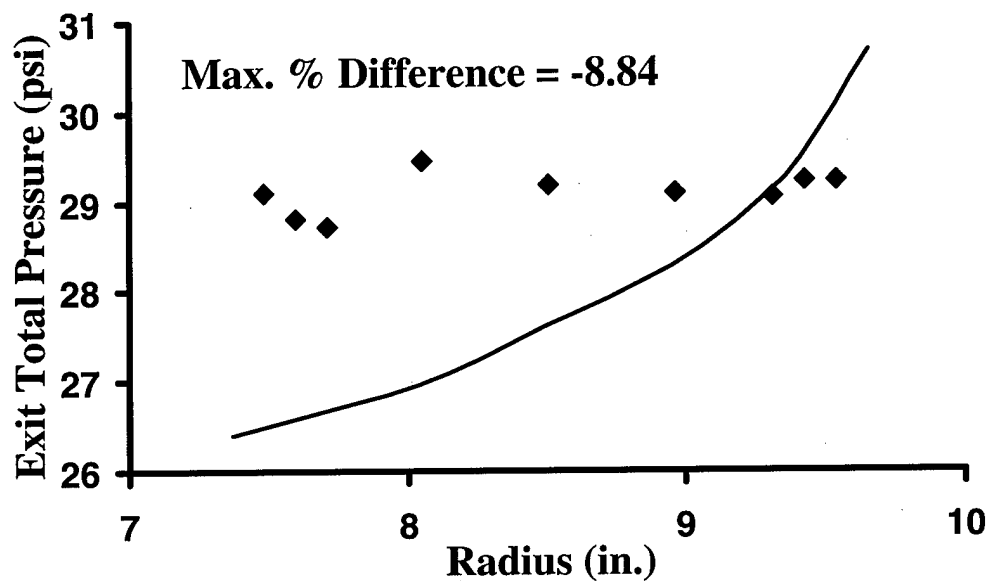Figure 5.7. Radial Distribution of Exit Mach Number for
Stage 35 Rotor.
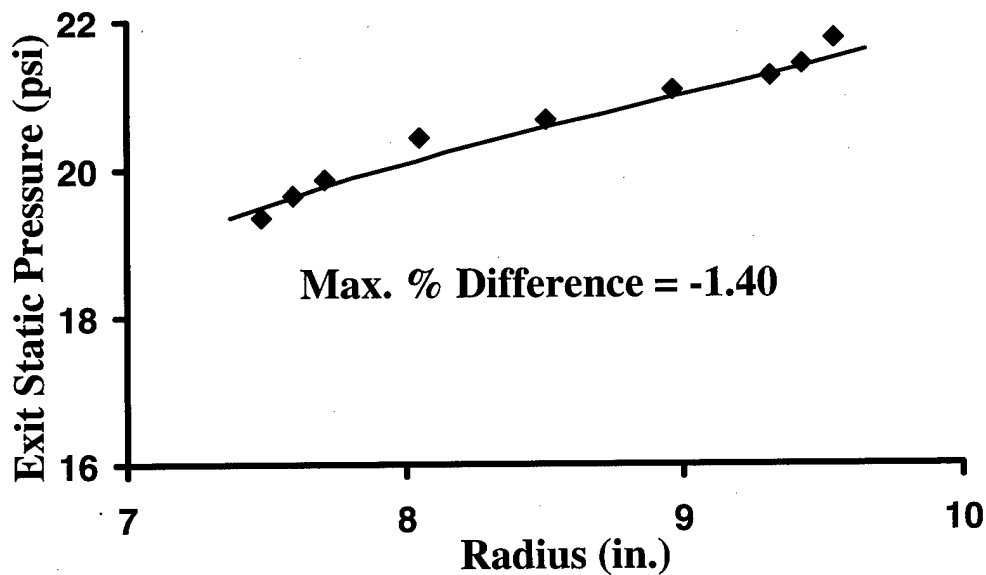
◆ Experimental Data   — Uncalibrated SLCC Results
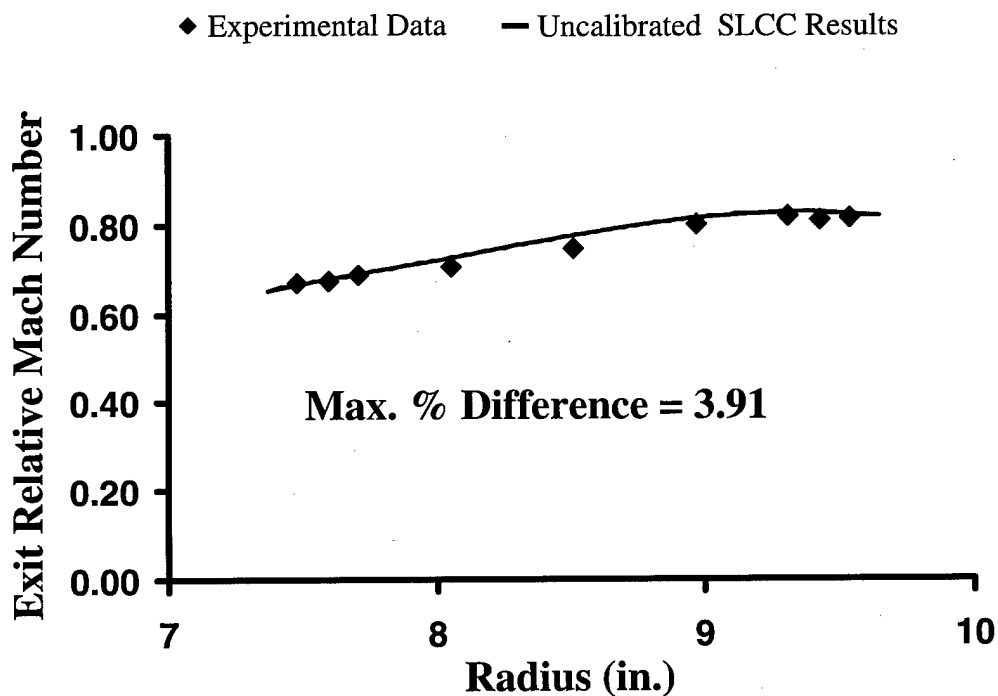
Figure 5.8. Radial Distribution of Exit Relative Mach Number
for Stage 35 Rotor.
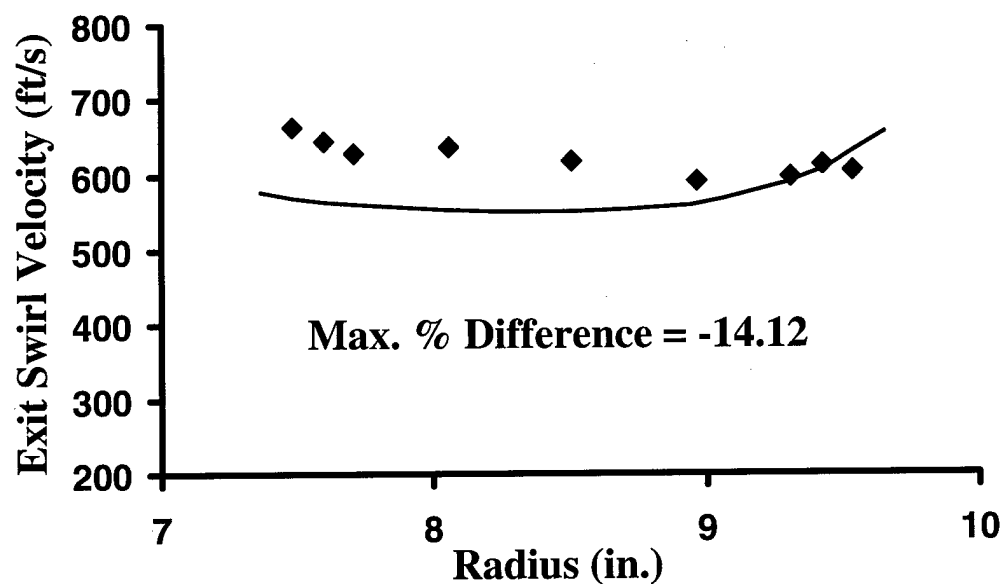
Figure 5.9. Radial Distribution of Exit Swirl Velocity
for Stage 35 Rotor.

◆ Experimental Data   — Uncalibrated SLCC Results
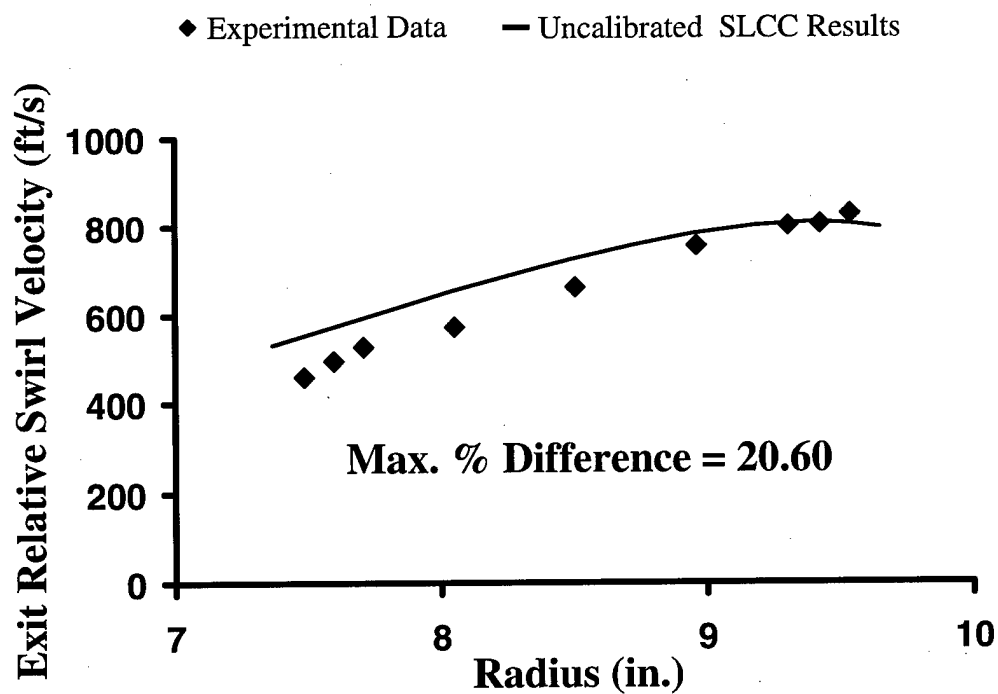
Figure 5.10. Radial Distribution of Exit Relative Swirl Velocity
for Stage 35 Rotor.

101

Figure 5.11. Radial Distribution of Exit Total Pressure
for Stage 35 Rotor.

◆ Experimental Data   — Uncalibrated SLCC Results

Figure 5.12. Radial Distribution of Exit Static Pressure
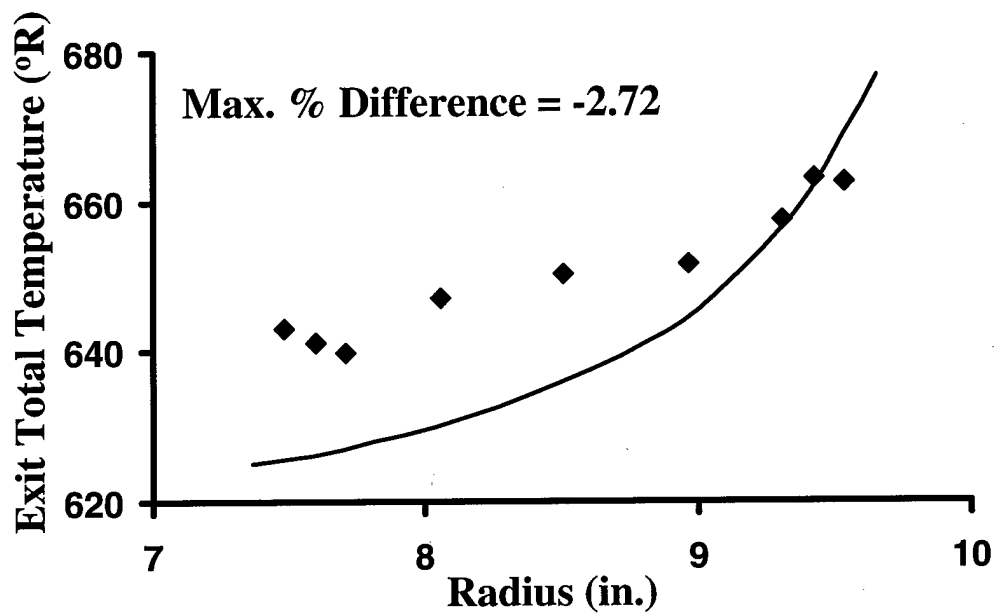for Stage 35 Rotor.

Figure 5.13. Radial Distribution of Exit Total Temperature
for Stage 35 Rotor.

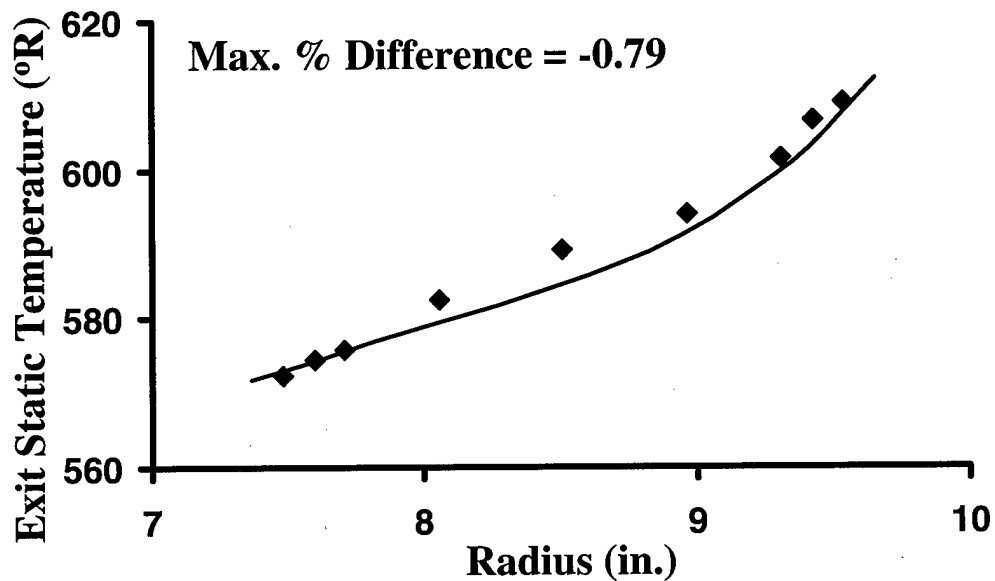◆ Experimental Data   — Uncalibrated SLCC Results

Figure 5.14. Radial Distribution of Exit Static Temperature
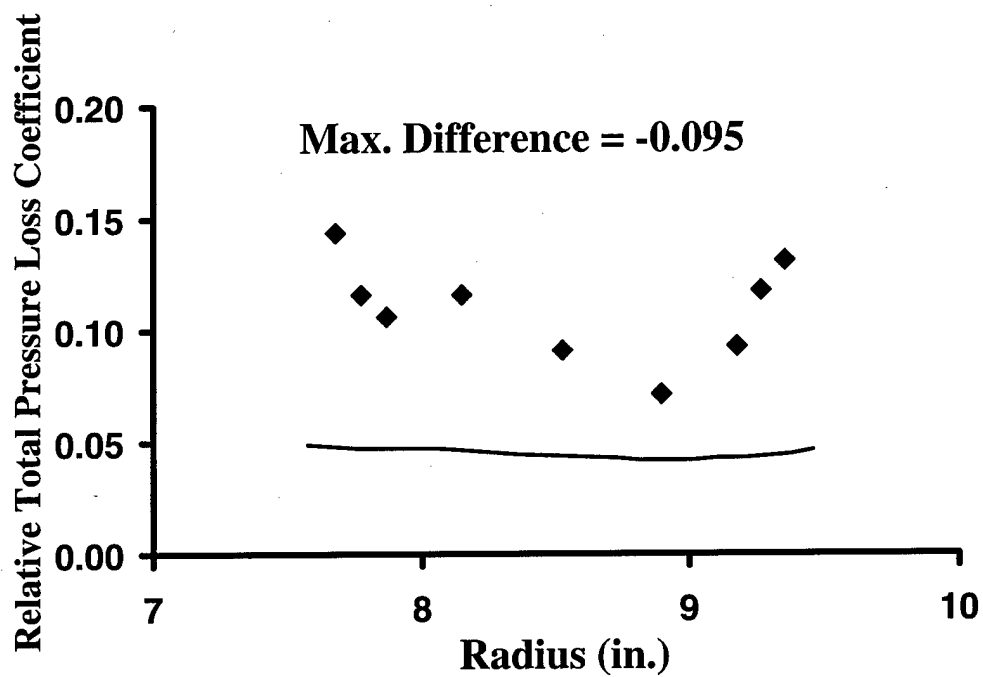for Stage 35 Rotor.

Figure 5.15. Radial Distribution of Relative Total Pressure Loss
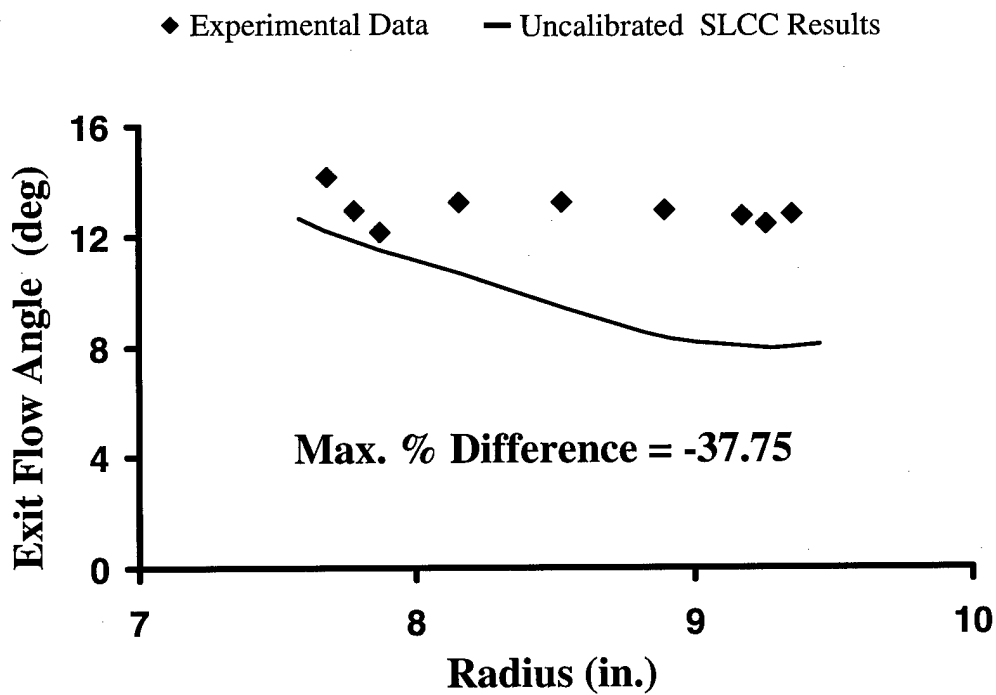Coefficient for Stage 35 Stator.

◆ Experimental Data   — Uncalibrated SLCC Results

Figure 5.16. Radial Distribution of Exit Flow Angle for Stage 35 Stator.
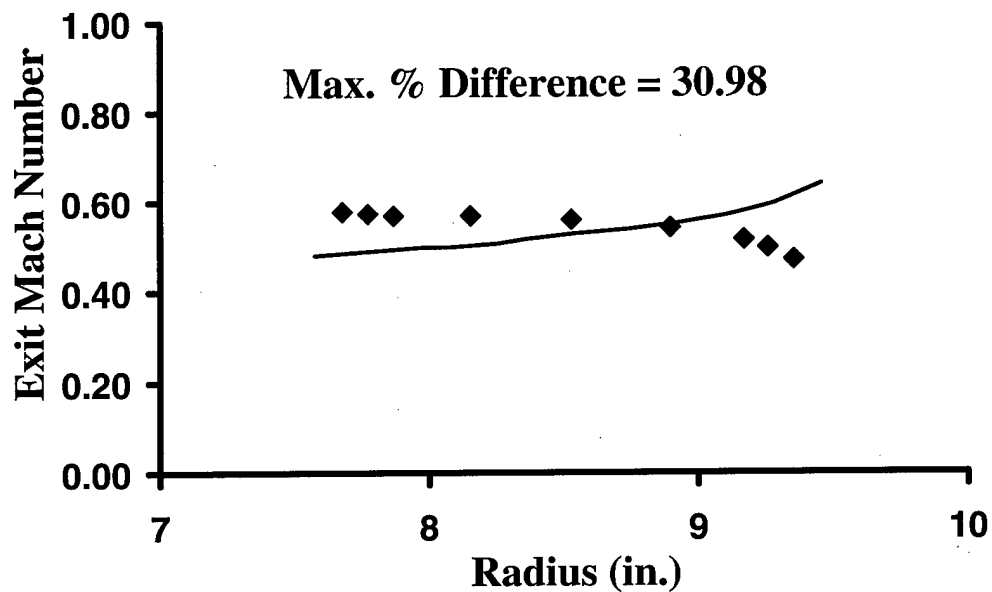
104

Figure 5.17. Radial Distribution of Exit Mach Number for
Stage 35 Stator.

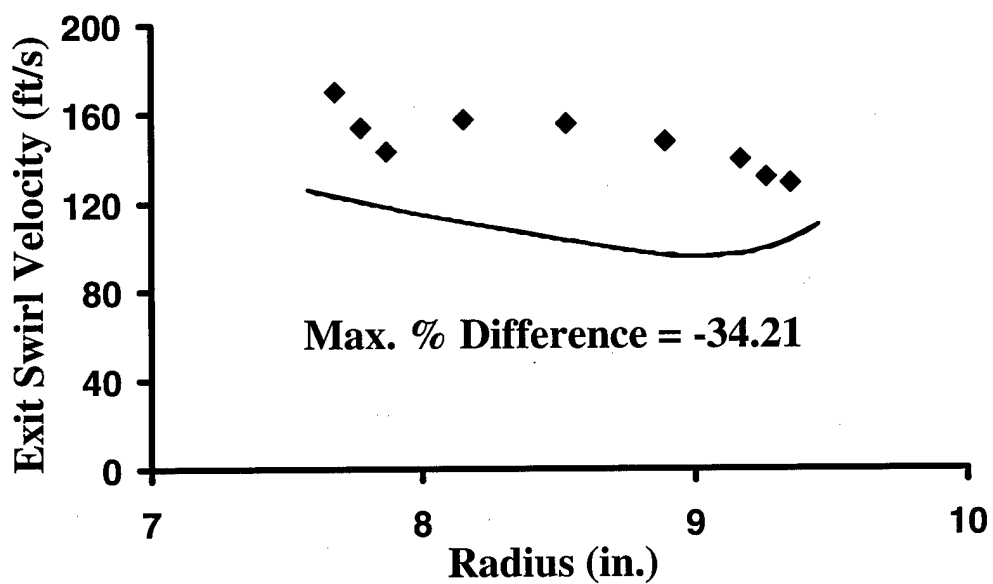◆ Experimental Data   — Uncalibrated SLCC Results

Figure 5.18. Radial Distribution of Exit Swirl Velocity
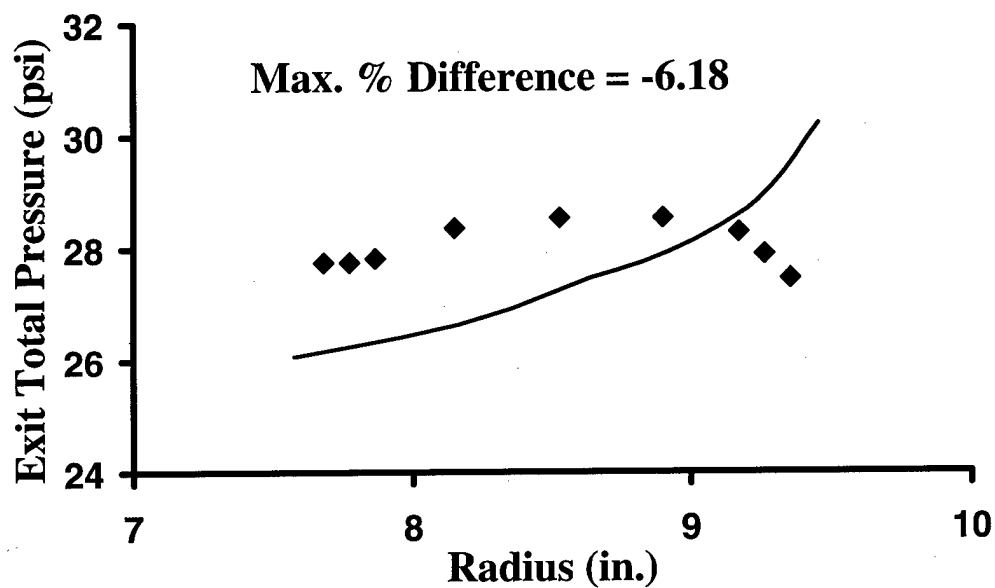for Stage 35 Stator.

Figure 5.19. Radial Distribution of Exit Total Pressure
for Stage 35 Stator.

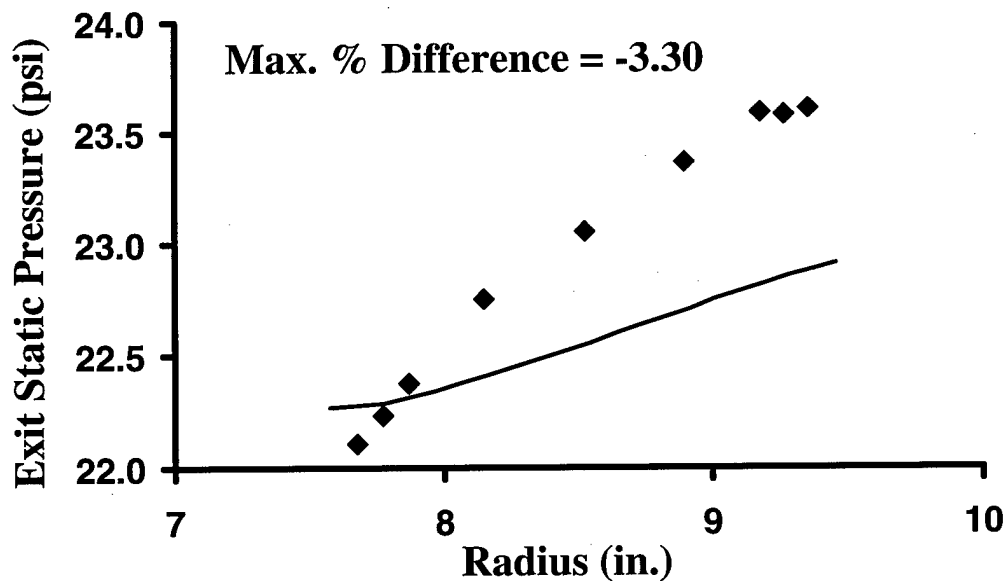◆ Experimental Data   — Uncalibrated SLCC Results

Figure 5.20. Radial Distribution of Exit Static Pressure
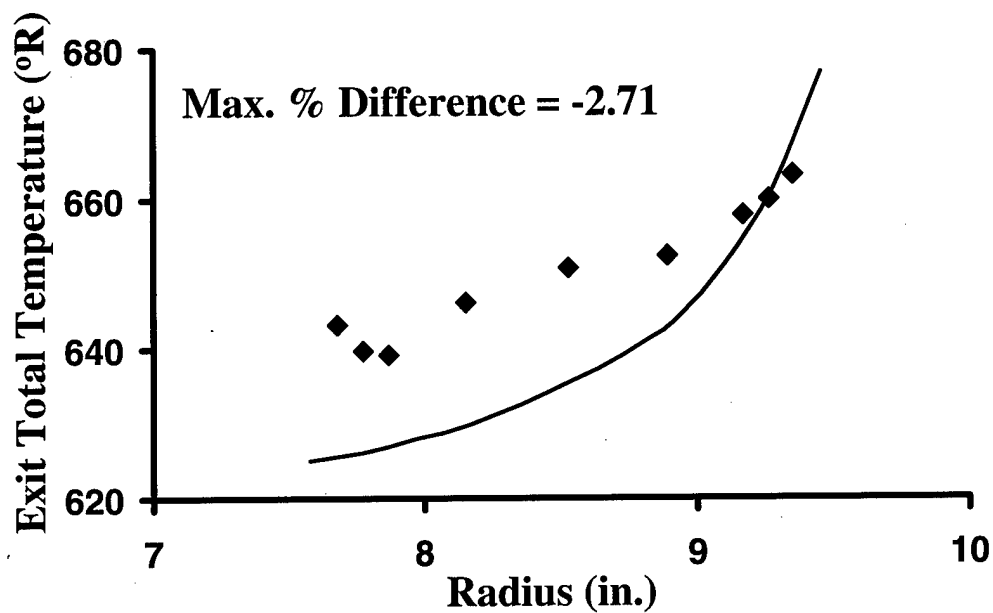for Stage 35 Stator.

Figure 5.21. Radial Distribution of Exit Total Temperature
for Stage 35 Stator.

♦ Experimental Data   — Uncalibrated SLCC Results
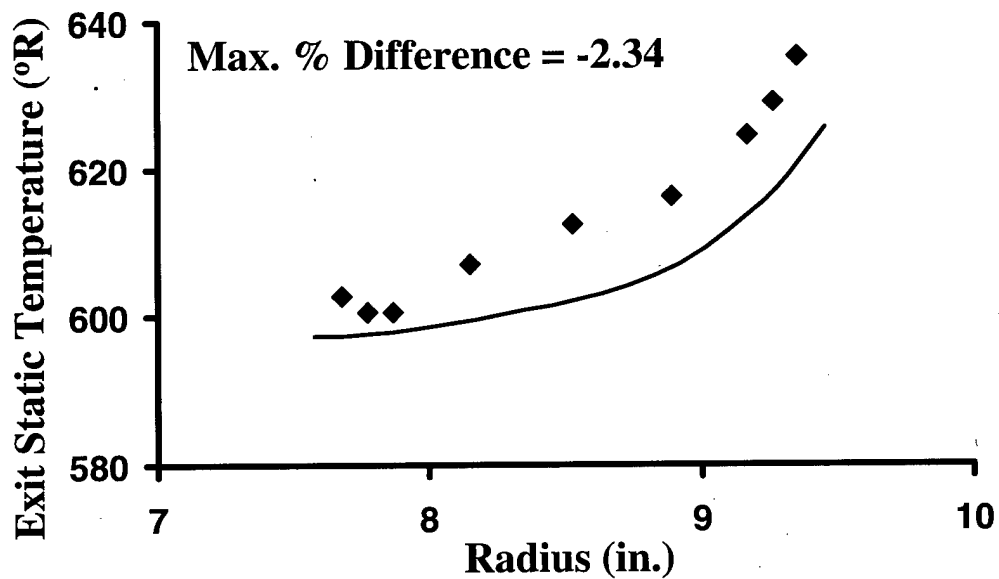
Figure 5.22. Radial Distribution of Exit Static Temperature
for Stage 35 Stator.
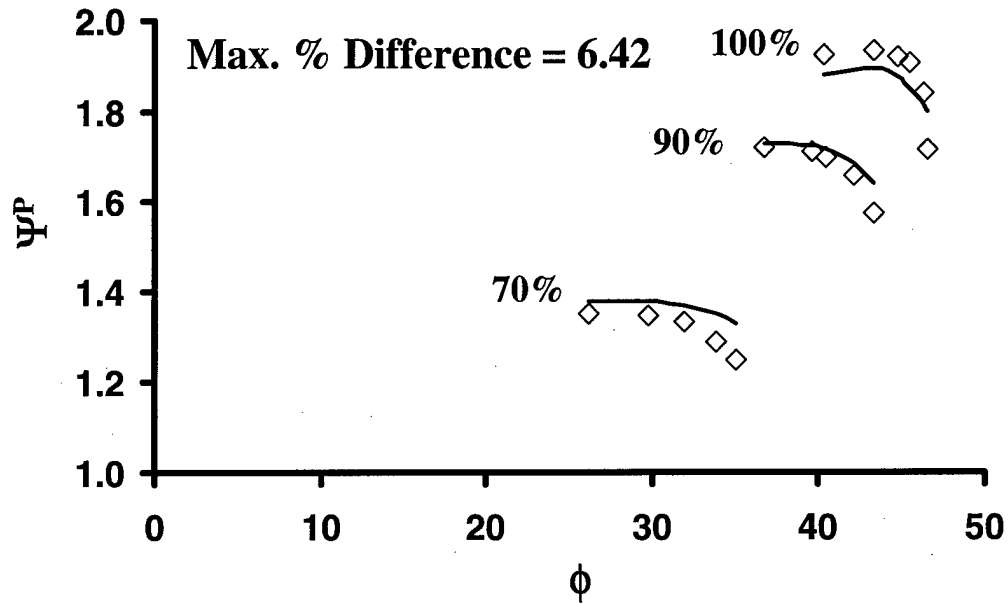
Figure 5.23. 1-D Pressure Characteristic Map for Stage 35.

◇ Data   — Uncalibrated Results

Figure 5.24. 1-D Temperature Characteristic Map for Stage 35.

Figure 5.25. Predicted and Experimental 2-D Pressure Characteristic Map for Stage 35

Figure 5.26. Predicted and Experimental 2-D Temperature Characteristic Map for Stage 35

Appendix C

Summary of the Derivation of the

SLCC Governing Equations

Appendix C – Summary of the Derivation of the

SLCC Governing Equations
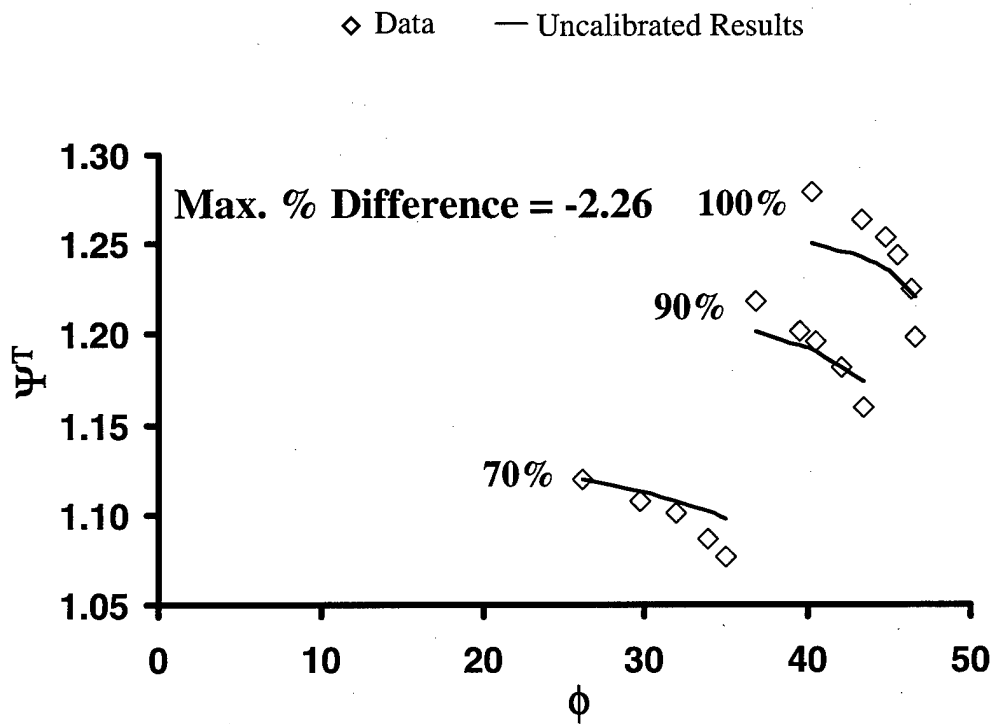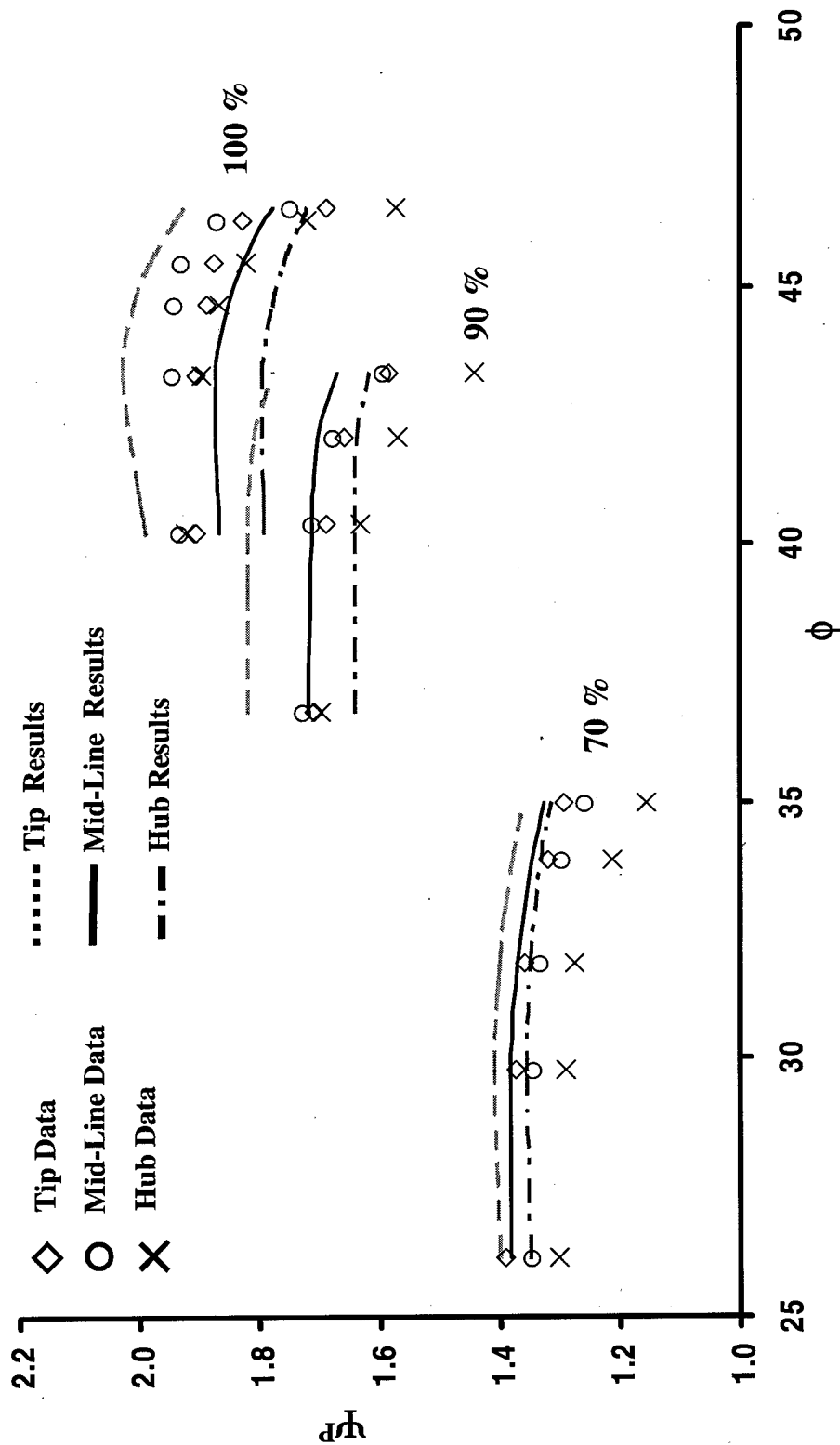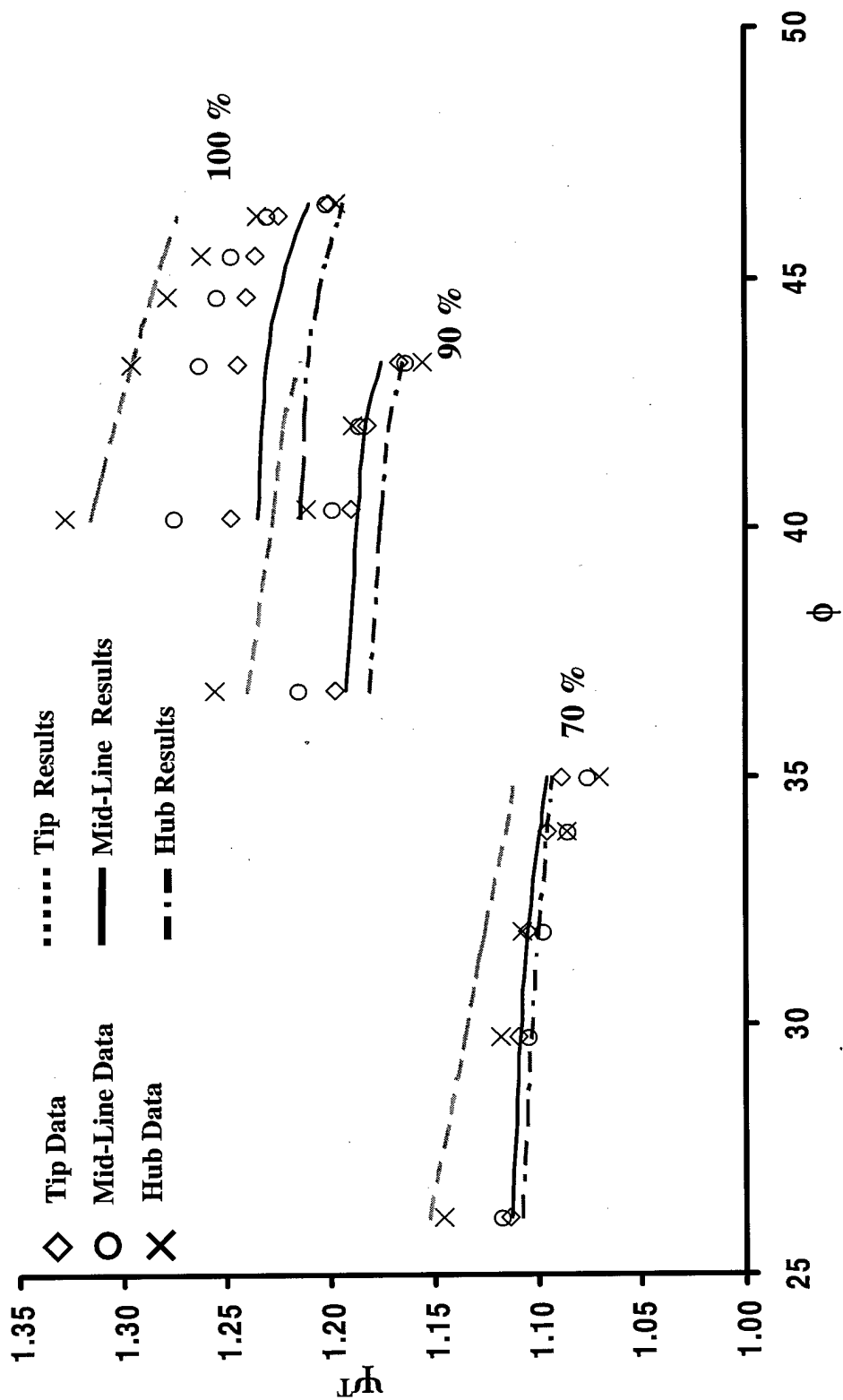
Because the SLCC is an integral part of the method presented in this thesis, it is important to understand the equations governing the code. This appendix will describe the governing equations and how the SLCC calculates streamlines through duct flow and through bladed regions.

C.1 Governing Equations

The governing equations are derived from the Navier-Stokes equations. With the assumptions of:

- Inviscid

- Axisymmetric

- No body forces

- Adiabatic

- Steady-state

the equations reduce to

$$\frac{1}{r}\frac{\partial}{\partial r}(\rho r V_r) + \frac{\partial}{\partial z}(\rho V_z) = 0 \qquad \text{Continuity} \qquad \text{[C.1]}$$

$$V_r\frac{\partial V_\theta}{\partial r} + V_z\frac{\partial V_\theta}{\partial z} + \frac{V_r V_\theta}{r} = 0 \qquad \text{Circumferential Momentum} \qquad \text{[C.2]}$$

$$V_r\frac{\partial V_z}{\partial r} + V_z\frac{\partial V_z}{\partial z} = -\frac{1}{\rho}\frac{\partial P}{\partial z} \qquad \text{Axial Momentum} \qquad \text{[C.3]}$$

$$V_r \frac{\partial V_r}{\partial r} + V_z \frac{\partial V_r}{\partial z} + \frac{V_\theta^2}{r} = -\frac{1}{\rho}\frac{\partial P}{\partial r}$$ Radial Momentum   [C.4]

$$\rho\frac{Dh_t}{Dt} = 0$$ Energy   [C.5]

$$\frac{Ds}{Dt} = 0$$ Entropy   [C.6]

$$P = \rho R T$$ Ideal Gas Equation of State   [C.7]

For use in the SLCC, the conservation equations were mapped to the non-orthogonal m and l coordinate system shown in Figure 3.2. The m direction is the meridional, or streamline, direction. The l direction is the computing station direction that can be leaned to better approximate leading and trailing edges of blades. Mapping Equation [C.2] to these coordinates gives

$$\frac{\partial}{\partial m}(rV_\theta) = 0.$$ [C.8]

This states that the angular momentum is constant along a streamline.

Equation [C.3] maps to

$$V_m\left(1 + \tan^2\beta\right)\frac{dV_m}{dm} = \sin(\phi + \gamma)V_m\frac{dV_m}{dm} - T\frac{dS}{dl} + \frac{dH}{dl} + \frac{V_m^2\cos(\phi + \gamma)}{r_c} -$$

$$\frac{V_m^2}{r}\tan^2\beta\cos\gamma - V_m^2\tan^2\beta\frac{d(\tan\beta)}{dl} + \frac{\cos\gamma}{\sin\phi}\left(T\frac{dS}{dm} - \frac{dH}{dm}\right)\quad [C.9]$$

Equation [C.4] maps to

$$V_m\left(1 + \tan^2\beta\right)\frac{dV_m}{dm} = \sin(\phi + \gamma)V_m\frac{dV_m}{dm} - T\frac{dS}{dl} + \frac{dH}{dl} + \frac{V_m^2\cos(\phi + \gamma)}{r_c} -$$

113

$$\frac{V_m^2}{r}\tan^2\beta\cos\gamma - V_m^2\tan^2\beta\frac{d(\tan\beta)}{dl} + \frac{\sin\gamma}{\cos\phi}\left(\frac{dH}{dm} - T\frac{dS}{dm}\right) \quad [C.10]$$

Upon close inspection of Equations [C.9] and [C.10], they are identified as identical except for the last terms with enthalpy and entropy. By mapping Equations [C.5] and [C.6] to the meridional direction, entropy and enthalpy are shown to remain constant along a streamline. Therefore, the last terms of Equations [C.9] and [C.10] are identically zero. Therefore, Equations [C.9] and [C.10] are equivalent to each other. Therefore, one of the equations can be discarded. It is decided to discard the axial momentum equation. The unknowns in Equation [C.10] are V_m, β, ϕ, T, S, H, r_c, and $\dfrac{dV_m}{dm}$. The next few steps will be presented to reduce the number of unknowns to the ones that can be solved.

By using the rules of differentiation and annulus geometry, it is discovered that

$$\frac{dV_m}{dm} = (1 - \tan\phi\tan\gamma)\frac{\partial V_z}{\partial z} + \frac{V_m\tan\phi}{r_c} - \frac{V_m\sin^2\phi\cos\phi}{\cos\gamma}\frac{d(\tan\phi)}{dl} + \frac{\sin\phi}{\cos\gamma}\frac{dV_m}{dl}. \quad [C.11]$$

However, we have introduced another unknown, the axial gradient of axial velocity. From continuity this can be shown to be

$$\frac{\partial V_z}{\partial z} = \frac{\sin\phi\sin\gamma}{\cos(\phi+\gamma)}\frac{dV_m}{dm} + \frac{\sin\gamma\cos\phi}{\cos(\phi+\gamma)}\frac{V_m}{r_c} - \frac{V_m}{\rho}\frac{d\rho}{dm} - \frac{V_m\sin\phi}{r} - \frac{\cos\phi\sin\phi}{\cos(\phi+\gamma)}\frac{dV_m}{dl} -$$

$$\frac{V_m\cos^4\phi}{\cos(\phi+\gamma)}\frac{d(\tan\phi)}{dl} - \frac{V_m}{\lambda}\frac{d\lambda}{dm}. \quad [C.12]$$

114

This however introduces another unknown, $\dfrac{d\rho}{dm}$, which by assuming perfect gas and knowing that entropy and enthalpy are constant along a streamline can be shown as

$$\frac{1}{\rho}\frac{d\rho}{dm} = -M_m^2\left(\frac{1}{V_m}\frac{dV_m}{dm} - \frac{\tan^2\beta\sin\phi}{r}\right).$$

[C.13]

Then, by combing Equations [C.10], [C.11], [C.12], and [C.13], the radial momentum becomes

$$\frac{dV_m^2}{dl} + A(l)V_m^2 = B(l),$$

[C.14]

where

$$A(l) = -2\cos^2\beta\left[\frac{1-\cos^2(\phi+\gamma)M_m^2}{\cos(\phi+\gamma)(1-M_m^2)} - \frac{\tan\beta}{rT}\frac{d}{dl}(r\tan\beta) - \right.$$

$$\frac{1}{1-M_m^2}\left[\cos^2\phi\tan(\phi+\gamma)\frac{d\tan\phi}{dl} + \frac{\sin(\phi+\gamma)}{\gamma}\frac{d\lambda}{dm}\right] -$$

$$\left.\frac{\sin\phi\sin(\phi+\gamma)(1+M_\theta^2)}{r(1-M_m^2)}\right],$$

[C.15]

and

$$B(l) = 2\cos^2\beta\left[c_p\left(1-\frac{T}{T_t}\right)\frac{dT_t}{dl} - \frac{1}{\rho}\frac{P}{P_t}\frac{dP_t}{dl}\right].$$

[C.16]

The continuity equation is

115

$$W = \int\limits_{hub}^{case} dW = \int\limits_{hub}^{case} \rho V_m \cos(\phi + \gamma)\lambda dA.$$ [C.17]

With these equations defined, the duct flow and bladed region solutions will be described in Sections C.2 and C.3, respectively.

C.2 Duct Flow

The duct flow case involves no bladed region. The eight unknowns for this case are: V_{m2}, ϕ_2, $V_{\theta2}$, P_{t2}, T_{t2}, P_2, T_2, ρ_2. The eight equations that solve these unknowns are:

$$\frac{dV_m^2}{dl} + A(l)V_m^2 = B(l)$$ Radial Momentum   [C.14]

$$\frac{\partial}{\partial m}(rV_\theta) = 0$$ Circumferential Momentum   [C.8]

$$W = \int\limits_{hub}^{case} dW = \int\limits_{hub}^{case} \rho V_m \cos(\phi + \gamma)\lambda dA$$ Continuity   [C.17]

$$\rho \frac{Dh_t}{Dt} = 0$$ Energy   [C.5]

$$\frac{Ds}{Dt} = 0$$ Entropy   [C.6]

$$P = \rho RT$$ Ideal Gas Equation of State   [C.7]

$$T = T_t - \frac{V_m^2 + V_\theta^2}{2c_p}$$ Static Temperature   [C.18]

$$P = P_t\left(\frac{T}{T_t}\right)^{\frac{\gamma}{\gamma-1}}$$ Isentropic Relationship   [C.19]

where the radial momentum, circumferential momentum, continuity, energy, entropy, and ideal gas equation of state were defined in Section C.1. The three closure parameters needed to resolve the flow field are exit swirl velocity, exit total temperature, and exit total pressure. By inspection of Equations [C.5], [C.6], and [C.8], it is known that enthalpy, entropy, and angular momentum are conserved along a streamline. Therefore, the exit swirl velocity can be resolved by integrating the circumferential momentum equation (Equation [C.8]) to give

$$V_{\theta 2} = \left(\frac{r_1}{r_2} \right) V_{\theta 1}.$$
[C.20]

Then, the exit total temperature is found by integrating the energy equation (Equation [C.5]) to give

$$T_{t2} = T_{t1}.$$
[C.21]

Finally, by integrating the entropy equation (Equation [C.6]), the exit total pressure relation becomes

$$P_{t2} = P_{t1}.$$
[C.22]

With these closure relations and the conservation equations listed at the beginning of this section, the entire flow field for a non-bladed region can be resolved.

C.3 Bladed Region

Resolving the flow field in the bladed region is more complicated. The unknowns and several of the governing equations are the same as the duct flow case. The closure relations are the only equations that change. Therefore, the

117

radial momentum (Equation [C.14]), continuity equation (Equation [C.17]), ideal gas equation of state (Equation [C.7]), static temperature equation (Equation [C.18]), and the isentropic relationship (Equation [C.19]) are all the same for the duct flow and bladed region cases. The new closure relations are developed because entropy, enthalpy, and angular momentum are no longer constant along a streamline and must be specified. Because of the complex flow involved when crossing a bladed region, the SLCC does not directly model the bladed regions. For the closure relations to be specified, loss and deviation across a bladed region must be known. For the SLCC used in this investigation, the loss and deviation were specified using loss and deviation correlations. Loss and deviation are defined in Section 3.1.

With deviation specified by the correlations and the velocity triangles and exit streamline angles known at the exit radius, the first of the closure relations, exit swirl velocity, can be calculated from

$$\tan \beta_2 = \frac{W_{\theta 2}}{V_{m2}}$$
[C.23]

$$\cos \phi_2 = \frac{V_{z2}}{V_{m2}}$$
[C.24]

$$V_{\theta 2} = V_{m2} \tan \beta_2 \cos \phi_2 + U_2.$$
[C.25]

The second closure relation uses two relationships for work to calculate the exit total temperature. By equating the Euler turbomachinery equation,

$$w = U_2 V_{\theta 2} - U_1 V_{\theta 1},$$
[C.26]

118

to the first law of thermodynamics with the assumptions of steady-state and isentropic flow with no heat addition,

$$w = h_{t2} - h_{t1},$$ [C.27]

the equation for exit total temperature is determined to be

$$T_{t2} = T_{t1} + U_2 \left[V_{\theta 2} - \frac{r_1}{r_2} V_{\theta 1} \right] \frac{1}{c_p}.$$ [C.28]

The final closure relation is used to calculate the exit total pressure. This relationship uses the thermodynamic quantity rothalpy, defined as

$$I = h + \frac{W^2}{2} - \frac{U^2}{2}.$$ [C.29]

For rothalpy to be conserved in a moving passage, the flow must be steady in the rotating frame, no work can be performed in the rotating frame, and no heat transfer can occur to or from the flow. Then, using the isentropic relations, the relative total pressure loss coefficient, and the conservation of rothalpy, the exit total pressure is determined to be

$$P_{t2} = P_{t1} \left(\frac{T_{t2}}{T_{t1}} \right)^{\frac{\gamma}{\gamma-1}} \left[1 - \left(\frac{P'_{t1}}{P'_{t2}} \right)_{id} \overline{\varpi}' \left(1 - \left[\frac{1}{1 + \frac{\gamma-1}{2} (M'_1)^2} \right]^{\frac{\gamma}{\gamma-1}} \right) \right]$$ [C.30]

where

$$\left(\frac{P'_{t1}}{P'_{t2}} \right)_{id} = \left\{ 1 + \frac{\gamma-1}{2} M_{T1} \left[\left(\frac{r_2}{r_1} \right)^2 - 1 \right] \right\}^{-\frac{\gamma}{\gamma-1}}$$ [C.31]

119

and

$$M_{T1} = \frac{U_1}{\sqrt{\gamma R T'_{t1}}}.$$

[C.32]

With the three closure equations defined, Equations [C.25], [C.28], and [C.30], the conservation equation listed at the top of this section can be solved to develop the flow field for a bladed region.

Appendix D

Compressor Performance Characteristic Forms

Appendix D – Compressor Performance Characteristic Forms

Compressor performance characteristics can be presented in different forms depending on user requirements and application. The following will provide a discussion of four different forms available in the current investigation. These fomrs are all discussed in more detail by Garrard (1995).

The first form is considered the classical form. The stage flow coefficient is defined as

$$\phi = \frac{u}{U} \qquad\qquad [D.1]$$

and the pressure and temperature coefficients, respectively, are defined as

$$\Psi^P = PR \qquad\qquad [D.2]$$

$$\Psi^T = TR - 1. \qquad\qquad [D.3]$$

The second form is defined by using the concepts of Mach number, flow function and critical reference state and are given by

$$\phi = \frac{W_{cor}(NR_{cor})}{W_{corr}^{**}} \qquad\qquad [D.4]$$

$$\Psi^P = PR^{\frac{\gamma-1}{\gamma}}(NR_{cor})^2 \qquad\qquad [D.5]$$

$$\Psi^T = (TR - 1)(NR_{corr})^2. \qquad\qquad [D.6]$$

where

$$W_{cor} = \frac{W\sqrt{T_T}}{P_T A} \qquad\qquad\qquad [D.7]$$

$$NR_{cor} = \frac{Design\ Corrected\ Speed}{Actual\ Corrected\ Speed}, \qquad\qquad [D.8]$$

and

$$W_{cor}^{**} = 0.5318 = Mass\ flow\ function\ representing\ sonic\ conditions. \qquad [D.9]$$

The third form is a derivative of the second form and is given by

$$\phi = W_{cor}' NR_{cor} \qquad\qquad\qquad [D.10]$$

$$\Psi^P = (PR-1)(NR_{cor})^2 \qquad\qquad\qquad [D.11]$$

$$\Psi^T = (TR-1)(NR_{cor})^2, \qquad\qquad\qquad [D.12]$$

where

$$W_{cor}' = \frac{W\sqrt{\dfrac{T_T}{T_{Tref}}}}{\left(\dfrac{P_T}{P_{Tref}}\right)}. \qquad\qquad [D.13]$$

The final form is a variation of the third form but with the removal of the direct influence of speed. The flow, pressure, and temperature coefficients then become

$$\phi = W_{cor}' \qquad\qquad\qquad [D.14]$$

$$\Psi^P = (PR-1) \qquad\qquad\qquad [D.15]$$

$$\Psi^T = (TR-1). \qquad\qquad\qquad [D.16]$$

VITA

Jason Brent Klepper was born in Rogersville, Tennessee, in November 1973 to Mr. Eugene Klepper and Mrs. Joyce Klepper. He grew up in the small community of Persia in upper east Tennessee with his parents and older brother William Klepper. He attended Hawkins County Elementary School and Rogersville Middle School in Rogersville, Tennessee, and graduated from Cherokee Comprehensive High School in May 1992. Jason entered Tennessee Technological University in the fall of 1992, and in May 1997, he received a Bachelors of Science degree in Mechanical Engineering. He then enrolled in the graduate program at the University of Tennessee Space Institute in Tullahoma, Tennessee, in the summer of 1997 as a Graduate Research Assistant for Sverdrup Technology, Inc. at the Arnold Engineering Development Center. In August of 1998, Jason officially received a Master of Science degree in Mechanical Engineering.